ulm university universität
uulm

Impulse-Radio Ultra-Wideband Systems for Vital-Sign Monitoring and Short-Range Communications

DISSERTATION

zur Erlangung des akademischen Grades eines

DOKTOR-INGENIEURS

(Dr.-Ing.)

der Fakultät für Ingenieurwissenschaften
und Informatik der Universität Ulm

von

Bernd Schleicher

aus Villingen-Schwenningen

Gutachter: Prof. Dr.-Ing. Hermann Schumacher

Prof. Dr.-Ing. Dr.-Ing. habil. Robert Weigel

Amtierender Dekan: Prof. Dr.-Ing. Klaus Dietmayer

Ulm, 08. November 2011

Printed version published by Verlag Dr. Hut, München
Sternstr. 18, 80538 München
www.dr.hut-verlag.de

ISBN 978-3-8439-0302-8

1. Auflage 2012

to my family

Preface

This thesis is the result of my time in the Institute of Electron Devices and Circuits at Ulm University. It is the second study on ultra-wideband technology at the institute and is consequently carrying on the work which was done by my predecessor Dr.-Ing. Jochen Dederer in [1]. Part of this work was done within the project "UWB in Medicine", which was financially supported under the priority program "Ultrabreitband-Funktechniken für Kommunikation, Lokalisierung und Sensorik (UKoLoS)" of the German Research Foundation (Deutsche Forschungsgemeinschaft, DFG). In this program our institute collaborated with the Institute of Microwave Techniques and the Institute of Information Technology, both from Ulm University.

I would like to thank a lot of people for their contribution, help, critique and support, making this dissertation possible. First of all, I would like to express my deepest gratitude to Prof. Dr.-Ing. Hermann Schumacher for giving me the opportunity to work in his group and an excellently equipped research environment as well as for supporting and encouraging me in all aspects during my time in Ulm. I am strongly indebted to the Institute's "UWB-fellow" Dr.-Ing. Jochen Dederer for intensive and very helpful discussions and especially for his pioneering integrated circuits, without which this thesis would not have become possible. I am deeply grateful to Dr.-Ing. Mario Leib for sharing his expertise on antennas and passive circuits, for his great help and fruitful discussions exceeding the aspects of the UKoLoS project and for granting access to the Vivaldi antennas and the power divider used in this work. I also owe a deep gratitude to Dr.-Ing. Andreas Trasser for his helpful advice and critique as well as for his proficiency in bonding. Many thanks to Prof. Dr.-Ing. Dr.-Ing. habil. Robert Weigel for his time and effort of being the second reviewer for this thesis. I am indebted to Dayang Lin for fantastic discussions and great support. Furthermore I am indebted to Ismail Nasr, Shamsuddin Ahmed, Çağrı A. Ulusoy, Rania Morsi, Miroslav Másar, Filipe Tabarani, Hatem Ghaleb and Rana Desouki for their big help and contribution throughout their final theses or as research assistants.

I would like to express my deep appreciation to Thanawat Thiasiriphet, Michael Mirbach, Prof. Dr.-Ing. Wolfgang Menzel and Prof. Dr.-Ing. Jürgen Lindner for their great effort and companionship in all aspects of the collaboration through the

UKoLoS project. Many thanks as well to the DFG for financial support. I would like to thank Ronald Ehrlich for his assistance in electronic circuit mounting, Ursula Winter for her help on clearing all administrative hurdles, Ferdinand Sigloch for his help in computer issues, Dr. Wolfgang Schwerzel from Telefunken Semiconductors, Heilbronn for the excellent cooperation and all the staff members of the Institute of Electron Devices and Circuits for the nice working atmosphere; special thanks to Xiaolei Gai and Ursula Spitzberg, with which I shared the office. I would like to express my deep appreciation to Dr.-Ing. Sébastien Chartier and Wolfgang Rubin for proof-reading and Helga Aichele and Rob Christ for corrections.

Last but not least I am infinitely grateful to my wife Veronika and my family for their loving guidance and continuous support throughout my life.

Ulm and München, June 2011

Bernd Schleicher

Contents

Preface v

1 Motivation 1

2 Introduction to Impulse-Radio Ultra-Wideband 5
2.1 FCC and ECC Regulation Situation 5
2.2 Impulse Shapes for IR-UWB Systems 7
2.2.1 Derivatives of the Gaussian Bell Shape 7
2.2.2 Gaussian-Gated Sinusoidal Functions 9
2.2.3 Repetition of Impulses in Time and Spectral Domain 10
2.2.4 Impulse Shape in Bandwidth-Limiting, Dispersive and Reflection-Tainted Environments 13
2.3 Basic IR-UWB Transceiver Concepts 16
2.3.1 Energy-Detection Receiver 16
2.3.2 Correlation-Detection Receiver 17
2.3.3 Impulse Modulation Methods 19

3 IR-UWB Radar Sensor for Location Tracking and Movement Detection 21
3.1 Introduction to Breath-Rate Sensing 22
3.2 IR-UWB Components for the Radar Demonstrator 23
3.2.1 Impulse Generator Fitting the FCC Indoor Mask 23
3.2.2 FCC-Compliant Correlation Receiver 27
3.2.3 UWB Directional Antennas 30
3.3 Transmission Evaluation 32
3.4 Radar Using Undersampling Reception 33
3.5 Radar Using a Hardware Correlator 37
3.5.1 Hard- and Software Implementation 37
3.5.2 Correlation-Slope Detection 40
3.5.3 Sweeping-Impulse Correlation 43

4 Analog Transmission Using Frequency Modulation of Impulses 51
4.1 Introduction to the Principle 51

4.2 Components for the FM IR-UWB Demonstrator 54
4.2.1 UWB Low-Noise Amplifier 54
4.2.2 Schottky Diode Rectifier 58
4.2.3 Low-Pass Filter 61
4.2.4 UWB Omnidirectional Monopole Antennas 62
4.2.5 FM Modulator and Demodulator 63
4.3 Measurements on the Demonstrator 64
4.3.1 FM IR-UWB Transmitter and Receiver Evaluation 64
4.3.2 Wireless Transmission 66
4.4 Measurements on Interference Robustness 67
4.4.1 Multipath Propagation 68
4.4.2 Multi-User Environment 72
4.4.3 Narrowband Interference 74

5 Advanced Concepts 79
5.1 Electronically Beam-Steerable UWB Antenna Array 79
5.1.1 Introduction to the Principle 80
5.1.2 Measurements on a 4x1 Antenna Array 86
5.2 Impulse Generator Targeting the ECC Mask 91
5.2.1 Circuit Concept and Simulations 91
5.2.2 Measurement Results 93
5.2.3 Modeling the Impulse Shape 94
5.3 Biphase Impulse Modulator Circuit 96
5.3.1 Circuit Concept 96
5.3.2 Measurement Results 98

6 Conclusion 101

A UWB Spectral Allocations 103
A.1 United States FCC Regulation 103
A.2 European ECC Regulation 104

B Abbreviations and Symbols 105

C Publications 109

Bibliography 113

1 Motivation

In their report on "Assessment of Ultra-Wideband (UWB) Technology" published in 1990, the expert group composed by the U.S. Defense Advanced Research Projects Agency (DARPA) and the Office of the Secretary of Defense (OSD) pointed out that UWB technology has no unique features compared to other radio transmission or sensing systems [2]. For some features claimed to be unique, they even *"found that this claim was due to inadequate understanding of the issues or erroneous application of electromagnetic theory and is incorrect"*.

However, apart from *unique features*, interesting for state authorities like the military, which do not have to care about regulation issues and power consumption, impulse-radio ultra-wideband (IR-UWB) technology offers *attractive features* for new commercial radio communication and sensing systems. One attractive feature of IR-UWB compared to continuous-wave (CW) systems is the radiation of short time domain transients, which allow the use of new and very simple system concepts for precise radar devices, of which some are detailed in the following sections. Another attractive feature of IR-UWB is the large power saving potential, because large parts of the electronics in transmitter and receiver are not used between the impulses and can therefore operate in idle state. This leads to a small duty cycle and therefore can save large amounts of power. A further general benefit of UWB is the spreading of the transmitted signal across a large spectrum. Thus a low transmit power density can be obtained, allowing a coexistence of UWB technology together with narrowband systems. Additionally, electromagnetic interference of the IR-UWB system to nearby located electronic devices is mediated much more than in conventional narrowband radio systems. Due to this, the use of UWB technology is well suited to electromagnetically sensitive environments, e.g. on board an aircraft or in a clinical environment.

In this thesis, the suitability of IR-UWB technology shall be investigated in a radar sensor for the measurement of human breathing and in a wireless IR-UWB transceiver of general acquired analog sensor signals, transmitted to a closely-located base station. The radar sensor could be used in a variety of applications. One application could be to measure the breath-rate of adults, children or infants in a clinical intensive-care unit. In contrast to methods using wired electrodes, e.g. in thoracic

impedance measurements, this sensor would have the advantage of measuring the breathing rate contact-free, which could increase acceptance by the patients or their parents. The sensor could be pre-installed in the intensive-care unit, abandoning the need for attaching electrodes and thus improving hygiene, because the patient need not be touched. A picture of a typical newborn intensive-care unit in a hospital can be seen in Fig. 1.1.

Figure 1.1: Typical newborn intensive-care unit, where the contact-free UWB radar sensor could be installed in the cover of the unit.

Another application for a UWB radar sensor deals with the detection of the occupation of seats in the back of a car. Every year an average number of 37 children[1] die in the U.S. from hyperthermia as a result of being left unattended in a car [3]. Astonishingly, it was found out that about half of the affected children were left in the car unintentionally while sleeping. In addition, it is estimated that each year hundreds of children experience heat illness by the same cause. In [3] was demonstrated experimentally that already at a relatively moderate ambient temperature of 22° C on a sunny day, the temperature in a car can rise up to 47° C within 60 minutes. This can

[1] Average of the period from 1998 to 2010.

cause a hyperthermia incident. By sensing for a breathing pattern, the occupancy of car seats in the back could be detected and an alarm could be triggered when the car is left unattended by the driver while a child is still in it. Other detection techniques for this scenario have certain disadvantages: A pressure sensor in the seat, for example, cannot distinguish between a child and a heavy bag; an accelerometer will not respond when the child is sleeping; and a thermal sensor will not detect a human being when the ambient temperature is around 37° C.

Another example for the use of a breath-rate sensor deals with aircraft passengers being stressed due to flight disorders, which is a common problem on board an aircraft [4, 5]. Airlines train their flight attendants to recognize visible symptoms of stressed people, to pay particular attention to these individuals and to start relaxing or cheering-up countermeasures if necessary. In such a situation, a contact-free breathing sensor, placed in front of each seat in the plane, could assist the flight attendants in recognizing stress symptoms by reporting stress-increased breathing. This could improve the comfort of travelers and decrease the need for medical assistance during a flight.

Besides applying UWB technology for breathing-pattern measurements, an extremely simple IR-UWB method is envisioned to transmit acquired analog information to a network node in close vicinity. In the clinical context the analog information could originate for example from sensors measuring the patient's body temperature or blood oxygen concentration; in an airplane the system could be used to wirelessly distribute the on-board audio channels to the passenger's headphones. The benefit of transmitting analog information with an analog (not a digital) transmission scheme is the reduced complexity of the wireless unit because the analog-to-digital converter (ADC) can be saved. Especially in the above scenarios, the use of UWB technology is favored to allow an interference-reduced operation to other equipment in the aforementioned electromagnetically sensitive environments. Both information-transmission scenarios promise an increased patient or passenger comfort because no cable wiring is necessary. Since it should be possible to place many sensors close to each other, the transmission must be multi-user capable and should not be distorted by other radio-transmission systems.

2 Introduction to Impulse-Radio Ultra-Wideband

The world's first commercial regulation on ultra-wideband (UWB) technology [6] by the U.S. Federal Communications Commission (FCC) in 2002, marks the biggest milestone in the recent UWB history to date. Evidence of UWB research and development can be found throughout many decades in radio history; some even consider the spark-gap transmitter Heinrich Hertz used for his first transmission experiments in 1887 as a UWB transmission [7]. However, the antennas he used did most probably not conform to the modern definitions of UWB technology. A major study on UWB technology in the areas of radar, communications, electronic warfare and radio-frequency (RF) weaponization was driven by U.S. military interests and published in 1990 [2]. A detailed overview of pioneering UWB works can be found in [7–9]. The FCC regulation initiated the commercialized use of UWB technology and thus magnified interest in this technological field in both academics and industry. Based on the FCC decision, nearly all countries worldwide started to open up their frequency bands to the use of UWB technology.

2.1 FCC and ECC Regulation Situation

According to the FCC definition in [6], a signal is an ultra-wideband signal when its fractional bandwidth is larger than 25% or the absolute bandwidth is larger than 500 MHz. The fractional bandwidth B_f can be calculated according to

$$B_f = \frac{B_{tot}}{f_c} = \frac{f_H - f_L}{(f_H + f_L)/2}\,, \tag{2.1}$$

where $B_{tot} = (f_H - f_L)$ is the total bandwidth, f_c is the center frequency and f_H and f_L denote the upper and lower -10 dB corner frequency of the signal. The FCC regulations allow a spectral location of the UWB radiation to overlap with already existing radio services. But, to ensure that there is only negligible interference to these systems, UWB must operate at a very reduced power spectral density (PSD) level. The allowed level is adopted from the U.S. Code of Federal Regulations, Title

47, Part 15 [10] for unintended emissions of electronic devices, which is at a maximum mean effective isotropic radiated power (EIRP) density level of 75 nW/MHz or -41.3 dBm/MHz. To further protect sensitive existing services, e.g. GPS, GSM or radio astronomy bands, the FCC introduced frequency masks for the intended UWB emissions. For indoor and outdoor UWB operation, the FCC allocated masks in the range of 3.1–10.6 GHz. Fig. 2.1 (a) shows this FCC allocation compared to some existing services in the band. The detailed mask values are given in Appendix A.1. To calculate the available mean power in the FCC spectral mask from 3.1–10.6 GHz, which is obtained when the band is completely exploited, we can multiply the spectral density of -41.3 dBm/MHz with the 7.5 GHz bandwidth (cf. [11]). This results in a mean power of 562.5 µW. The FCC allows a peak emission limit for UWB devices of 0 dBm EIRP density, measured in a 50 MHz bandwidth.

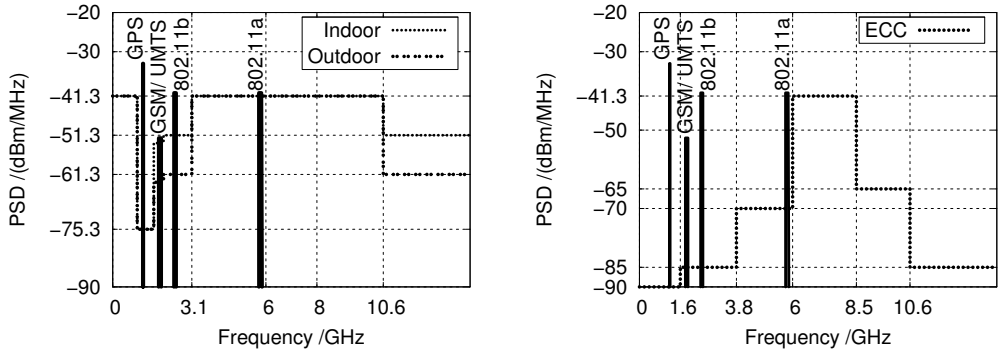

Figure 2.1: Spectral comparison between some existing services and (a) the FCC UWB masks in the USA and (b) the mitigation-free UWB band in Europe.

In 2007 the Electronic Communication Commission (ECC) in Europe also allocated a frequency band for the use with UWB technology [12, 13]. Therein the generic use of ultra-wideband applications is specified at a maximum mean EIRP spectral density of -41.3 dBm/MHz in the band from 6–8.5 GHz. From 3.4–4.8 GHz bands are specified, in which mitigation techniques, like a low duty cycle operation or a detect and avoid operation, must be applied to further protect existing services [14]. In this study we focus on the mitigation-free bands only. Fig. 2.1 (b) illustrates the ECC mask where no mitigation techniques need to be applied in comparison to some existing services, the detailed mask values are presented in Appendix A.2. The available mean power in the ECC band from 6–8.5 GHz can be calculated similarly

as above and results in 187.5 µW. As a maximum value, a peak emission limit of 0 dBm/50 MHz is allowed in the band from 6–8.5 GHz.

In general, all emissions fulfilling the aforementioned spectral and power requirements are allowed to transmit within the UWB bands. This has led to mainly two branches of UWB systems: the originally intended impulse-radio (IR) UWB systems and spread-spectrum UWB systems, like e.g. the OFDM UWB. Because this thesis focuses on IR-UWB only, the following section deals with suitable impulses for the allocated UWB masks.

2.2 Impulse Shapes for IR-UWB Systems

In general, an impulse used in a UWB system must satisfy two main criteria. It must make efficient use of the spectral mask and should have a small time-domain extension at the same time. Fitting to a spectral mask is demanded by the regulation. A larger time-domain extension would worsen the spatial resolution of a radar system. Unfortunately, spectral occupation and time-domain extension are inversely related. This means, on one hand, an impulse completely filling the rectangular shape of a spectral mask has an infinite time duration and, on the other hand, a very short spike in time domain occupies an infinite spectrum. For UWB systems, the requirements of making efficient use of the allocated mask with a good time extension therefore stand in contrast to each other. Nevertheless in specialist literature, e.g. [15–20], some advantageous impulse shapes are discussed, presenting an interesting compromise. However, applying such a waveform results in a reduced spectral occupation in form of an implementation loss of spectral signal energy. Yet it comes with the benefit of a desireably small impulse duration. One of those waveforms is based on the Gaussian bell shape. It can be made compliant to the UWB masks and it has a small spectral implementation loss with good time-domain extension. This waveform is introduced in two ways mathematically in the following sections.

2.2.1 Derivatives of the Gaussian Bell Shape

The general Gaussian bell shape is defined as

$$f(t) = \frac{A_0}{\sqrt{2\pi} \cdot \sigma} \cdot \exp\left(-\frac{t^2}{2\sigma^2}\right) , \tag{2.2}$$

where A_0 is the normalizing amplitude and σ is the standard deviation. The derivatives of the Gaussian bell shape lead to waveforms which are DC-free and can be radiated by an antenna. To fit the impulse shape to a spectral mask, the two possible adjustment parameters are the derivative order and the standard deviation σ, with which the spectral broadening and the center frequency of the impulse can be brought into the UWB masks. A detailed description on the fitting of Gaussian derivative impulses to the UWB masks can be found in [20]. To fulfill the requirements for the FCC indoor mask, a fifth derivative of the Gaussian bell shape with a $\sigma = 51$ ps needs to be selected. The fifth Gaussian derivative can be calculated according to

$$f(t) = \frac{A_5}{\sqrt{2\pi}} \cdot \left(-\frac{t^5}{\sigma^{11}} + \frac{10 \cdot t^3}{\sigma^9} - \frac{15 \cdot t}{\sigma^7} \right) \cdot \exp\left(-\frac{t^2}{2\sigma^2} \right) . \tag{2.3}$$

The corresponding time-domain waveform can be seen in Fig. 2.2 (a). The time-domain extension of the waveform can be determined by measuring the full-width at half-maximum (FWHM) of the impulse's envelope function, since this represents a precisely measurable entity. The time extension of the fifth Gaussian derivative with a $\sigma = 51$ ps is 180 ps (FWHM). Fig. 2.2 (b) shows the Fourier transformed impulse shape in a normalized spectral domain representation and compared to the FCC-allocated spectral mask for indoor applications. The figure shows that the impulse shape fits well into the mask.

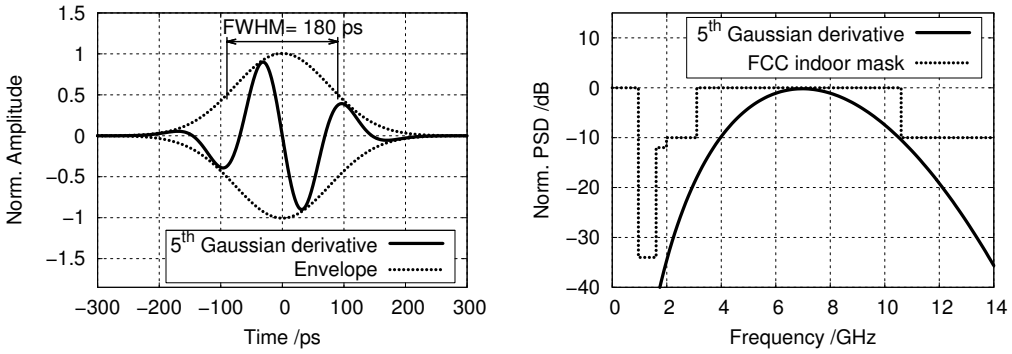

(a) (b)

Figure 2.2: Fifth derivative of a Gaussian bell shape with $\sigma = 51$ ps for efficient use of the FCC indoor mask in (a) time and (b) frequency domain.

The seventh derivative of the Gaussian bell shape with a $\sigma = 65$ ps fits the FCC outdoor mask. The waveform can be seen in Fig. 2.3 (a) in time domain, having a

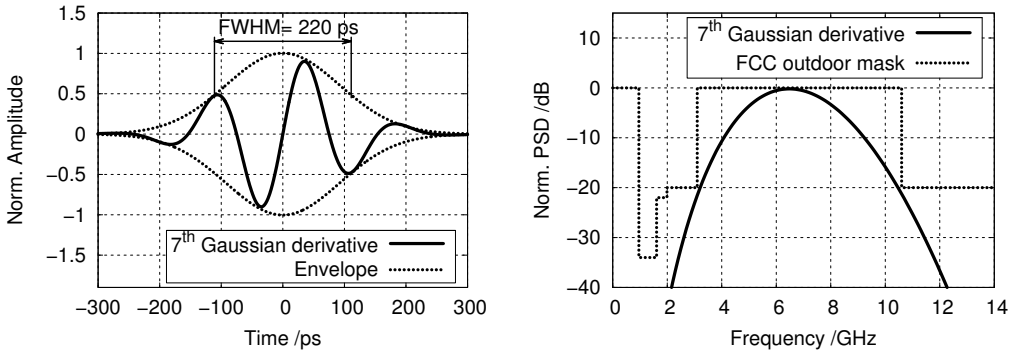

(a) (b)

Figure 2.3: Seventh derivative of a Gaussian bell shape with $\sigma = 65$ ps for efficient use of the FCC outdoor mask in (a) time and (b) frequency domain.

time extension of 220 ps (FWHM). In Fig. 2.3 (b) the normalized spectral domain shape is compared to the FCC outdoor mask and is shown to fit to this allocation. The seventh derivative can be obtained mathematically by

$$f(t) = \frac{A_7}{\sqrt{2\pi}} \cdot \left(-\frac{t^7}{\sigma^{15}} + \frac{21 \cdot t^5}{\sigma^{13}} - \frac{105 \cdot t^3}{\sigma^{11}} + \frac{105 \cdot t}{\sigma^9} \right) \cdot \exp\left(-\frac{t^2}{2\sigma^2} \right) \ . \quad (2.4)$$

Both waveforms, the fifth and the seventh Gaussian derivative, present a compromise of a short impulse duration and an efficient spectral occupation and therefore do not fill the spectrum from 3.1–10.6 GHz completely. Especially the signal content at the corners is missing. To identify the implementation loss of these impulse shapes, the power of the waveform, as the integral of the spectral curve, can be calculated and related to the mean power of the FCC-allocated spectrum. The implementation loss of the fifth derivative of the Gaussian function is 2.9 dB, the implementation loss of the seventh derivative is 3.9 dB.

2.2.2 Gaussian-Gated Sinusoidal Functions

A second way of constructing UWB impulses is to use the Gaussian bell shape as an envelope function of a sinusoidal carrier signal [21]. This can be represented mathematically according to

$$f(t) = \frac{A}{\sqrt{2\pi} \cdot \sigma} \cdot \exp\left(-\frac{t^2}{2\sigma^2} \right) \cdot \sin\left(2\pi f \cdot t \right) \ , \quad (2.5)$$

where σ is the standard deviation of the envelope function determining the impulse width, f the frequency used in the sinusoidal function determining the impulse center frequency and A the normalizing amplitude. With this mathematical representation, impulses fitting the FCC masks can be realized choosing $f = 7\,\text{GHz}$ and $\sigma = 76.5\,\text{ps}$ for the indoor and $f = 7\,\text{GHz}$, and $\sigma = 92\,\text{ps}$ for the outdoor mask, which are similar to fifth and seventh Gaussian derivatives, respectively. Besides describing the FCC impulses, the Gaussian-gated sinusoidal representation is well suited for a description of impulses fulfilling the ECC regulation in Europe. As discussed earlier, the ECC regulation requires a much narrower spectral mask than the FCC regulation and also steeper sidewalls at the spectral boundaries. Therefore a longer impulse time extension is necessary.

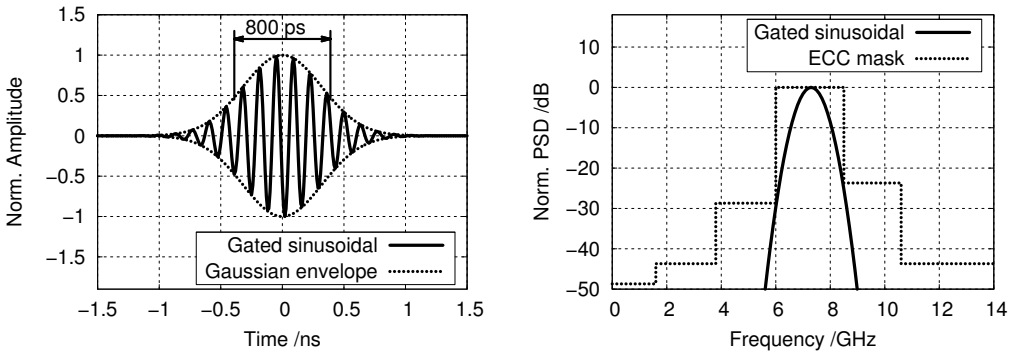

(a) (b)

Figure 2.4: Gaussian-gated sinusoidal impulse fitting the ECC mask in (a) time and (b) spectral domain.

Fig. 2.4 shows the time and spectral domain shape of a gated sinusoidal, which fits the ECC mask. To obtain this impulse shape, $f = 7.3\,\text{GHz}$ and $\sigma = 320\,\text{ps}$ are used in (2.5). The impulse has a time-domain extension of 800 ps (FWHM) and makes efficient use of the ECC mask. The implementation loss of the applied Gaussian-gated sinusoidal impulse compared to a completely exploited ECC mask is 4.5 dB.

2.2.3 Repetition of Impulses in Time and Spectral Domain

The previous spectral-domain impulse representations are focusing on a single impulse only. In case of a modulated or unmodulated impulse train, the spectral domain representations of Figs. 2.2 (b), 2.3 (b) and 2.4 (b) change. An unmodulated

impulse sequence with equally spaced impulses can be described mathematically by a convolution of the time-domain impulse with a Dirac comb or Shah function. The periodic repetition of the impulses is given by the repetition interval T_{rep}. The Fourier transformation of the Dirac comb results in a line spectrum with a frequency spacing of the lines of $f_{rep} = 1/T_{rep}$. The spectrum of a time-domain impulse train consists of a line spectrum which is weighted by a spectral envelope function according to the chosen impulse shape. Fig. 2.5 depicts an example of an impulse train with equally spaced fifth Gaussian derivative impulses at a repetition rate of 200 MHz in time and spectral domain, where the lines with a spacing of 200 MHz can be seen clearly as well as the envelope function compared to the FCC indoor mask. In case of a modulated impulse sequence, spectral emission as well between the spectral lines occurs depending on the applied modulation, cf. Sec. 2.3.3.

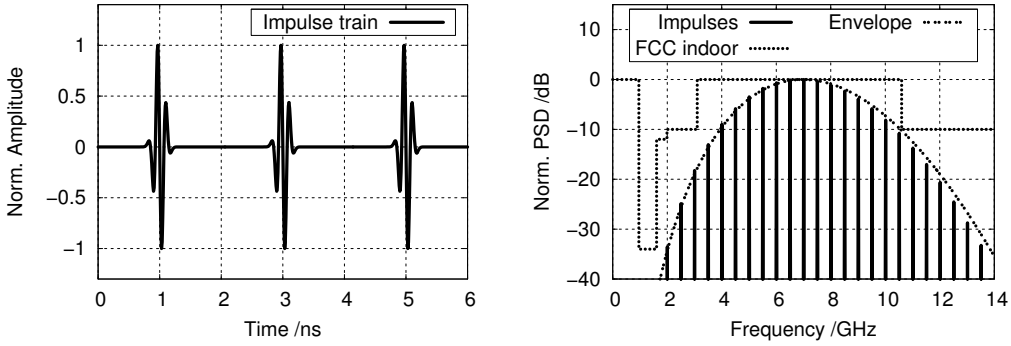

Figure 2.5: Impulse train using fifth derivative impulses with a repetition rate of 200 MHz in (a) time and (b) frequency domain, illustrating the change in spectral appearance.

To fully exploit the mean -41.3 dBm/MHz and the peak 0 dBm/50 MHz EIRP densities of the allocated UWB masks, the impulse repetition rate and the impulse amplitude both are of great importance. This can be explained using time and frequency considerations: An increase in impulse repetition interval T_{rep} in time domain means that the impulse's mean power is distributed over a larger time instance. To obtain the same mean power density, the impulse amplitude can be enlarged. In frequency domain, an increase in repetition interval results in an increased number of spectral lines. Thus, the impulse emission is distributed to more spectral lines, and the impulse amplitude can be increased to approach the upper boundary of the regulation mask.

To evaluate the allowed maximum impulse amplitude at a given repetition rate, the investigation must follow the measurement descriptions of the regulations in [6, 10] for the FCC and in [12, 14] for the ECC mask. Both regulations specify to use a spectrum analyzer with a 1 MHz resolution bandwidth and the root-mean-square (RMS) detector for the mean EIRP and a 50 MHz bandwidth and the maximum detector for the peak EIRP evaluations. The computations presented study the case in which the amplitude of the simulated PSD corresponds directly to the EIRP density limits. This represents a measurement where the impulse generator is directly connected to the 50 Ohm input port of a spectrum analyzer. The influence of the applied antennas has to be considered separately.

A computation of the maximum possible impulse voltage amplitude with compliance to the FCC indoor mask is plotted in Fig. 2.6 (a) using a fifth Gaussian derivative with $\sigma = 51$ ps. For this plot, three repetition-rate regions can be identified. For repetition rates larger than 1 MHz, and with this larger than the resolution bandwidth of the spectrum analyzer, the maximum amplitude allowed follows $A = (13.4\,\mathrm{MHz}/f_{rep}) \cdot \mathrm{V}$. In the region between 1 MHz and 420 kHz, which is the region where the spectral content of more than one spectral line sums up in the resolution-bandwidth filter, the maximum amplitude varies with $A = \sqrt{169\,\mathrm{MHz}/f_{rep}} \cdot V$. For repetition rates below 420 kHz, a constant maximum amplitude of $A = 20.7\,\mathrm{V}$ is permitted, which is limited by the peak-emission requirement.

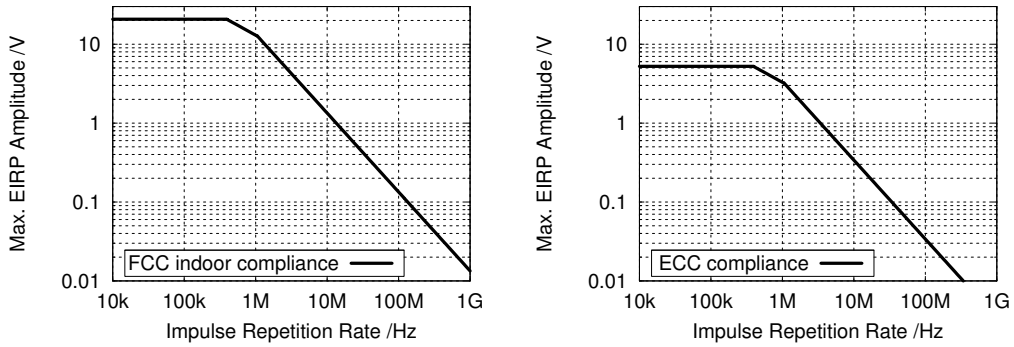

Figure 2.6: Maximum voltage amplitudes allowed with compliance to UWB mask for different repetition rates using (a) a fifth Gaussian derivative for the FCC indoor mask and (b) a Gaussian-gated sinusoidal for the ECC mask.

For the ECC mask, Fig. 2.6 (b) shows the maximum voltage amplitude allowed using a Gaussian-gated sinusoidal with $f = 7.3\,\mathrm{GHz}$ and $\sigma = 320\,\mathrm{ps}$. The same repetition rate regions can be identified for compliance to the ECC mask, but with different peak amplitudes. In the region with repetition rates larger than 1 MHz, the maximum amplitude allowed varies with $A = (3.4\,\mathrm{MHz}/f_{rep}) \cdot \mathrm{V}$. Between 1 MHz and 420 kHz, the amplitude varies with $A = \sqrt{10.8\,\mathrm{MHz}/f_{rep}} \cdot V$, and below a repetition rate of 420 kHz, a constant maximum amplitude of $5.2\,\mathrm{V}$ is acceptable. An evaluation supporting these results is presented in [22].

2.2.4 Impulse Shape in Bandwidth-Limiting, Dispersive and Reflection-Tainted Environments

Processing a broadband impulse with linear but band-limited or dispersive components (e.g. amplifiers, antennas, filters) will change the shape of the impulse, both in the time and the frequency domain. These effects can be seen in measurements in later sections, but will be introduced by theoretical considerations here. As a first example, the influence of a bandwidth-limitation of a component is studied. A bandwidth limitation will naturally result in the longer time-domain extension of an excited UWB impulse. For the numerical evaluation of the bandwidth limitation, an artificial bandpass is set up that only changes the spectral amplitude of the incoming signal. The phase of the incoming signal and therefore its group delay is not affected. The amplitude variation of the bandpass is Gaussian-shaped according to

$$A_{BP}(f) = \exp\left(-\frac{(f - f_c)^2}{2 \cdot \sigma_{BP}^2}\right) , \tag{2.6}$$

where f_c is the center frequency of the bandpass and σ_{BP} is the standard deviation of the Gaussian function, responsible for the bandwidth. For example, a bandpass is computed using $f_c = 6.85\,\mathrm{GHz}$ and $\sigma_{BP} = 2.47\,\mathrm{GHz}$ centered in the UWB band with a -10 dB attenuation at the 3.1–10.6 GHz corner frequencies. This bandpass may represent a concatenation of system components, e.g. two antennas. A fifth Gaussian derivative impulse with a $\sigma = 51\,\mathrm{ps}$ is fed through this bandpass by a numerical simulation. Fig. 2.7 gives a comparison between simulated input and output impulses of this bandpass filtering. In time domain the resulting output impulse is broader than the input impulse and resembles the shape of a seventh Gaussian derivative with a $\sigma = 65\,\mathrm{ps}$. Therefore it fits well into the narrower FCC outdoor mask, which is displayed in Fig. 2.7 (b) in the spectral representation.

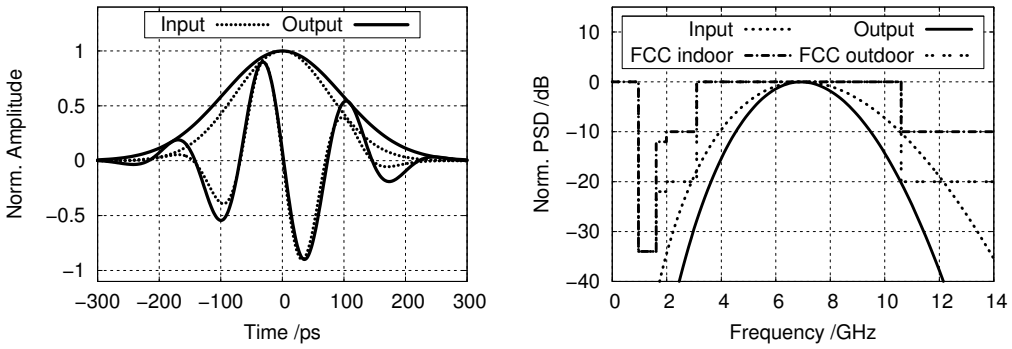

(a) (b)

Figure 2.7: Comparison of input and output shape of a fifth Gaussian derivative impulse feed through a filter with Gaussian-shaped filter response in (a) time and (b) spectral domain.

A different distortion is caused by the variation of group delay in a linear component. The group delay represents the time it takes for a signal to pass through a system. Ideally this time is the same for all frequencies, but in real components some frequencies are processed faster than others, which is of concern especially in a broadband system. A measure of this effect is found in the group delay variation $\Delta\tau_g$ as the value between minimum and maximum group delay in a certain

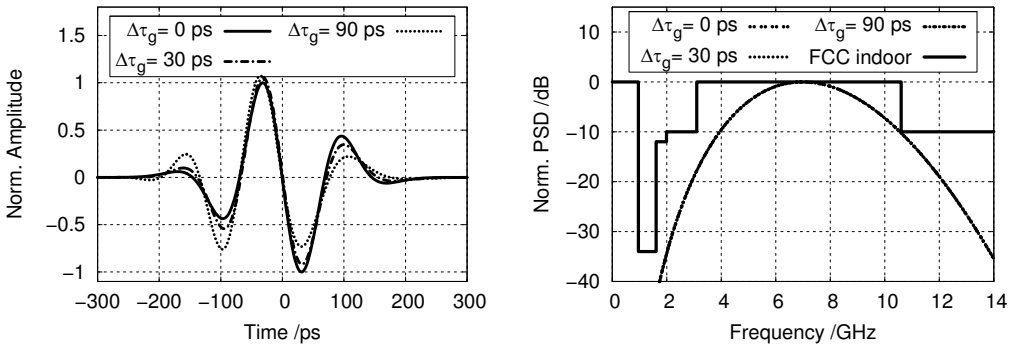

(a) (b)

Figure 2.8: Influence of components with different linear group delay variations on the impulse shape of a fifth Gaussian derivative plotted in (a) time and (b) spectral domain.

bandwidth. However, the influence on the signal does depend on the curve shape of the group delay, too. To show the effect a further artifical filter is set up, which only changes the phase performance and therefore the group delay characteristic between input and output signal at different frequencies. The effect of changing the group delay variation on an input impulse can be seen in an example in Fig. 2.8, where a fifth Gaussian derivative is numerically fed through different filters with linearly increasing group delay variations $\Delta\tau_g$ from one edge to the other in the 3.1–10.6 GHz band. As can be seen, the shape of the output impulses changes from a symmetrical to a more and more asymmetrical shape while there is no influence on the spectral magnitude.

A further distortion of the impulse shape can be initiated by reflections, occurring at discontinuities in the signal path. These discontinuities can be connectors, line transitions, bondwires, for example, or may be due to multipath propagation. Albeit small, these reflections will merge with the desired waveform, thus distorting the original impulse depending on its amplitude, sign and relative location in time with respect to the original waveform. Fig. 2.9 (a) illustrates an example of a summation of an impulse and a delayed and attenuated reflected impulse. The reflected impulse has 20 % of the original impulse amplitude, a non-inverted shape and a time delay $\tau_r = 130$ ps. When the impulse and the reflection merge, the summed waveform has changed compared to the original waveform, as can be seen in Fig. 2.9 (a) in the time domain. The change in spectral shape is shown in Fig. 2.9 (b), which compares

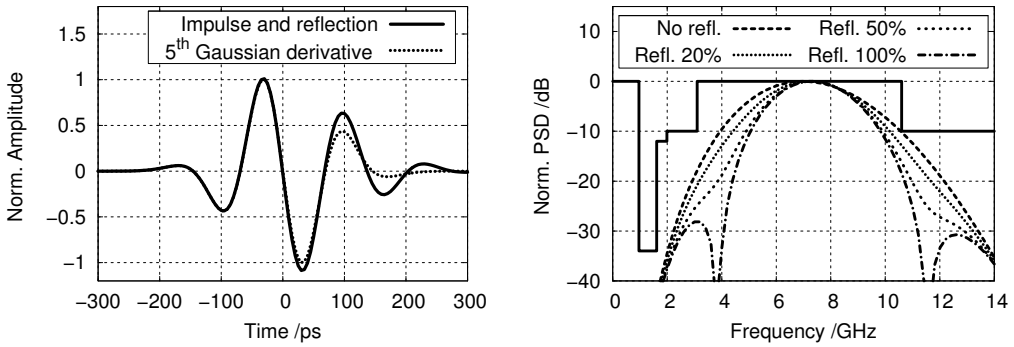

Figure 2.9: Comparison between the original fifth derivative impulse and a merged impulse with a reflection having a delay of 130 ps (a) and a relative reflection impulse amplitude of 20 % in time domain and (b) with different relative amplitudes in frequency domain.

the original impulse and merged impulses with a delay $\tau_r = 130\,\text{ps}$ and non-inverted shape, but different relative amplitudes of the reflected impulse. As can be seen, repeated notches in the impulse spectrum are occurring, which have a spectral distance $\Delta f_r = 1/\tau_r \approx 7.69\,\text{GHz}$. The frequency location of the lowest notch is placed at $f_r/2$ for a non-inverted reflection and at f_r for an inverted reflection. The time-domain graph in Fig. 2.9 (a) illustrates that due to the impulse nature the reflection behavior differs from standing-wave conceptions of classical sinusoidal-based systems because the impulse lasts only for a short time period. This involves that the original impulse will always be broadened in time by reflections, and the impulse can only be totally canceled by an inverted impulse in combination with a time delay of the repetition rate f_{rep}. Measurements on this will be presented in Sec. 4.4.1, when dealing with multipath effects.

In general, it is difficult to give boundary values for the presented three linear distortion effects. Ripples of the attenuation, as well as minima and maxima of the group delay variation may occur at all locations in the UWB band, not necessarily at the boundaries as presented here. Additionally, reflections can occur with different amplitudes and at different locations. But the examples presented may help to understand the general distortion behavior and thus help to reduce the effects in component and system design, accordingly.

2.3 Basic IR-UWB Transceiver Concepts

Transceiver concepts are intensively investigated in current IR-UWB studies. In general, two main receiver structures can be found (cf. [21,23]), which are the basis for advanced transceiver implementations, as described, for example, in [24–26].

2.3.1 Energy-Detection Receiver

The easiest receiver concept for IR-UWB systems is the energy-detection receiver. It consists of a receive antenna, a squaring circuit and an integrator. A block diagram of such a receiver can be seen in Fig. 2.10 (a). In Fig. 2.10 (b) an illustration of the signals present at each output of the components of an energy-detection receiver is shown for a fifth Gaussian derivative waveform. A digital information transmission can be done by a simple on-off-keying (OOK) modulation. Advantages of the basic energy-detection receiver are that it consists of a very simple system architecture and that it requires no synchronization between transmitter and receiver. One

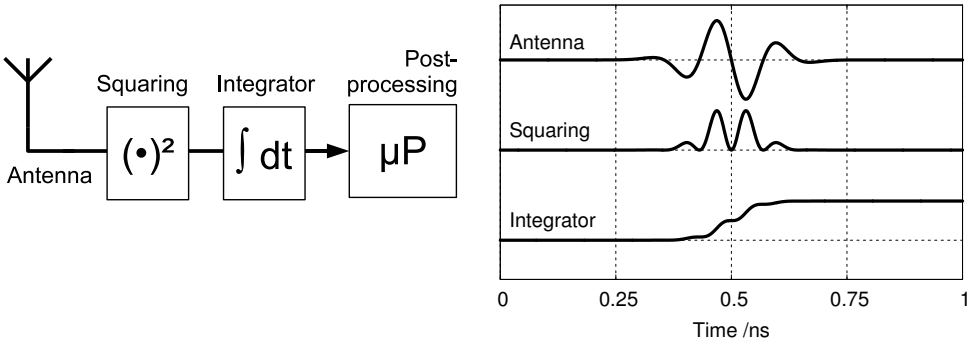

(a) (b)

Figure 2.10: (a) Block diagram of an energy-detection receiver. (b) Illustration of the signals at the output of the components in an energy-detection receiver.

disadvantage of such a receiver is that because of the squaring operation it is very insensitive to low level signals. Furthermore, in its basic form, it is not robust to in-band interferers and not usable in an IR-UWB multi-user environment.

2.3.2 Correlation-Detection Receiver

A different receiver concept applies the cross-correlation operation and is therefore known as correlation-detection receiver [21]. Mathematically, the complex cross-correlation function $CCF_{s,g}$ is defined in its general form as

$$CCF_{s,g}(\tau) = \int_{-\infty}^{t=+\infty} \left(s^*(t) \cdot g\left(t+\tau\right)\right) \mathrm{dt} \,, \tag{2.7}$$

where s and g are two different functions in time (here: the Gaussian derivative impulses) and τ a time shift between the functions [27]. When only real signals are applied, as done here, the complex conjugate of s does not need to be taken. The cross-correlation function is a measure for the similarity of the functions s and g and obtains its maximum value when s and g are time-aligned to each other. When s and g are the same function, this special case is called autocorrelation function ACF_s. The cross-correlation receiver is the classical matched-filter receiver for IR-UWB communication systems for best signal-to-noise ratio performance in additive white Gaussian noise (AWGN) channels [23, 27].

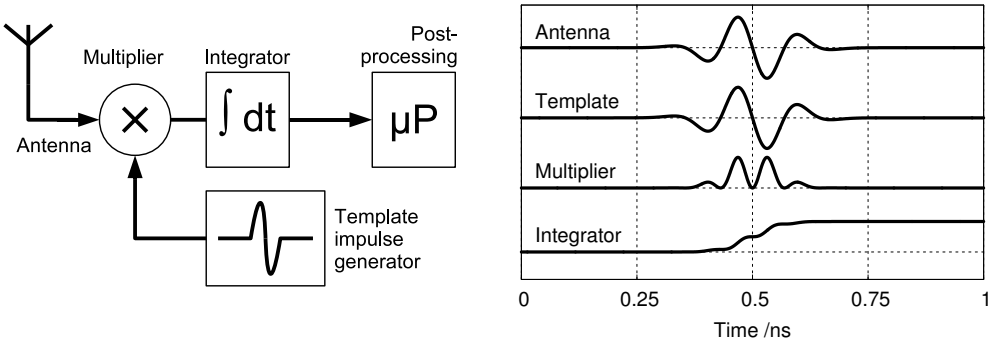

(a) (b)

Figure 2.11: (a) Block diagram of a correlation-detection receiver. (b) Illustration of the signals at the output of the components in a correlation-detection receiver with ideal overlap ($\tau = 0$) of receive and template impulse.

Fig. 2.11 (a) shows a block diagram of a correlation-detection receiver, which consists of a receive antenna, a template impulse generator using the same basic waveform as the received antenna signal, a four-quadrant multiplier and an integrator. Fig. 2.11 (b) depicts a principle simulation of the signals appearing in a correlation receiver using fifth Gaussian derivative waveforms and time shift $\tau = 0$ ps. As can be seen, the received impulse and the template impulse require a precise time alignment to each other; otherwise the correlation maximum is not reached.

The influence of applying different time shifts τ between the two impulses can be investigated by plotting the correlation function (2.7) versus τ. Fig. 2.12 presents a comparison of correlation functions using the autocorrelation of the fifth Gaussian derivative ACF_5, the autocorrelation of the seventh Gaussian derivative ACF_7 and a cross-correlation of a fifth with a seventh Gaussian derivative $CCF_{5,7}$. In Fig. 2.12 (a) all correlations curves are normalized to the maximal value of ACF_5. This plot shows that the correlation functions in all three cases are very similar. As can be seen, ACF_7 has a correlation value of 1.25 when normalized to the maximal value of ACF_5. This comes from the fact that the seventh Gaussian derivative obtains a longer impulse length than the fifth Gaussian derivative and therefore the integration sum of its autocorrelation is larger. The $CCF_{5,7}$ also shows a slightly increased correlation value of 1.08 compared to ACF_5 for the same reason. Especially, as shown in Sec. 2.2.4, the comparison with $CCF_{5,7}$ indicates that impulses transmitted through a bandlimited arrangement can be equally used for correlation detection. In Fig. 2.12 (b), all curves are normalized to unity. This plot illustrates

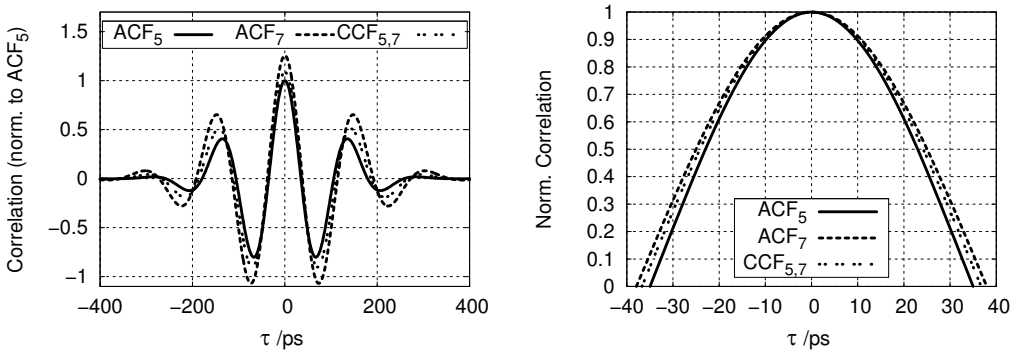

(a) (b)

Figure 2.12: Comparison of the autocorrelation of the fifth Gaussian derivative (ACF_5), the autocorrelation of the seventh Gaussian derivative (ACF_7) and the cross-correlation of the fifth with the seventh Gaussian derivative ($CCF_{5,7}$) versus time shift τ. In (a) the functions are shown normalized to the maximal value of ACF_5. In (b) a detail of the functions in the vicinity of the correlation maximum is presented normalized to unity.

that even a slight time misalignment of 10 ps between the impulses, for example, results in a decrease to 90% of the maximum correlator output amplitude.

2.3.3 Impulse Modulation Methods

Impulse modulation methods shall be presented very briefly and for the sake of completeness only, because the innovative analog modulation scheme presented in Sec. 4 differs from current digital modulation methods. Currently proposed modulation methods using ultra-wideband impulses apply a quantized and discrete modulation to each impulse. In general, there are two main modulation techniques discussed in specialist literature: pulse-amplitude modulation (PAM) and pulse-position modulation (PPM) (cf. [21, 23]). Fig. 2.13 shows extracted sequences of these modulation methods.

In PAM the amplitude of the impulses is modulated with the digital information signal. Two special cases are on-off-keying (OOK) modulation, in which either an impulse or no impulse is transmitted, and binary phase shift keying (BPSK) or biphase modulation, in which the impulse or the inverted replica of the impulse is transmit-

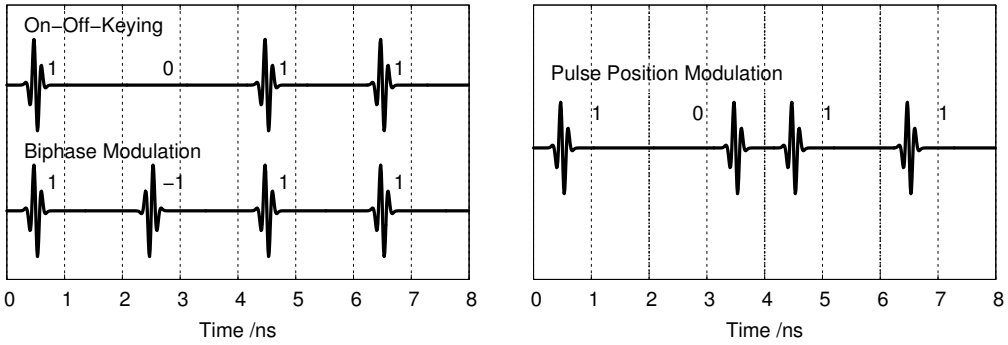

Figure 2.13: IR-UWB modulation methods using (a) pulse-amplitude modulation and (b) pulse-position modulation techniques.

ted. In PPM the impulse orientation remains unchanged, but the impulse is transmitted at different positions in time. In combination with an energy-detection receiver, only OOK modulation can be used. For correlation-detection receivers all three modulation methods can be applied, using appropriately modified receiver structures. A detailed performance comparison on the modulation methods presented is given e.g. in [28].

3 IR-UWB Radar Sensor for Location Tracking and Movement Detection

A measurement of the human breath-rate with impulse-radio UWB technology is introduced first in the two patents by Thomas McEwan [29, 30] in 1996 and 1998, respectively. He proposes a method transmitting an ultra-wideband spike to open a range-gate in which the breathing pattern of a test person can be detected and determined. The demonstrator system built by Stephen Azevedo and Thomas McEwan, operating in the lower part of the FCC spectrum, is described in [31, 32]. In the following years, many research groups have picked up McEwan's idea and have proposed refined IR-UWB sensors for breathing measurements, examples being Enrico Staderini et al. [33, 34] or, based on Staderini's concept, Florian Michahelles et al. [35]. Both groups demonstrate breathing measurements using low-frequency UWB emissions, even though detailed measurements of their systems and the impulses applied are missing. Gerald Ossberger and a group at Linz University report on a hybrid impulse generator using a step-recovery diode and discuss breathing measurements using an undersampling receiver system [36]. Several IR-UWB systems are investigated by Igor Immoreev and co-workers; in [37] they describe an impulse with a peak emission at 1 GHz; in the system proposed in [38], they are using an impulse with a center frequency of 6.75 GHz and a time duration of 2 ns and apply a correlation-detection receiver. In both publications breath-rate measurements are given. A UWB concept using an M-sequence generator and rectangular waveforms, which do not show compliance to the allocated UWB masks, is used by Jürgen Sachs and collaborators from TU Ilmenau in [39–42]. The group demonstrates breathing measurements using an undersampling receiver technique. Amer Nezirovic et al. measure the breath-rate by applying Gaussian bell-shaped impulses, which do not comply to any UWB mask [43, 44]. Breathing measurements with FCC mask-conform impulses are discussed by Michael Chia et al. in [45]. Their hardware makes use of the lower 3.1–6 GHz part within the FCC regulation.

In this chapter circuits and software for a radar sensor using UWB impulses are presented, and a radar-sensor testbed is described which makes use of the entire FCC-allocated frequency mask for indoor applications. By making use of the complete

band, the impulses created by this testbed show the smallest time-domain extension for compliance to the mask and are therefore best suited for a high-resolution ranging. Using monolithic hardware components results in a very compact sensor prototype, and with this prototype different concepts for an ultra-fine movement detection are studied and compared. The radar sensor's hardware and software will be explained and verified by detailed measurements.

3.1 Introduction to Breath-Rate Sensing

The idea behind medical diagnostics using electromagnetic waves is to use the reflections of the waves occurring at the tissue boundaries of the person under examination. The reflections occur due to a change in the dielectric properties of the materials or tissues penetrated. The amount of electromagnetic reflection can be calculated by the reflection coefficient Γ using

$$\Gamma = \frac{Z_1 - Z_0}{Z_1 + Z_0}\,, \tag{3.1}$$

where Z_0 represents the characteristic impedance of the material the wave is starting from and Z_1 the characteristic impedance of the material or tissue the wave is penetrating. The general characteristic impedance Z_x can be calculated in the simplified case of a lossless, non-magnetic material by

$$Z_x = \sqrt{\frac{\mu_0}{\epsilon_0 \epsilon_{r,x}}}\,, \tag{3.2}$$

where $\mu_0 = 4\pi \cdot 10^{-7}$ H/m is the vacuum permeability, $\epsilon_0 = 8.85 \cdot 10^{-12}$ F/m the vacuum permittivity and $\epsilon_{r,x}$ the relative permittivity of material x (cf. [46]). In the scenario of measuring the breath rate, the radiated impulse first travels through air, which has a relative permittivity $\epsilon_r = 1$ and therefore a characteristic impedance $Z_0 = 377\,\Omega$. Then the impulse hits the skin of the person monitored. In the FCC frequency range of 3.1–10.6 GHz, (dry) human skin has a relative permittivity $\epsilon_r \approx 40$, see [47]. This results in a characteristic impedance $Z_1 = 60\,\Omega$. Inserting the two values in (3.1) results in a reflection coefficient $\Gamma \approx$ -0.72, which means that 72 % of the signal amplitude is reflected back at the air-skin interface. Furthermore an inversion of the time-domain impulse shape takes place, indicated by the minus sign. A further contribution to the reflected impulse energy will come from the part of the impulse energy penetrating the skin, not being absorbed by the lossy tissue and being re-

flected at deeper tissue boundaries, but this contribution plays a minor role only. The reflected impulse is collected by a receiver system and its relative arrival time is determined, which represents the movement of the thorax excursion when breathing, for example. However, it has to be taken into account that the curved shape of the human body (e.g. the chest) can diffract the incident impulse in a complex way.

3.2 IR-UWB Components for the Radar Demonstrator

In this section the applied circuits are presented and characterized for the use in the IR-UWB system. The integrated circuits (ICs) are designed and fabricated in the SiGe heterojunction bipolar transistor (HBT) technology with a 0.8 µm minimum drawn feature size from Telefunken Semiconductors with transistors having $f_T/f_{max} = 80/90$ GHz and $BV_{CEo} = 2.4$ V [48, 49].

3.2.1 Impulse Generator Fitting the FCC Indoor Mask

For this study an impulse generator for the FCC indoor mask was available through the previous studies of [1]. Its concept is briefly repeated here for clarity and measurements are shown to prove the applicability of the circuit for the intended task. The impulse generator consists of three main subcircuits. Its block diagram is given in Fig. 3.1.

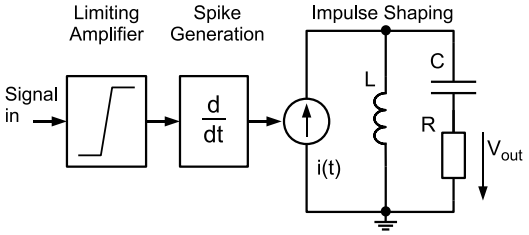

Figure 3.1: Block diagram of the impulse generator IC applied.

The first subcircuit is a two-stage limiting amplifier. It is excited with an input trigger signal and is used to convert the input signal from a potentially long rise-time signal into a rectangular signal with a short rise time. The circuit can be operated by a sinusoidal input signal, too. The rising slope of the short rise-time signal is differentiated by the spike-generation subcircuit, which forms a short-width, Gaussian-like output spike. The corresponding negative spike, coming from the falling slope

of the rectangular signal, is suppressed. In the third subcircuit, the impulse forming takes place. The Gaussian-like spike activates a transistor-controlled, underdamped LC-resonator. At the output a transient impulse is formed, which is very similar to a fifth derivative of a Gaussian bell shape with a $\sigma = 51$ ps. A deeper insight into the impulse generator design can be found in [1, 50, 51].

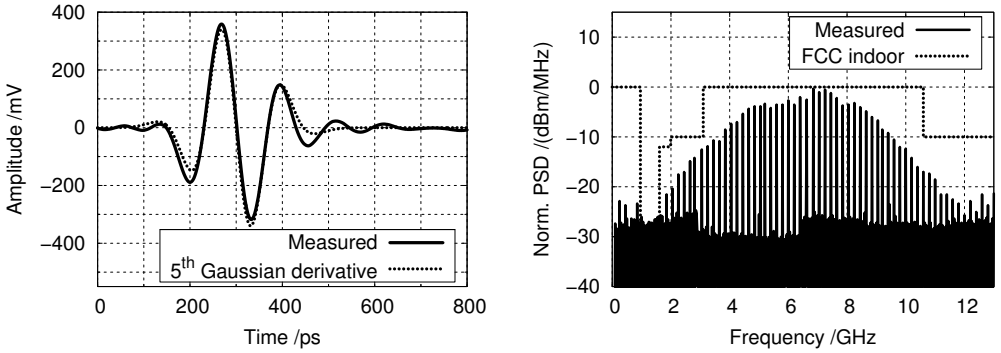

(a) (b)

Figure 3.2: Measurements of the FCC-compliant impulse generator IC in (a) time and (b) spectral domain.

The on-chip measured output impulse in time domain is shown in Fig. 3.2 (a), compared to an ideal fifth Gaussian derivative, proving the close fit to the waveform. As discussed, the fifth derivative of a Gaussian impulse generates a spectrum which fits the FCC UWB frequency allocation for indoor applications. The measured on-chip output signal in spectral domain can be seen in Fig. 3.2 (b). Here, a sinusoidal input trigger signal of 200 MHz is chosen. The IC has an overall power consumption of 38 mW.

As discussed in Sec. 2.3.2, it is crucial for a correlation-detection receiver that the time shift between the impulses is kept very precise and stable in order to avoid a decrease in correlation amplitude. This decrease will occur, for example, when the impulses jitter, which means that small random deviations in the time position with respect to the absolute position occur. This jittering of the impulse signal consist of a jitter part coming from the externally-fed trigger signal and an additional jitter component induced by the circuit operation of the impulse generator. For a characterization of the IC, the additional jitter of the impulse generator circuit is estimated in a time-domain and a phase-noise measurement; however, a precise determination of the additional jitter is not done here. In time domain an additional jitter can be

estimated by a comparison of the time broadening between the slopes of the trigger and the impulse signal, when plotted in infinte persistance mode on an oscilloscope. Fig. 3.3 (a) shows such an oscilloscope picture of the trigger signal together with the output impulse. In case of a large additional jitter, the measured output signal of the impulse generator will show a visible broadening of the impulse shape compared to the trigger signal. The trigger signal in Fig. 3.3 (a) is split by a power divider and fed to the impulse generator and to the first oscilloscope channel.The output signal of the impulse generator is fed to the second channel of the oscilloscope with which the two signals can be compared. As can be seen, the broadening of the two lines is very much the same, indicating the small amount of additional jitter of the impulse generator IC.

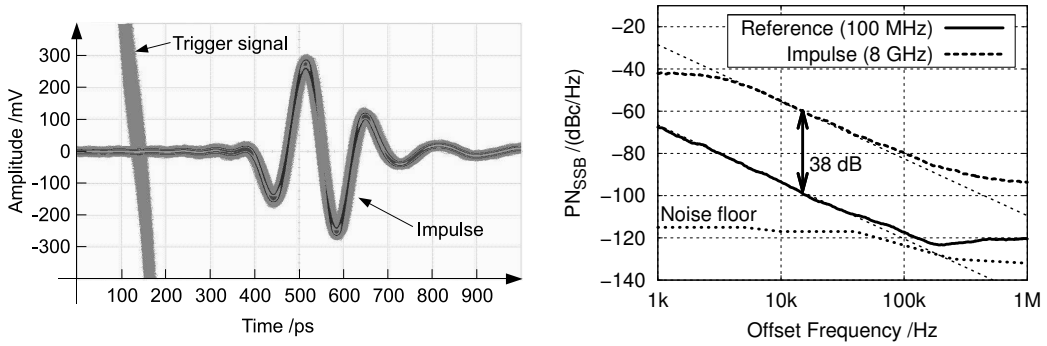

(a) (b)

Figure 3.3: Evaluation of the impulse generator's jitter behavior in (a) time domain and (b) by a phase noise measurement. The 38 dB offset is the theoretically expected value from the harmonic order of the 8 GHz spectral line.

The evaluation of the impulse-generator jitter performance by a phase-noise measurement is adopted from [52, 53]. It uses the increase in single-sideband phase noise of higher harmonics compared to the fundamental trigger signal. The increase in single-sideband phase noise PN_{SSB} of a higher harmonic can be calculated by

$$\Delta PN_{SSB} = 20 \cdot \log_{10}(N)\,\mathrm{dB}\,, \tag{3.3}$$

where N is the order number of the harmonic [54]. Fig. 3.3 (b) shows a comparison of the phase-noise measurement of the 100 MHz impulse generator trigger signal and the 8 GHz spectral harmonic of the impulse-generator signal. The measurement

is done using the direct spectrum phase-noise measurement option of a spectrum analyzer [55, 56] with which pulsed sources can be measured, too. The disadvantage of this method is its limitation by the noise floor of the spectrum analyzer. Therefore, sources with a good phase noise performance cannot be measured with the direct spectrum method. Consequently, a 100 MHz trigger signal with a comparably poor phase-noise performance is used for the phase-noise characterization. Fig. 3.3 (b) illustrates that the measured reference trigger signal above 100 kHz is already approaching the noise floor of the spectrum analyzer [57, 58], resulting in a plateau[1]. As a trade-off the measured phase-noise curve of the 8 GHz harmonic signal has a very strong phase noise and shows a plateau at frequencies below 5 kHz. This results, when the spectrum analyzer's IF filter is completely filled by the jittering signal component of the impulse. But in the range of approximately 5 kHz to 100 kHz, a comparison of both curves is reliable. In Fig. 3.3 (b) the offset of $\Delta PN_{SSB} = 20 \cdot \log_{10}(8\,\text{GHz}/\,100\,\text{MHz}) = 38\,\text{dB}$ between the two signals is plotted for evaluation. It can be seen that the measured increase in phase noise fits the theoretical prediction. Together with the time domain measurement, this leads to the conclusion that the additional jitter is negligibly small and the impulse generator is suitable for the use in an IR-UWB correlation-detection receiver.

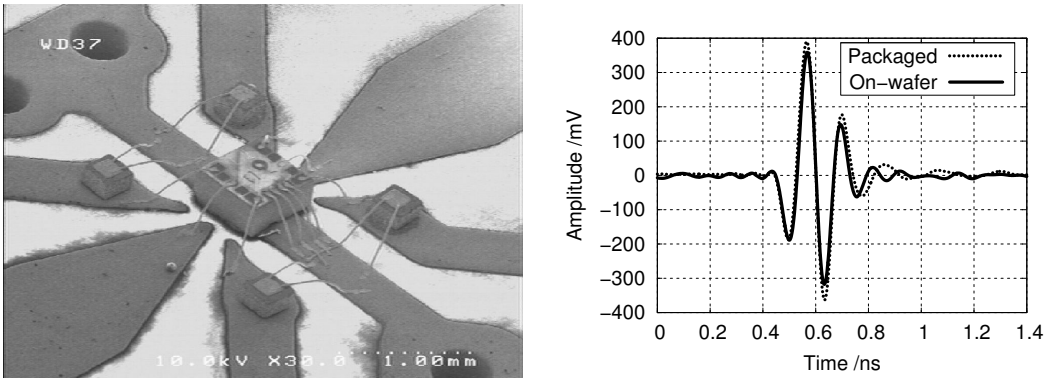

(a) (b)

Figure 3.4: (a) SEM picture and (b) comparison between packaged and on-chip measured output impulse shape of the FCC-compliant impulse generator IC.

For packaging reasons, the impulse generator is glued chip-on-board on top of a RO4003 substrate and is connected with bondwires to the input, output and supply

[1]The phase-noise utility manual [58] specifies an amplitude accuracy of ±2.5 dB at >10 dB above system noise floor.

lines of the circuit board. Commercial voltage regulators were used to supply the circuit from a common DC voltage. In Fig. 3.4 (a) a micrograph of the packaged circuit and in Fig. 3.4 (b) a comparison of the measured output amplitudes can be seen. The packaging has only a negligible influence on the shape of the impulse. The output amplitude of the packaged IC is slightly larger because the housing was connected directly to the oscilloscope, thus omitting the attenuation of the feeding lines used in the on-chip measurement.

3.2.2 FCC-Compliant Correlation Receiver

To avoid sampling of the high-frequency UWB signal a hardware correlation receiver is built, according to the cross-correlation operation introduced in Sec. 2.3.2. The receiver combines an FCC-compliant correlator IC with a baseband circuit. A block diagram of the complete correlation receiver is given in Fig. 3.5 (a). The correlator IC was available for the project; a detailed description of this IC can be found in [1, 59].

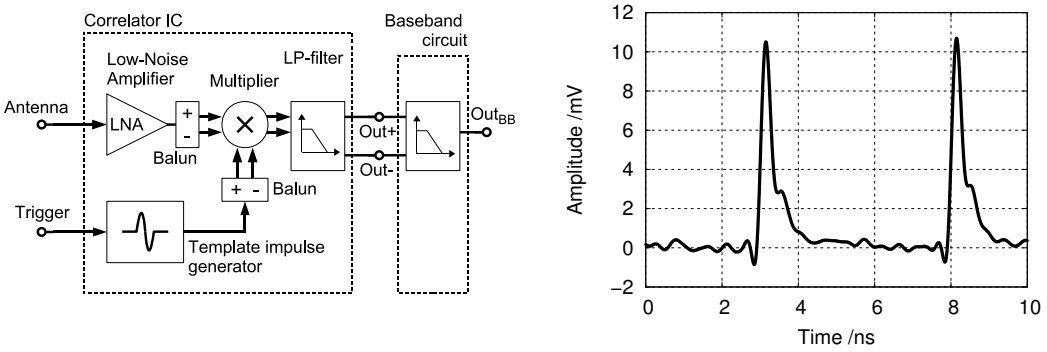

(a) (b)

Figure 3.5: (a) Block diagram of the hardware correlation receiver applied. (b) Measured differential output signal of the correlator IC for an ideal alignment ($\tau = 0$ ps) of receive and template impulse at a 200 MHz repetition rate.

The correlator IC consists of a low-noise amplifier (LNA), a template impulse generator, a multiplier and a first integrating low-pass filter. The performance of the UWB low-noise amplifier is evaluated in detail in Sec. 4.2.1; the template impulse generator is the same as the fifth Gaussian derivative FCC-compliant impulse generator shown in Sec. 3.2.1. For multiplication operations a four-quadrant multiplier is

necessary. Therefore a fully balanced Gilbert-cell topology is applied, and converters (baluns) are placed at the input for a conversion of the single-ended LNA and impulse generator output signals to the differential inputs of the Gilbert-cell. The output port of the multiplier remains differential. The multiplier output is filtered by a first integrating low-pass filter with a cut-off frequency of around 800 MHz. To measure the output signal of the correlator IC, the output ports ($Out+$, $Out-$) are connected with DC blocks to two channels of a wideband oscilloscope. The DC blocks are necessary in order not to detune the correlator ICs internal biasing by the 50 Ohm impedance of the wideband oscilloscope. $Out-$ is subtracted mathematically from $Out+$ to show the differential signal content on the display. An attenuated fifth Gaussian derivative impulse signal is applied to the antenna input of the circuit. Two synchronized signal sources are connected to the inputs of the external impulse generator and the internal template impulse generator to provide an adjustable trigger signal. Fig. 3.5 (b) shows a measured output waveform in which the antenna and the template impulse are aligned at $\tau = 0$ ps for maximum correlation.

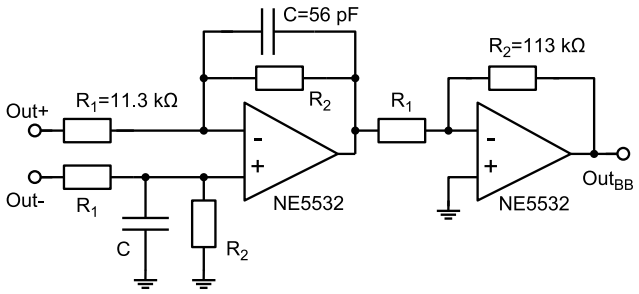

Figure 3.6: Simplified schematic of the baseband circuit using two operational amplifiers.

To further process these signals, a baseband circuit is connected externally to the output of the correlator IC, which first provides a conversion from differential to single-ended, secondly amplifies the output signals and additionally applies further integration by a strong low-pass filtering. The applied circuit, which provides all three operations, is presented in Fig. 3.6. It is based on a differential amplifier [60] enhanced with a single-pole low-pass filter in both branches. Due to its high input impedance, the baseband circuit can be connected directly to the correlator IC's output without distorting the correlator IC's internal biasing. A second operational amplifier stage is cascaded for a further gain increase. The voltage gain of each stage is set by $G_V = -R_2/R_1 = -10$, and the filter's 3 dB corner frequency is adjusted

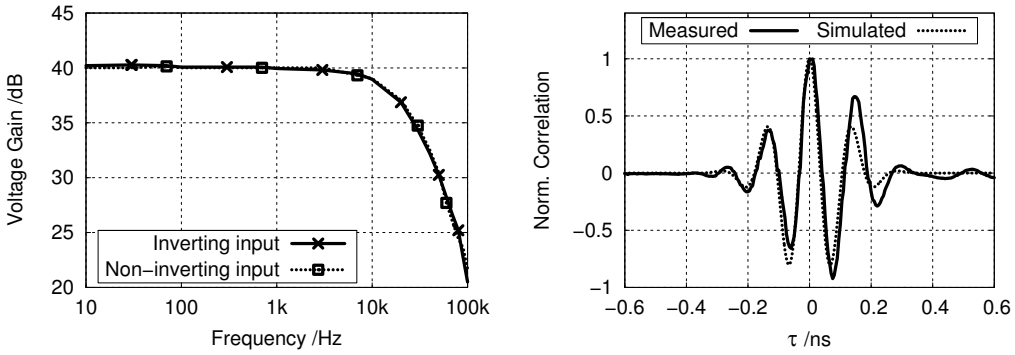

(a) (b)

Figure 3.7: (a) Voltage gain of the baseband circuit. (b) Measured correlation of the built correlation receiver, compared to the autocorrelation function of a fifth Gaussian derivative impulse.

to $f_{LP} = 1/(2\pi \cdot R_2 \cdot C) = 25\,\text{kHz}$. A measurement of voltage gain versus frequency is given in Fig. 3.7 (a) for both inputs of the baseband circuit. The operational amplifier is supplied with a positive and a negative supply voltage. The negative voltage is generated by a switched-capacitor voltage converter from the general voltage supply of the correlation receiver. The baseband circuit with regulators consumes 23 mA at a 9 V supply. The IC with baseband circuit contains all building blocks necessary for a correlation receiver, as discussed in Sec. 2.3.2. To show the correlation abil-

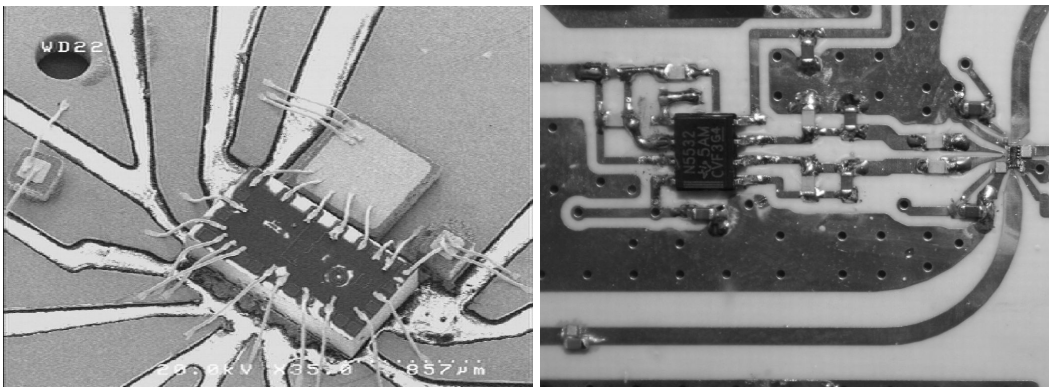

(a) (b)

Figure 3.8: (a) Micrograph of the correlator IC placed chip-on-board on the antenna substrate and (b) photograph of the complete correlation receiver.

ity of the correlation receiver, a measurement, using an externally connected input impulse as described above, is performed with varying time delay τ between the impulses. The measured normalized correlation plot can be seen in Fig. 3.7 (b), in which it is compared to an ideal autocorrelation of a fifth Gaussian derivative. The curve shows a clear correlation maximum and can therefore be used for the intended sensor. The deviations from the ideal correlation shape are due to the varying group delay in the multiplier and to reflections at interface boundaries of the components. For this circuit, a packaging method is implemented, too, which integrates the IC and the baseband circuit in a compact arrangement on the antenna substrate. Fig. 3.8 (a) shows the chip-on-board mounted correlation IC, and in Fig. 3.8 (b) the complete correlation receiver, using surface mount device (SMD) components, is shown.

3.2.3 UWB Directional Antennas

UWB directional antennas and the antenna characterization measurements were provided through the project collaboration with the Institute of Microwave Techniques at Ulm University. Due to its very broadband behavior, a Vivaldi antenna is chosen, which is formed by an exponentially tapered slot on a microwave substrate [61]. In order to feed the antenna with a microstrip line, enabling connection to the ICs, a broadband transition to the slot line is needed. This is achieved by using a planar Marchand balun with circular open and short circuits in microstrip

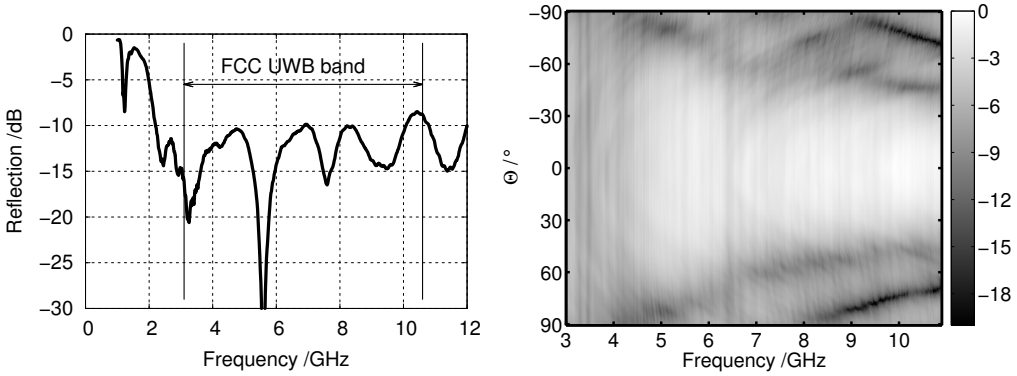

(a) (b)

Figure 3.9: (a) Measured matching performance of the Vivaldi antenna. (b) Measured Vivaldi antenna radiation diagram in H-plane for the co-polarization.

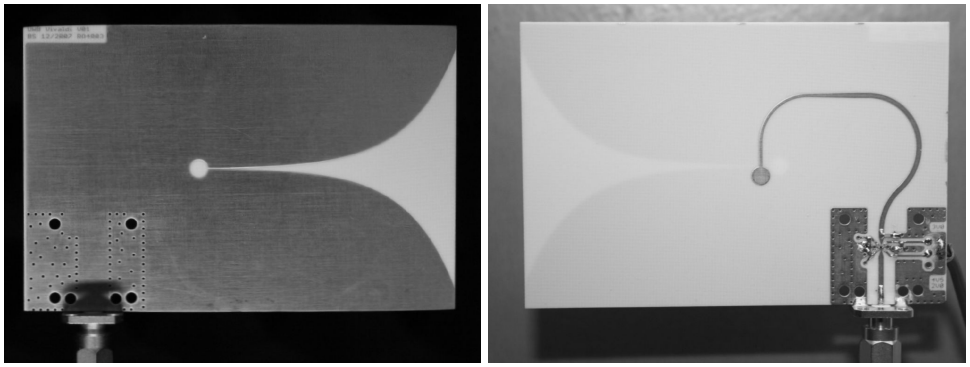

(a) (b)

Figure 3.10: Photograph of the Vivaldi antenna, (a) frontside view of the tapered radiating slot and (b) backside view of the microstrip feeding line and mounted impulse generator.

and slot line techniques [62]. On the used microwave substrate, RO4003 with a substrate height of 0.5 mm, a return loss of more than 10 dB is obtained in the desired frequency range, as shown in the measurement of Fig. 3.9 (a). The measured antenna radiation diagram in co-polarization and rotated in the H-plane can be seen in Fig. 3.9 (b). The antenna's main radiation direction is in the direction of the tapered slot and the antenna gain increases with frequency. For 3.1 GHz, a gain of 3 dBi is achieved; the maximum value is 9.3 dBi. A picture of front- and backside of the transmit antenna is presented in Fig. 3.10.

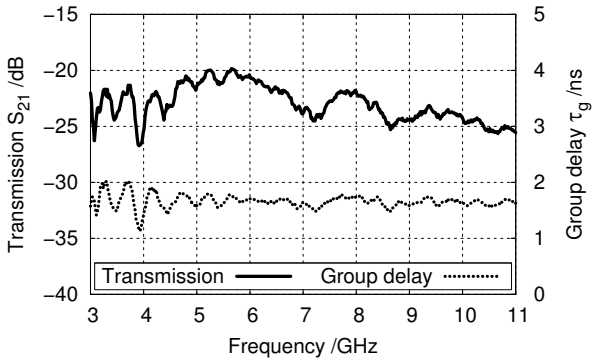

Figure 3.11: Transmission and group delay measurement of two Vivaldi antennas at a spacing of 24 cm.

As the group delay of the signal from the antenna is quite constant over frequency, the antenna is well suited for impulse radiation. This is demonstrated by an S-parameter measurement by which the transmission behavior between two Vivaldi antennas is determined. There, the antennas are facing each other and are separated by 24 cm. As can be seen in Fig. 3.11, the amplitude and the group delay over frequency are acceptably small. The small variations over frequency are caused by the antenna matching behavior, multiple reflections at the metallic antenna holders and parasitic radiation on the feeding structure.

3.3 Transmission Evaluation

For the system, the ICs are mounted directly on the feeding lines of the antennas, as for example Fig. 3.10 (b) shows for the impulse generator circuit. This avoids the formation of reflections which occur at discontinuities on the transmission lines, for example at bends, or at the connectors. Using the Vivaldi antenna with the mounted FCC-compliant impulse generator, a transient transmission measurement is performed. For this, a signal source generating a 200 MHz sinusoidal signal is connected to the trigger input of the impulse generator, causing an impulse train of fifth Gaussian derivative impulses with a repetition rate of 200 MHz to be transmitted by the antennas. A receiving antenna without electronics is connected to an

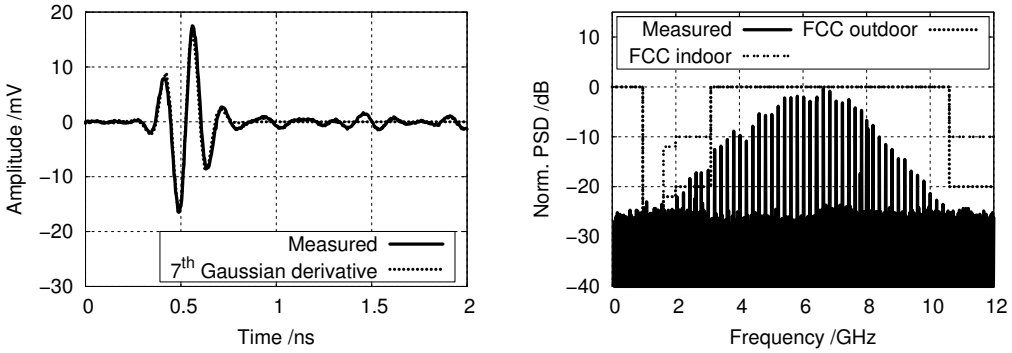

(a) (b)

Figure 3.12: Received impulse in (a) time domain, compared to a seventh derivative with a $\sigma = 65$ ps, and in (b) spectral domain, compared to the FCC indoor and outdoor masks.

oscilloscope, which is triggered through the 10 MHz synchronization reference of the signal source. The antennas are placed at a distance of 15 cm facing each other.

In Fig. 3.12 (a) the measured transient result of the transmitted impulses can be evaluated. It can be fitted well to a seventh Gaussian derivative with a $\sigma = 65$ ps, as predicted for band-limited systems in Sec. 2.2.4. Fig. 3.12 (b) depicts the spectrum of the measured impulse train at the output of the receiving antenna. The spectral shape fits the allocated FCC outdoor mask at the higher edge, but cuts the mask at the lower boundary. It can be seen that the impulse has only a small ringing, which again qualifies the Vivaldi antennas as broadband radiating elements. As discussed in Sec. 2.3.2, the impulses can be used for a correlation detection because the cross-correlation function using fifth with seventh Gaussian derivative impulses ($CCF_{5,7}$) is very similar to the ideal autocorrelation function of a fifth Gaussian derivative (ACF_5).

3.4 Radar Using Undersampling Reception

Using the Vivaldi antenna with mounted impulse generator, a first radar demonstrator fulfilling the spectral requirements of the FCC mask is built. For this setup, the transmit antenna is placed in a collinear alignment to a plain Vivaldi receive antenna at a distance of 10 cm. As can be seen in the block diagram of Fig. 3.13, the transmitter is supplied by a sinusoidal trigger signal, causing an impulse repetition rate of 200 MHz. The receive antenna is connected directly to a sampling-type os-

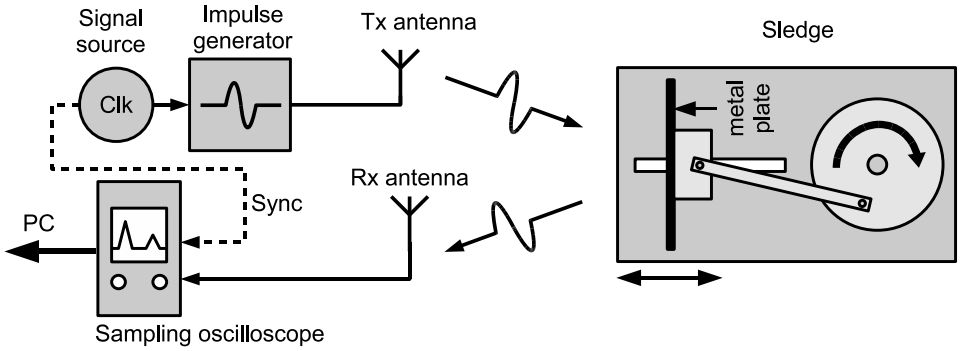

Figure 3.13: Block diagram of the radar demonstrator using undersampling reception.

cilloscope and is triggered by the 10 MHz synchronization reference of the signal source.

An impulse train is transmitted, and the reflected signal of an object in front can be received and monitored. The sampling-type oscilloscope used has a 20 GHz bandwidth and applies an undersampling acquisition of the impulses, for which it requires a periodic impulse train to reconstruct the impulse shape. In the present case of a slowly moving object, the impulse shape can be reconstructed well. From the sampling oscilloscope, the general purpose interface bus (GPIB) transfers the 511 data points displayed on the screen to a personal computer with a transfer rate of 3 Hz. The transfer speed is limited by the speed of the sampling oscilloscope. In order to increase the transfer speed, a different sampling device would be necessary. The measured data is processed immediately on the computer by a method similar as proposed in [36], but in contrast to a continuous wavelet transform, a much simpler cross-correlation procedure is applied here. The correlation maximum is continuously monitored and refers to the position of the object. The measurement procedure consists of two steps. In the first step, present background emission is determined in absence of any object in front of the arrangement. The background emission contains all static reflections and the crosstalk impulse of the direct coupling between the antennas. In the presented measurement, a mean of 30 background data sets are used and averaged. In the second step, the measurement is performed with the object. The background signal is subtracted from every data set to improve the measurement and correlation process. The procedure can be seen in Fig. 3.14 (a).

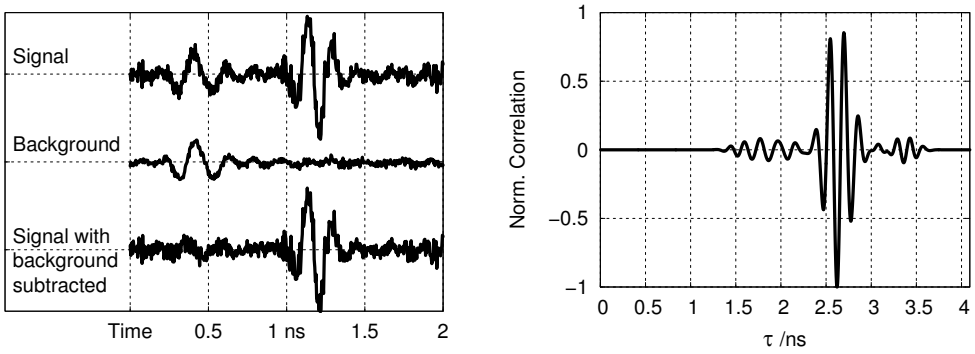

Figure 3.14: (a) Procedure of background emission removal from the measured signal. (b) Calculated correlation of the background-free signal.

To assess the principle, at first an aluminum plate of 12 x 15 cm^2 is placed in front of the antenna arrangement at a distance of approximately 15 cm. This metal plate is placed on a sledge which can be moved forward and backward by an eccentrically mounted lever, resulting in a sinusoidal movement (see Fig. 3.13). The deviation amplitude of the movable sledge can be adjusted by the position of the lever on the rotation table.

One acquired oscilloscope data set of the directly coupled signal and the signal reflected at the metal plate is presented in Fig. 3.14 (a). The peak-to-peak amplitude of the impulse reflected at the metal plate is approximately 20 mV. From this measured curve, the signal from the background is removed, as can be seen as well in Fig. 3.14 (a). The cross-correlation function is then calculated between the background-free signal and an ideal seventh Gaussian derivative with a $\sigma = 65$ ps, as the example in Fig. 3.14 (b) shows. The cross-correlation curve appears inverted because the reflection at the metal plate produces a signal inversion. The minimum of the correlation signal is monitored. When the metal plate is moving, the minimum of the correlation signal moves with respect to the position of the metal plate. The relative distance Δs can be calculated by

$$\Delta s = \frac{c_0 \cdot \Delta\tau}{2} \ , \tag{3.4}$$

were c_0 is the speed of light and $\Delta\tau$ the arrival time difference between the minimum of two data sets. The theoretical point-to-point precision of the measurement can be determined using the time resolution of the data points in the sampling oscilloscope. Here a time window of 2.044 ns is used. Divided by the 511 data points, a minimal time step of 4 ps between each data point is resolved in the sampling oscilloscope. By using (3.4), a best case resolution of 0.6 mm can be achieved, when applying the simple minimum-detection algorithm. Fig. 3.15 presents a measurement of a relative movement of the metal plate of approximately 5 mm deviation and with a rotation speed of 20 min^{-1} or 0.33 Hz as an example of a movement determination in the millimeter range. The deviation is clearly resolved.

In a next measurement, the breathing of a test person is monitored. The same measurement setup and the background-removal procedure are applied for this measurement. The antennas are placed to target the region of the abdomen, where the strongest breathing movement takes place. Fig. 3.16 (a) shows the time domain measurement and Fig. 3.16 (b) gives the computed spectrum of the measured breath rate curve. The time-domain measurement is presented with the movement axis upside down. This is the natural representation for physicians, because breathing-in is in the positive direction from the patient's view but means a reduced distance towards

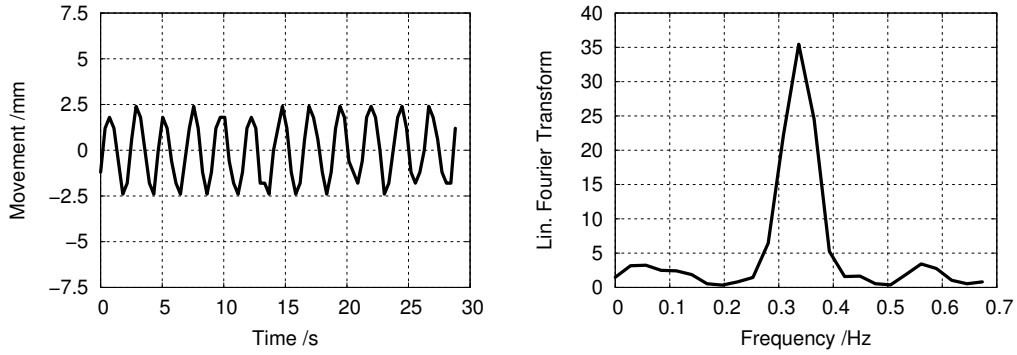

(a) (b)

Figure 3.15: Measured movement of the metal sledge with a relative deviation of approx. 5 mm in (a) time and (b) spectral domain.

the radar sensor. The drift of the breathing curve can be explained by a small movement of the whole body of the test person.

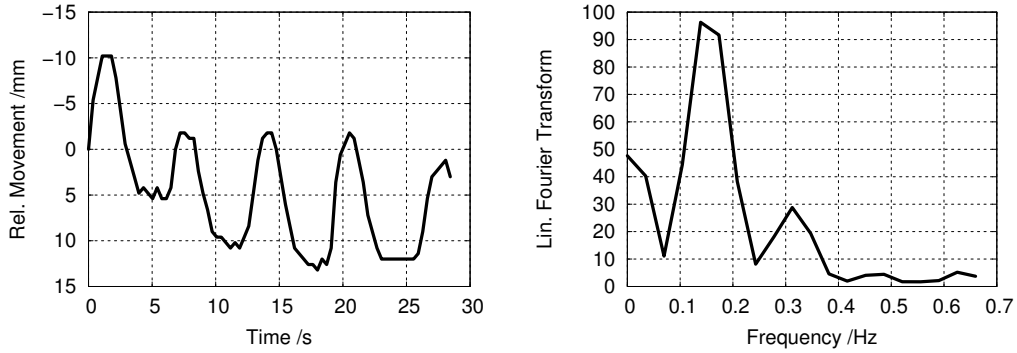

(a) (b)

Figure 3.16: Breath-rate measurement using the undersampling receiver in (a) time and (b) spectral domain.

Although the breath rate of a test person can be obtained with high accuracy, the concept is investigated using a commercial measurement device, which is not flexible in settings, such as number of data points or update rate of the GPIB interface. In the next section, an IR-UWB radar system using the hardware correlation receiver is presented. This allows a flexible setting of all system parameters and employs a hardware, tailored for UWB operation.

3.5 Radar Using a Hardware Correlator

In this section a hardware correlation reception is investigated applying the components presented in Sec. 3.2 together with control and acquisition components. First, the hard- and software implementation of the hardware correlation demonstrator is presented, then two methods of movement determination are explained using the demonstrator.

3.5.1 Hard- and Software Implementation

A demonstrator for the hardware correlation radar is built in accordance with the block diagram in Fig. 3.17. Used are the Vivaldi transmit antenna with the impulse generator, as discussed in Sec. 3.3, and the correlator antenna with the correlator IC and the baseband circuit, as discussed in Sec. 3.2.2.

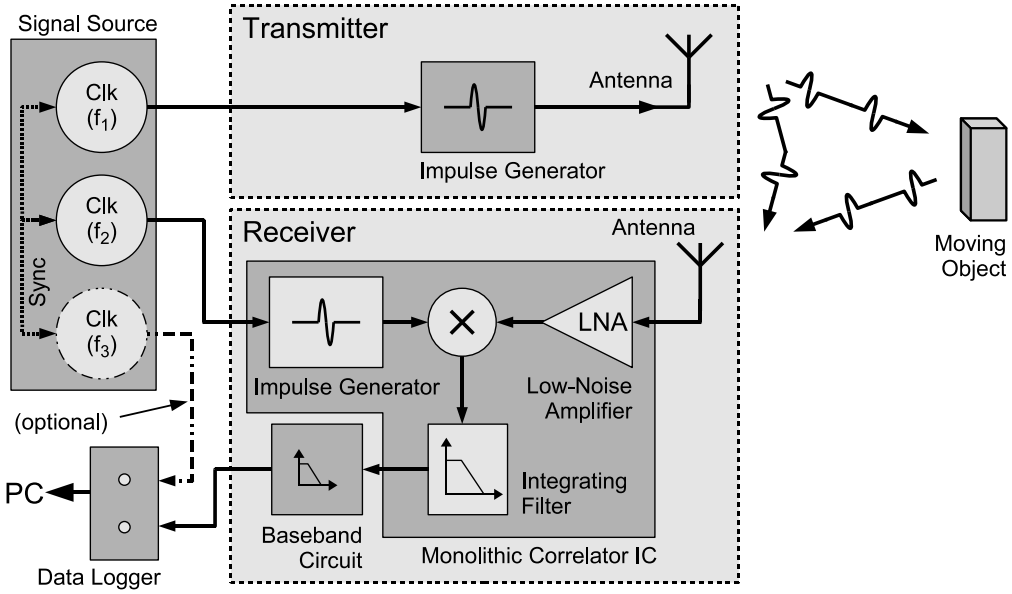

Figure 3.17: Block diagram of the correlation-based radar demonstrator.

The impulse generators in transmitter and receiver are fed by sinusoidal trigger signals created by the direct-digital-synthesizer (DDS) signal source AD9959 [63], which is available as an evaluation-board [64]. The board has four channels which can be controlled individually in frequency and phase and are sharing a common synchronization reference. Two channels supply the transmit and receive boards,

an optional third is used for synchronization, which will become relevant for the sweeping-impulse correlation method, shown in Sec. 3.5.3. The output frequency of the AD9959 ranges from 0 to ≈ 210 MHz with a minimum step size of ≈ 0.116 Hz; the minimal adjustable phase step is ≈ 0.019°. The non-decimal fractions of the values are due to the binary operation of the device.

The sinusoidal purity of the trigger signals is a major concern. This is due to the direct influence of threshold-switching operation on the jitter of the transmit and the template impulses. Impulses with strong jitter need to be avoided, because jitter changes the time-alignment of the correlation operation and therefore introduces amplitude fluctuations which distort the measurement. It is therefore required that the jitter of the trigger signals for the impulse generators is very small (compare with the measurements of the additional jitter of the impulse generators in Sec. 3.2.1). For the DDS, especially non-harmonic spurs in the output sinusoidal are identified as a major contribution to jitter of the trigger signal. Fig. 3.18 (a) shows the spectral measurement of one output channel of the DDS. The spurious-free dynamic range (SFDR), as the amplitude distance of the wanted signal component to the next interfering signal component [65], is smaller than 50 dBc. The jitter variation Δt_{ji} of a sinusoidal signal due to an overlaying non-harmonic spur signal can be calculated by using $\sin(x) \approx x$ for small values of x, to

$$\Delta t_{ji} = 2 \cdot \frac{\Delta A_{SFDR}}{2\pi \cdot f_{rep}} \ , \tag{3.5}$$

where f_{rep} is the frequency of the sinusoidal signal and ΔA_{SFDR} is the amplitude difference to the spur, here obtained by $\Delta A_{SFDR} = 10^{-SFDR/20}$. Calculating this for a SFDR of 50 dBc and f_{rep} = 200 MHz, we obtain Δt_{ji} = 5 ps, which is too much for a precise ranging, as indicated in the correlation evaluation in Sec. 2.3.2.

To obtain a pure output sinusoidal, the control signals are bandpass filtered. To also sufficiently suppress spurs very near to the wanted sinusoidal, a filter with a high quality factor, i.e. a small passband width, is necessary. Therefore, helical bandpass filters are built, as described in [66, 67], which have a good quality factor in the desired frequency range. Fig. 3.19 (a) gives a picture of the opened helix bandpass filter and Fig. 3.19 (b) shows the S-parameter performance measured in a 50 Ohm environment. The filter has an insertion loss of 0.9 dB at 200 MHz center frequency and a 3 dB-bandwidth of 6 MHz. Using the bandpass filter, the SFDR of the DDS board output signal has strongly improved, as Fig. 3.18 (b) illustrates. The SFDR is larger than 70 dBc and therefore the jitter variation Δt_{ji} is smaller than 0.5 ps. Unfortunately, the use of the bandpass filter brings a loss of flexibility in the chosen

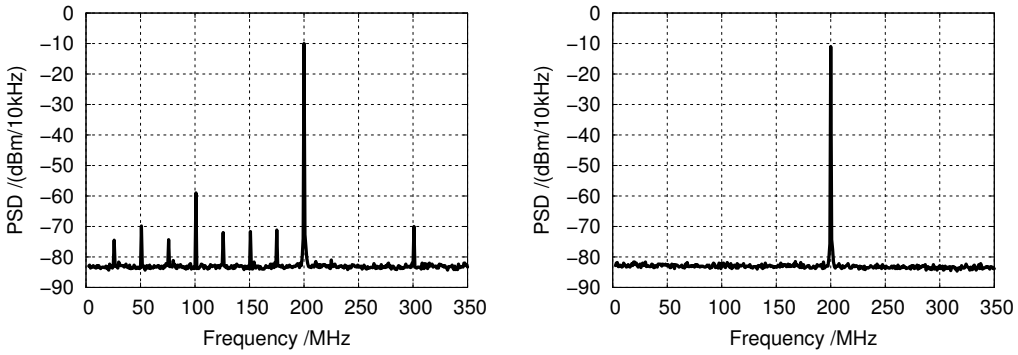

(a) (b)

Figure 3.18: DDS AD9959 output spectrum (a) without filtering and (b) with helical bandpass filter.

repetition rate, which is now fixed within the filter bandwidth. However, the use of the DDS IC is still justified because the used two (or optional three) channels remain coupled, which is important for a precise phase adjustment or an adjustment of a small frequency difference between the signals.

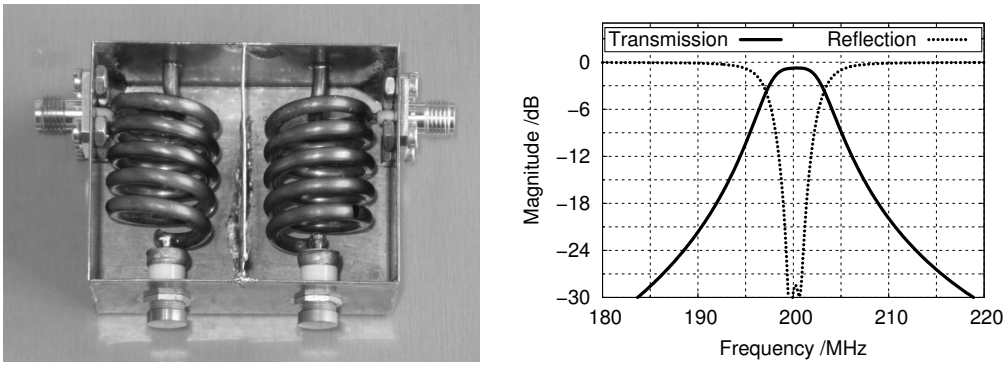

(a) (b)

Figure 3.19: Helix bandpass filter; (a) picture of the opened housing and (b) measured S-parameter performance.

For data acquisition, a USB oscilloscope [68] in data-logger mode is applied, which transfers the sampled data with a 30 µs sampling time to a personal computer. For setting the DDS board frequencies and post-processing of the acquired measurement data, a custom computer program is written using LabWindows/CVI from

National Instruments [69], a C-based programming software with pre-build mathematical and graphical functions.

3.5.2 Correlation-Slope Detection

The first presented method for a movement detection with the hardware correlation demonstrator is to exploit the slope of the correlation function. The input impulse from the object's reflection together with the correctly aligned template impulse result in the largest correlator output amplitude. If, due to the movement of the investigated object, the input impulse from the object's reflection is moving, then an amplitude fluctuation is caused in the correlator output signal, which can be processed and from which the movement of the object can be determined subsequently. This amplitude variation follows the slope of the correlation curve and takes place only in the region of the correlation impulse. Therefore, a pre-adjustment of the template and the receive impulse to a working region of the correlation function must be done. Fig. 3.20 (a) shows a normalized autocorrelation function of a fifth Gaussian derivative ACF_5, with the working region of this approach plotted in the bold and crossed line above. The large cross in Fig. 3.20 (a) indicates the location

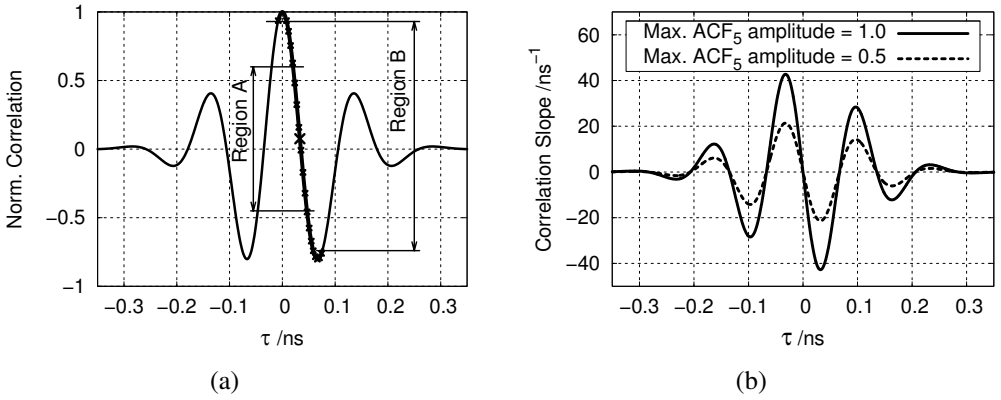

Figure 3.20: (a) Normalized correlation function ACF_5 and the working regions for a movement determination using the correlation-slope detection. The large cross indicates the location of the maximum slope and therefore the highest sensitivity. (b) Slope of the correlation function with two different amplitudes, predicting high sensitivity, but also indicating the problem in determining the object deviation under varying receiver amplitudes.

of the maximum slope. The measurement works best around the maximum slope in the approximately linear region A.

The sensitivity of this method depends on the slope of the correlation function and consequently, on the applied impulse shapes. Using the fifth Gaussian derivative impulses, the correlation slope is calculated by differentiating the correlation function, as seen in Fig. 3.20 (b). In the solid curve, the corresponding fifth Gaussian derivative impulses both have an amplitude leading to an autocorrelation function ACF_5 with an amplitude maximum of one. Also seen in the figure, this leads to a maximum slope of 42.7 ns^{-1}, predicting high sensitivity when the impulses are pre-adjusted to the maximum slope at $\tau = \pm 32$ ps. The dashed line in Fig. 3.20 (b) presents a further case where the received fifth Gaussian derivative has only half of the amplitude than before, leading to a maximal amplitude of the autocorrelation function ACF_5 of 0.5. This occurs in the radar system when reflected signals of different amplitude are received, stemming from changed object distances or from objects with different radar cross-sections. Also seen in Fig. 3.20 (b), the correlation slope decreases to half of the previous value. This means that the sensitivity of the radar system changes with the received amplitude. As a consequence, the deviation amplitude of the object under scrutiny can not be precisely computed using the slope-detection method, because on the one hand, a smaller deviation of the object causes a smaller correlator amplitude, and on the other hand, a smaller impulse amplitude at the receiver input decreases the correlation amplitude, too. However, the general movement cycle and the frequency of the movement can be determined by this method.

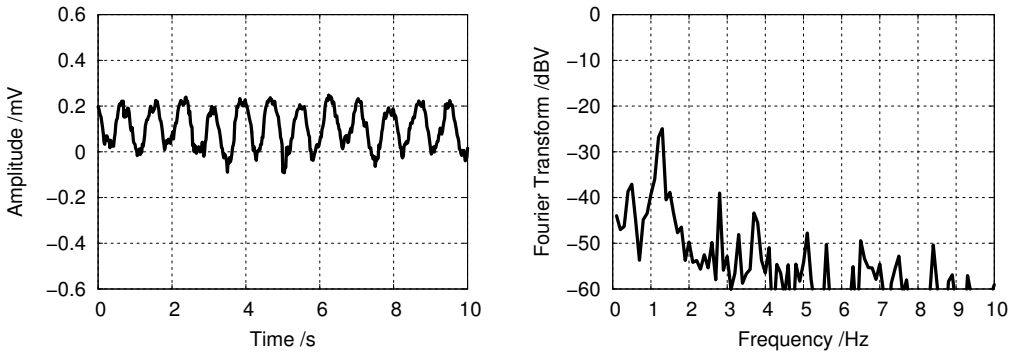

Figure 3.21: Moving metal plate with a 2 mm deviation at a distance of 60 cm in (a) time and (b) spectral domain.

To process the measurement using the correlation slope, the location of the reflected impulse and the template impulse needs to be adjusted precisely to the object under scrutiny in order to hit the correlation function in the position of the maximum slope. This can be done by a continuously varying phase shift of one of the trigger signals. When the targeted region is reached, a moving object causes a varying voltage signal at the correlator output. An example measurement of this is shown in Fig. 3.21 for a 2 mm deviation amplitude at a mean distance of the metal plate of 60 cm. The motion can be clearly resolved both in time and in spectral domain.

When the deviation of the object gets too large, the correlation function is brought to its limits, as can be seen in the correlation plot of Fig. 3.20 (a) indicated by region B. Here, the slope can no longer be considered linear and a distortion of the correlator amplitude takes place. Fig. 3.22 presents a measurement example in which the deviation of the metal plate is now adjusted to 15 mm at a mean distance of 60 cm. It is shown that the sinusoidal shape is clipped in time domain, which generates distortion harmonics in the spectrum.

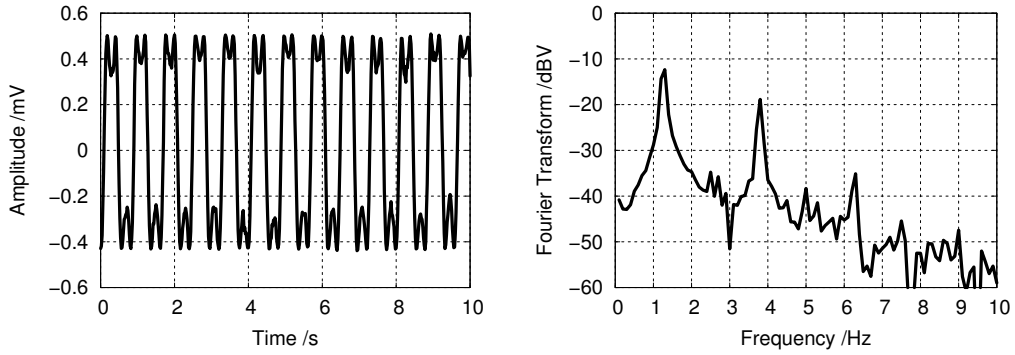

(a) (b)

Figure 3.22: Moving metal plate with a deviation of 15 mm at a distance of 60 cm in (a) time and (b) spectral domain. The amplitude is distorted because the boundaries of the correlation function are reached.

As could be proven by the measurements presented, the movement determination using the correlation-slope procedure has the precision to resolve movements in the mm-range, but the method has advantages and disadvantages. A definite advantage of the procedure is its simple system concept, since the correlator output voltage can be used directly to display the movement and no post-processing of the acquired data is necessary. For the desired task of measuring the breath-rate, no high sampling rates are necessary for the data logger; even for faster moving signals

the sampling rates are moderate. However, a disadvantage of the correlation-slope detection is that the system needs a pre-adjustment of the impulses to the desired object, which requires additional computation effort. Furthermore, using this method, only a relative movement measurement of an object can be performed. Another major disadvantage is that large deviation amplitudes or a constantly moving object beyond the correlator working region cannot be resolved or require a readjustment of the working point during the measurement, leading to an increased complexity of the procedure. Besides, only the deviation frequency of the object can be determined precisely by this method; the deviation amplitude cannot be computed because the correlator output amplitude varies with the distance of the object to the sensor or the radar cross-section of the object. Furthermore, a radar system using the correlation-slope method can only point to one object, a multi-object tracking is not possible. For a pure movement determination of one object, the correlation-slope detection is applicable. In the next section, another method is presented which allows an absolute position determination and has a working region not limited to the linear region of the cross-correlation function.

3.5.3 Sweeping-Impulse Correlation

Another method for movement detection can be found in the principle of sweeping-impulse correlation. This method uses a small offset frequency Δf between the repetition frequency f_{rep} of the impulse train in transmitter and receiver (which is equivalent to a continuously incrementing phase) to scan the channel in front of the antenna [70, 71]. The operation applies an undersampling principle as discussed in Sec. 3.4, but here a Gaussian impulse is used as the sampling signal in contrast to a narrow impulse in the sampling oscilloscope. Fig. 3.23 (a) illustrates the movement of the template signal with respect to the time location of the antenna receive signal.

The antenna receive signal in this illustration consists of one impulse originating from the direct coupling between the antennas and another impulse from a reflection. For illustration purposes, the Δf-signal in Fig. 3.23 (a) is shown with a very large frequency difference. It can be seen that the template impulse is continuously sweeping through the receiving signals. While the impulses are sweeping, the correlation function of the complete channel is computed by the correlation receiver. This channel sweep is continuously repeated. Fig. 3.23 (b) presents the signals in the vicinity of the impulse. It can be seen that the correlation function evolves with increasing time shift τ. In the computed correlation, the peak from the object under scrutiny can be identified. For a moving object, the correlation peak of the object

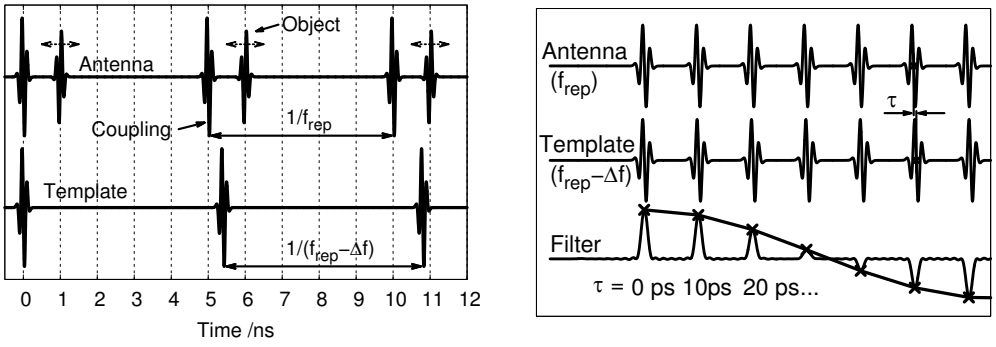

(a) (b)

Figure 3.23: (a) The antenna receive signal and the template signal, sweeping through the receiver channel (Δf not to scale). (b) Receive and sweeping template signal in the vicinity of the impulses, forming the correlation function.

will change depending on the object's position. By comparing one correlation position with another, the movement can be computed. The correlation signal of the time-domain example presented above is computed in Fig. 3.24.

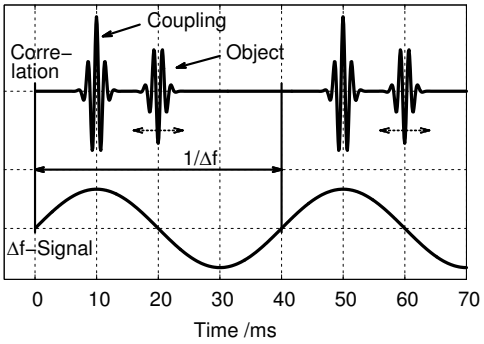

Figure 3.24: The correlator output signal together with a generated Δf-signal to separate the continuous correlation sweep.

The repetition of the correlation sweep takes place with a rate of Δf, as shown in the lower part of Fig. 3.24. The continuous correlation sweeps must be divided into parts belonging to one channel representation. Therefore a sinusoidal signal with frequency Δf is generated by the third channel of the DDS board and brought to

the second input of the data logger (cf. block diagram in Fig. 3.17). The separation of the correlation sweeps is done at every rising slope of the Δf-signal.

The chosen settings have an impact on the system performance. For the demonstrator built, a repetition frequency $f_{rep} = 200\,\text{MHz}$ and $\Delta f = 25\,\text{Hz}$ is applied. The correlator output signal and the Δf-signal are continuously sampled by the data logger with sampling time $T_s = 30\,\mu\text{s}$. Using these values, the system performance can be calculated. The maximum sensing distance d_{max} for which the distance of a reflected impulse can be indisputably associated, which means without extending into the region of the following repetition cycle, can be calculated by

$$d_{max} = \frac{c_0}{2 \cdot f_{rep}} \,, \tag{3.6}$$

where f_{rep} is the repetition rate of the impulses, c_0 is the speed of light and the $1/2$ is due to the impulses traveling the distance twice. Using $f_{rep} = 200\,\text{MHz}$, one obtains $d_{max} = 0.75\,\text{m}$. With the presented settings, the highest observation frequency f_{max} can be calculated by

$$f_{max} = \frac{\Delta f}{2} \,, \tag{3.7}$$

where Δf is the frequency difference used between the transmitted and the template impulse. With the values selected, a maximum sinusoidal movement speed of $f_{max} = 12.5\,\text{Hz}$ can be resolved, which is well suited in the present case of the slowly moving breath-rate signal. The correlation signal is sampled at quantized time steps by a data logger. Therefore the point-to-point time resolution is also quantized by the difference between two sampling instances. A minimal point-to-point resolution $d_{min,pp}$ can be calculated by

$$d_{min,pp} = \frac{c_0}{2 \cdot f_{rep}} \cdot T_s \cdot \Delta f \,, \tag{3.8}$$

where T_s is the sampling time of the data logger. This leads to a minimum point-to-point resolution $d_{min,pp} = 0.5625\,\text{mm}$ when applying the above-mentioned values.

The data points acquired from the data logger are transfered in data blocks of 60,000 values, equivalent to a data block of 1.8 s or 45 correlation sweeps. Each data block is appended to the previous data block, achieving a continuous measurement. As mentioned before, for a separation of the correlation sweeps the Δf-signal is sampled and also transfered to the computer for post-processing. Special care needs to be taken for the Δf-signal because noise is overlaying the Δf-signal and is introducing an error to the zero-crossing used for dividing the correlation signal.

Fig. 3.25 gives an enlarged part of the measured Δf-signal. The noisy spikes would influence the precision of the correlation separation and decrease the measurement accuracy. As a countermeasure, the acquired sinusoidal is first smoothed with a moving average algorithm to damp unwanted spikes. Next, the number of positive slopes in the 60,000 points data block is counted. With this number, an artificial sinusoidal is calculated, which fits the original frequency but which has an ideal smooth slope. With this sinusoidal, the separation of the correlation blocks is performed, which leads to an error of one sampling digit only. In Fig. 3.25 the three states of the correlation repetition Δf-signal can be compared in an enlarged graph.

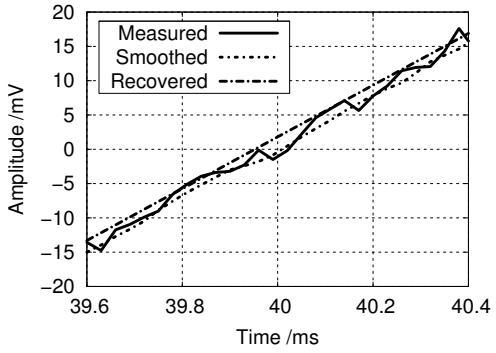

Figure 3.25: Comparison of sampled and post-processed Δf-signal. The straightened slope of the recovered signal can be used best for the correlation separation.

Fig. 3.26 shows a measurement of one separated correlation sweep with signals of the direct antenna coupling and one reflection at the metal plate. The position of the metal plate d_{ob} can be calculated from the reflection signal by

$$d_{ob} = \frac{c_0}{2 \cdot f_{rep}} \cdot T_{ob} \cdot \Delta f \ , \tag{3.9}$$

where T_{ob} is the time instance corresponding to the object location. For a continuous position determination, the time instance T_{ob} for each correlation sweep is computed from the acquired measurement data. When the object is moving, T_{ob} varies according to the movement and the object can be tracked throughout the correlation sweep. In the following, three methods are compared in order to accurately calculate the time instance T_{ob} in the continuously sweeping correlation signal. The comparison is carried out with the presented metal plate placed in front of the demonstrator, but not moving this time. The measured correlation signals are plotted in a histogram

and on the basis of the distribution of the histogram, the method with the smallest distribution error can be identified. All three tested methods are illustrated in the correlation plot of Fig. 3.26.

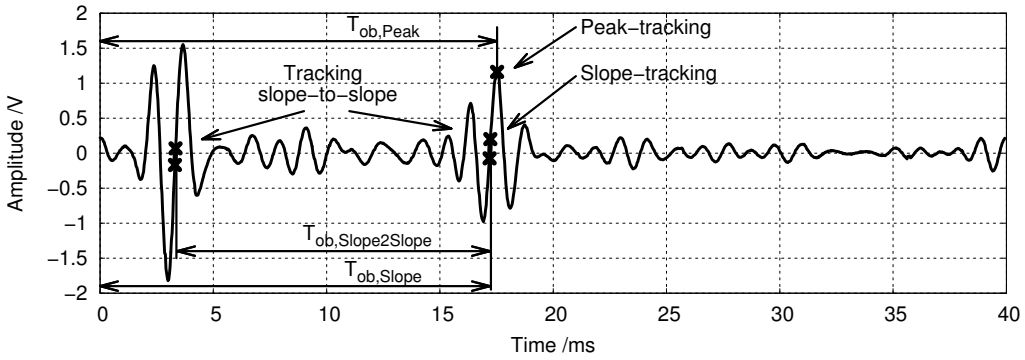

Figure 3.26: Measured correlation sweep with the three methods tested for object tracking.

The first method tested is the peak-tracking method. As illustrated in Fig. 3.26, the peak-tracking method applies a simple tracking of the maximum peak of the object reflection signal to obtain $T_{ob,Peak}$. A histogram of this method is depicted in Fig. 3.27 (a). It shows that the distribution is quantized with a step of the calculated 0.5625 mm according to (3.8), resulting from the chosen system settings. The distribution width of the histogram is approx. 1 mm (FWHM). The second method, called slope-tracking method, applies a tracking of the correlation-signal slope, as can again be seen in Fig. 3.26. Here, the positive and negative sampling points around the zero-crossing next to the maximum of the reflection signal are used to span a straight line. The calculated position where the straight line crosses the zero axis is taken as time instance $T_{ob,Slope}$. Fig. 3.27 (b) shows the distribution of the slope-tracking method, which is continuous because the zero-crossing of the slope is independent from the sampling instances. However, the distribution width remains approximately 1 mm, which is the same as obtained by the peak-tracking method.

The third method tracks the slope of the reflection signal, as in method two, but additionally takes the static impulse from the antennas' direct coupling into account. The subtraction of the zero-crossing of the direct coupling and the zero-crossing of the reflected signal is used as time instance $T_{ob,Slope2Slope}$, as can be investigated in Fig. 3.26. The error from the subtraction of the static time instance can be compensated by adding a constant calibration value. The histogram of this method in

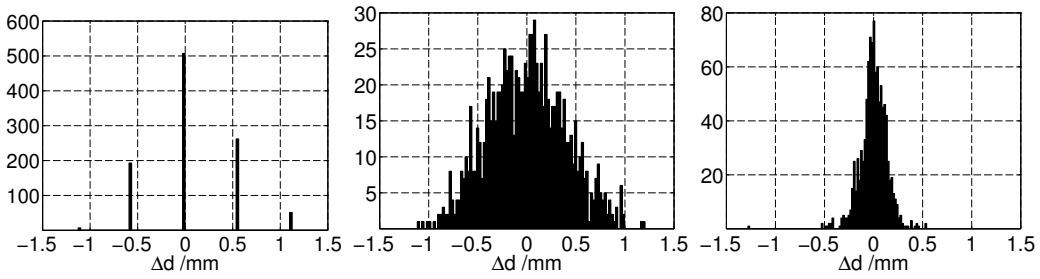

(a) (b) (c)

Figure 3.27: Distribution comparison between the three methods for tracking the correlation signal: (a) tracking the maximum peak, (b) tracking the slope and (c) tracking slope-to-slope.

Fig. 3.27 (c) shows that the distribution is continuous and that the distribution width has reduced to below 0.5 mm (FWHM). This is because the slope-to-slope tracking method removes the one digit error originating from the sampled correlation repetition Δf-signal. Therefore the third position tracking method performs best and is applied for the following measurements.

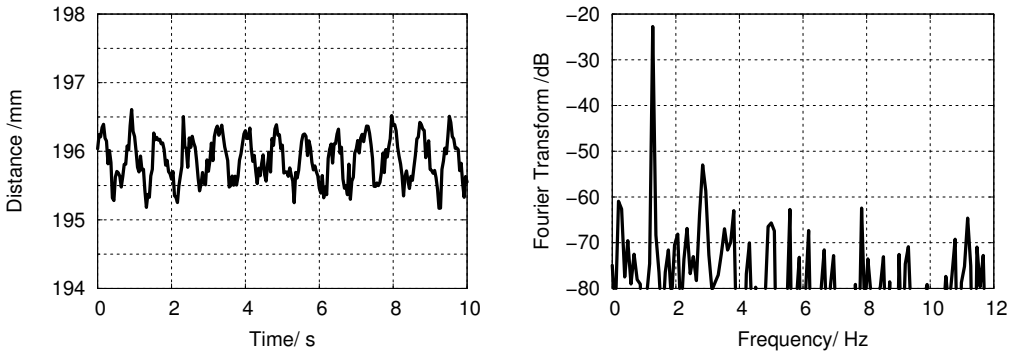

(a) (b)

Figure 3.28: Moving metal plate with a deviation of approx. 1 mm at a mean distance of 19.6 cm in (a) time and (b) spectral domain.

In order to verify the precision predicted, the metal plate from before is placed in front of the sensor and is now moving with a deviation of approx. 1 mm. The measurement results in both time and spectral domain are shown in Fig. 3.28. The figures illustrate that the metal plate is placed at a distance of 19.6 cm with a deviation

of approx. 1 mm and a rotating speed of 1.3 Hz. The deviation can be clearly resolved, which confirms the evaluation. With this setup the breathing measurements can be done. For this measurement, male test persons lying on the back are placed in front of the operating sensor. Two measurements of the acquired time-domain breathing patterns can be seen in Fig. 3.29. Fig. 3.29 (a) illustrates a test person's normal, deep breathing and Fig. 3.29 (b) shows the artificially fast and flat breathing of another test person. As discussed in the breathing measurement of the radar using undersampling reception in Sec. 3.4, the movement axis is inverted here as well, plotting the breathing signal from a medical perspective.

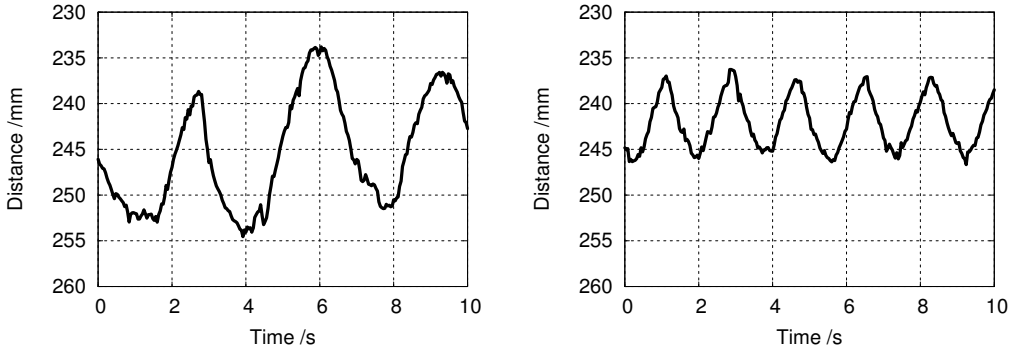

Figure 3.29: Examples of a breathing of two male test persons in time domain with (a) a normal, deep breathing cycles and (b) an artificially fast and flat breathing.

A measurement is carried out, in which the breathing patterns of a seven-week-old infant are determined[2]. These measurements are done while the infant is sleeping. Fig. 3.30 (a) shows the resulting breathing pattern for the infant sleeping in a bed on its back and Fig. 3.30 (b) for the infant sleeping in a typical car seat. The second measurement shows the arrhythmic breathing pattern, which is very typical for infants. These measurements suggests that using this radar principle a sleeping infant in the backside of a car can be detected.

The sweeping-impulse correlation method has benefits and drawbacks, too. This method requires much more post-processing compared to the slope-detection method, because the correlation signal needs to be sampled at comparably higher rate and computation effort is necessary to calculate the movement. A further disadvan-

[2]All measurements on humans are approved by the ethic commission of Ulm University.

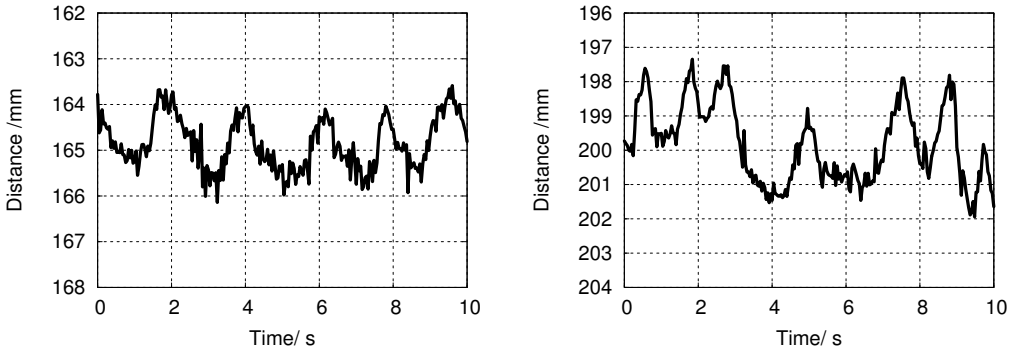

Figure 3.30: Time domain breathing cycle of a seven-week-old sleeping child, sleeping (a) in a bed, showing a continuous breathing cycle, and (b) in a car seat, showing a breathing cycle with an arrhythmic breathing.

tage of this method is that it requires an additional Δf-signal to be generated and sampled for the precise separation of the correlation sweeps, thus increasing hardware complexity. On the other hand, the method has benefits as well. The sweeping-impulse correlation method scans the whole channel, allowing to measure the absolute distance of objects in front of the sensor. Furthermore, large deviations of the object movement can be resolved; even multi-object tracking could be implemented by following the same principle. An amplitude scaling of the received impulses due to a reduced radar cross-section has no effect on the precise determination of the object movement amplitude. However, when the radar cross-section gets too small, enhanced signal processing methods are required to determine the smaller signals in the channel. Another advantage of the method is that no control of the repetition-rate signals is necessary during sensor operation. Besides, no pre-adjustment of the template impulse to the object must be done, which decreases complexity of the control unit. As the presented measurements demonstrate, the method using sweeping-impulse correlation is very well suited for an implementation as a movement detection and consequently as a breath-rate sensor.

4 Analog Transmission Using Frequency Modulation of Impulses

One motivation of this study is to distribute analog information between very simple network nodes located in the vicinity of each other. Because the complexity of the transceiver devices would increase by an analog-to-digital conversion, a UWB transmission scheme is to be used which processes the analog information directly. The analog transmission scheme should transmit information signals of any kind, such as e.g. speech, music or analog sensor data. For the transmission, it is favorable to use IR-UWB technology to maintain the advantage of UWB in terms of low interference to sensitive electronic equipment in a clinical environment or on board of an aircraft. Furthermore, the transmission scheme should be able to operate perturbation-free in a multi-user scenario.

4.1 Introduction to the Principle

Proposed modulation schemes for IR-UWB apply a discrete and quantized modulation of the impulses, in which each impulse contains the digital information of one bit (or chip). The impulses are either pulse-amplitude modulated (PAM) or pulse-position modulated (PPM), as discussed in Sec. 2.3.3 or in more detail in [23]. In contrast to digital transmission schemes, here analog information needs to be transmitted. Therefore, an innovative analog modulation scheme using UWB impulses is proposed, which applies a continuous pulse-position modulation to the radiated

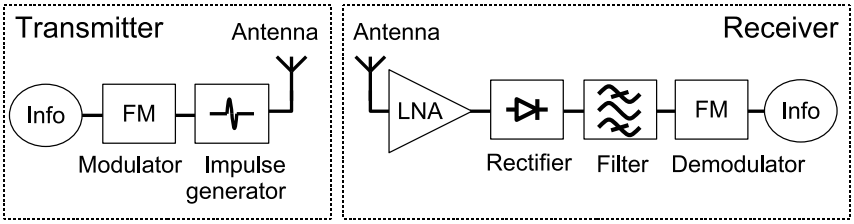

Figure 4.1: Block diagram of the analog FM IR-UWB transceiver.

impulses using a frequency-modulated (FM) trigger signal. A block diagram of the proposed analog transceiver is presented in Fig. 4.1.

At first the transmitter principle is explained. Fig. 4.2 (a) illustrates the time-domain signal evolution in the transmitter. The analog information signal is converted by a frequency modulator to a frequency-modulated sinusoidal signal. The nomenclature used in classical frequency modulation can be applied and shall be repeated briefly. A sinusoidal carrier, which is frequency modulated with a sinusoidal information signal, can be written in time domain as

$$u_{FM}(t) = U_c \cdot \cos\left(2\pi t \cdot (f_c - \Delta f_c \cdot \sin(2\pi f_s t))\right) \ . \tag{4.1}$$

Here, f_c is the frequency of the FM carrier signal, which in the FM IR-UWB system is responsible for the repetition rate of the impulses; Δf_c is the FM deviation, which is a measure of the largest deviation of the FM carrier signal or the volume of the modulation; f_s is the frequency of the sinusoidal information signal, of which the FM rate $f_{s,max}$ is the highest appearing frequency component in case of a diverse information signal. The amplitude of the carrier signal U_c is of minor importance in the present case because u_{FM} is used to trigger the impulse generator only. For more details on frequency modulation see [72].

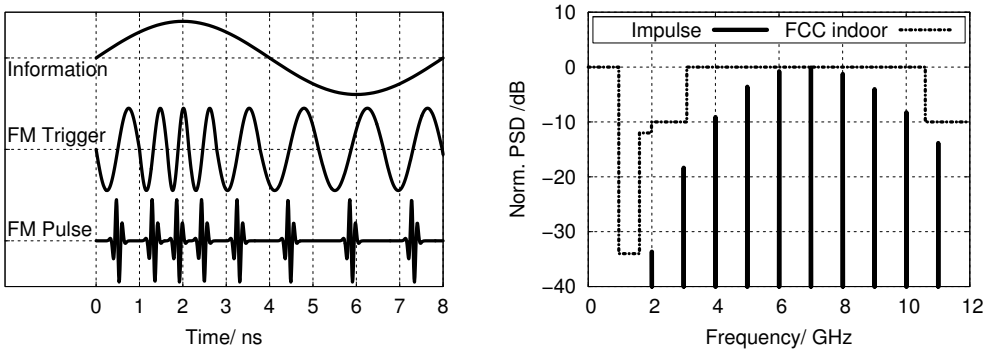

Figure 4.2: (a) Illustration of the time domain signals at the output of the transmitter's function blocks (frequency deviation not to scale). (b) Typical line spectrum of a UWB impulse train transmission.

The FM signal is used as a triggering signal to the impulse generator circuit that is placed behind the frequency modulator. At every rising edge of the signal, an impulse is generated, resulting in a position-varying impulse train, which contains

the analog information. See again Fig. 4.2 (a) for the time-domain representation. This modulated impulse train is radiated by the UWB antenna. Fig. 4.2 (b) illustrates a spectrum of the corresponding simulated UWB transmission. The envelope of the line spectrum is given by the output waveform of the impulse generator, with which the spectrum can be made compliant to any country-specific UWB mask simply by changing the impulse shape. In case of an unmodulated impulse train, the spectral lines have no spectral broadening. When a frequency modulation is applied, each line widens and its bandwidth can be approximated by a modified Carson bandwidth (cf. [72]) to

$$B_{FM,N} \approx 2 \cdot N \cdot (\Delta f_c + f_{s,max}) \ , \tag{4.2}$$

where Δf_c is the FM deviation, $f_{s,max}$ is the FM rate, in accordance to (4.1), and N represents the order number of the harmonic spectral component. For example, in case of a 100 MHz impulse transmission, the spectral line appearing at 6.6 GHz is broadened by $N = 66$ compared to the 100 MHz modulation signal.

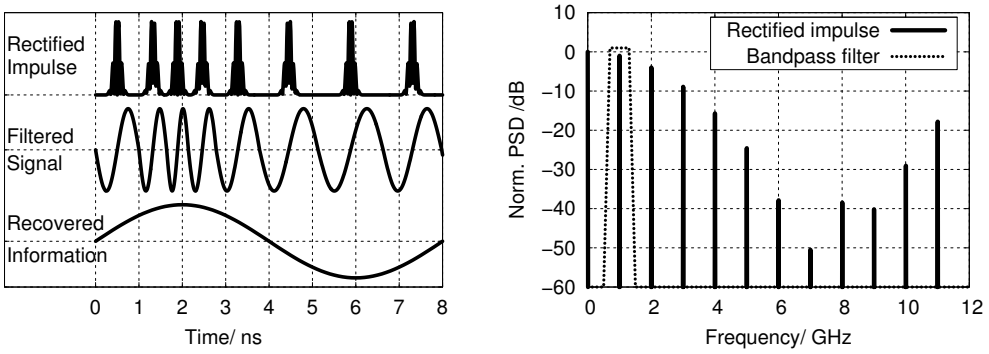

Figure 4.3: (a) Illustration of the time domain signals at the output of the receiver function blocks (frequency deviation not to scale). (b) Typical line spectrum of a rectified UWB impulse train.

As shown in the receiver side in Fig. 4.1, to demodulate the information content from the radiated impulse train, the received impulse signal is first amplified and then fed to a rectifier, which converts the bandpass limited UWB emission to lower frequencies. Fig. 4.3 (a) depicts the time-domain signal and Fig. 4.3 (b) the spectral domain of the rectified signal. As can be seen, the spectral envelope of the rectified impulses now approaches DC. The spectrum still consists of modulation-broadened spectral lines with the first harmonic line at the frequency of the repetition rate. This line is identical in frequency, FM deviation and FM rate to the FM signal appearing

at the output of the modulator used for triggering of the impulse generator. Using a bandpass filter, this spectral line is extracted and the information signal can be recovered by an FM demodulator. Fig. 4.3 (a) illustrates this operation. In the next sections, a demonstrator test system is introduced, with which the FM IR-UWB concept is investigated.

4.2 Components for the FM IR-UWB Demonstrator

This section presents the necessary components for an FM IR-UWB demonstrator system as shown in the block diagram in Fig. 4.1. The applied components are characterized for their usability in the intended task. The impulse generator, presented in Sec. 3.2.1, and the directional Vivaldi antenna, shown in Sec. 3.2.3, are used here, too. For a performance evaluation of these components see the relevant sections. In case not otherwise stated, here FM modulation and demodulation parameters from classical FM radio transmission are used, i.e. FM carrier frequency $f_c = 100\,\text{MHz}$ and FM deviation $\Delta f_c = 60\,\text{kHz}$. Applying the parameters of classical FM radio, widely available and cheap FM radio components can be applied, allowing to reduce the costs and development effort of such a system.

4.2.1 UWB Low-Noise Amplifier

As can be seen in the block diagram of the FM IR-UWB system in Fig. 4.1, a low-noise amplifier (LNA) is used in the receiver branch, following the receive antenna. A UWB LNA, fabricated in the SiGe HBT semiconductor technology from Telefunken Semiconductors is available for this task. The LNA is a three stage circuit which uses local and global resistive feedback to achieve both constant high gain and good noise performance in the full UWB bandwidth at the same time. A detailed insight to the circuit is given in [1, 73], a simplified circuit schematic of the IC is presented in Fig. 4.4 (a). The same LNA is used as the amplifier building block in the monolithic correlator IC of Sec. 3.2.2.

For a combination of components in the demonstrator system, it is necessary to use a packaged low-noise amplifier. Therefore, the packaging of the IC is explained first, the characterization measurements later compare on-chip and packaged performance. LNA packaging is more critical than impulse generator packaging. Because a parasitic inductance of a bondwire placed between chip ground and board

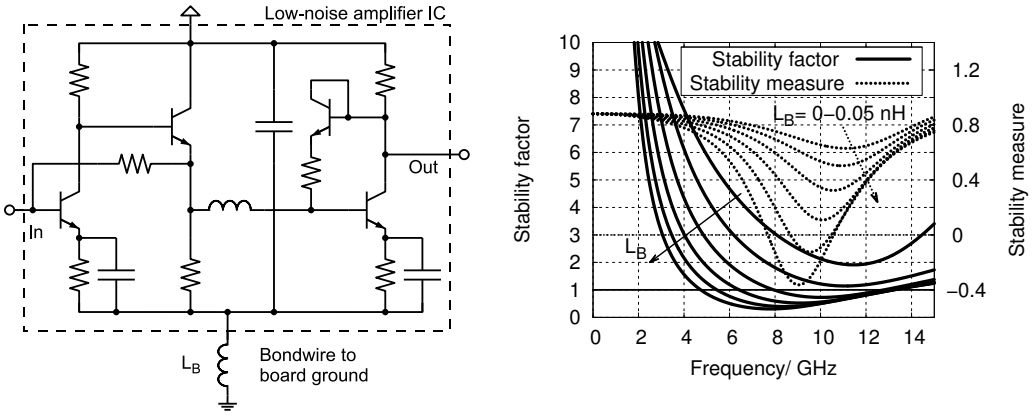

Figure 4.4: (a) Simplified circuit schematic of the LNA IC, indicating the location of a bondwire to ground. (b) Simulated stability factor and stability measure with bond wire inductance $L_B = 0$–0.5 nH.

ground introduces a parasitic feedback path and presents an inductive emitter degeneration to the transistors of the gain stages, cf. [74]. This leads to a decreased stability of the applied circuit. Similarly, an inductance between chip and board supply node, which is formed by feeding lines and bondwires and is usually larger than the ground inductance, leads to a similar effect, but because the chip supply node is tied to RF ground with a large on-chip shunt capacitor the inductance to ground has a stronger influence. An evaluation is carried out by circuit simulation using the LNA schematic of Fig. 4.4 (a) with an inductance L_B placed between the ground nodes and a DC feed placed to the supply pin. To assess stability, stability factor and stability measure are used [75]. A circuit is unconditionally stable when the stability factor is larger than one and the stability measure is positive.

As can be seen in Fig. 4.4 (b), the stability criteria are violated already with bondwire inductances $L_B > 0.01$ nH. As a rule of thumb, a bondwire of 100 µm length has an inductance of 0.1 nH [76]. For the used single-ended IC with a substrate height of 300 µm and without backside metalization of the die, at least an inductance value of 0.3 nH would have to be considered in case the chip is glued on top of the board. To keep the bondwire inductance to ground small, the IC is embedded into the RO4003 substrate to avoid long bondwires. Furthermore, a grounded coplanar transmission line is used, which has the board ground connections in the same plane as the circuit ground to additionally decrease the inductance of the path. A micrograph of the integrated IC is given in Fig. 4.5 (a). For a connection of the

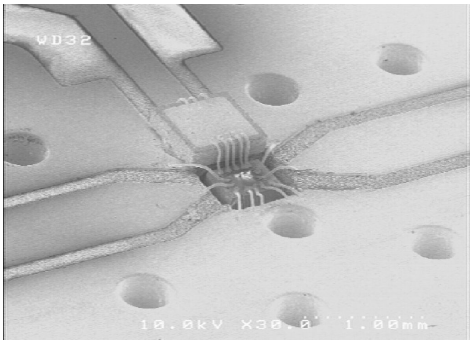

(a)

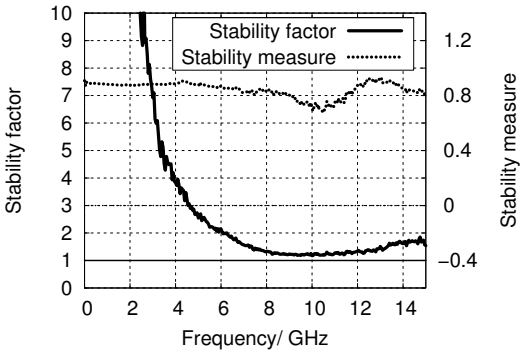

(b)

Figure 4.5: (a) Micrograph of the LNA IC embedded in the substrate. (b) Corresponding measured stability factor and stability measure of the packaged LNA.

package to the measurement equipment, SMA connectors at the in- and output are applied and a voltage regulator is used to stabilize the DC supply of the IC. The measured stability curves of the developed LNA block are shown in Fig. 4.5 (b).

The packaged LNA, including the SMA connectors and the feeding transmission lines, is characterized and compared to on-chip measurements with microwave wafer probes. Fig. 4.6 (a) shows a comparison of the gain performance. The packaged gain is around 26 dB in the complete 3.1–10.6 GHz FCC UWB band, with a gain ripple of ± 1 dB. The packaged performance deviates by less than 3.5 dB from the measured on-wafer performance. This deviation is mainly due to the bondwire inductances at the input and output ports of the IC and the ground bondwires, indicating that the effect of emitter degeneration could not be eliminated completely. A comparison of the basic group delay performance is presented in Fig. 4.6 (b). The group delay of the packaged IC is larger compared to the on-chip measurement because the package includes transmission lines. The variation of the group delay increases from 7 ps of the on-wafer performance to approximately 40 ps of the packaged one. With the measured gain ripple and group delay variation, the deformation of the impulse shape is very small.

In a further characterization of the LNA, a comparison of the noise figure can be seen in Fig. 4.7 (b). The packaged IC, including its bondwires, transmission lines and connectors, has an overall mean noise figure of 3.7 dB and stays below 4 dB in

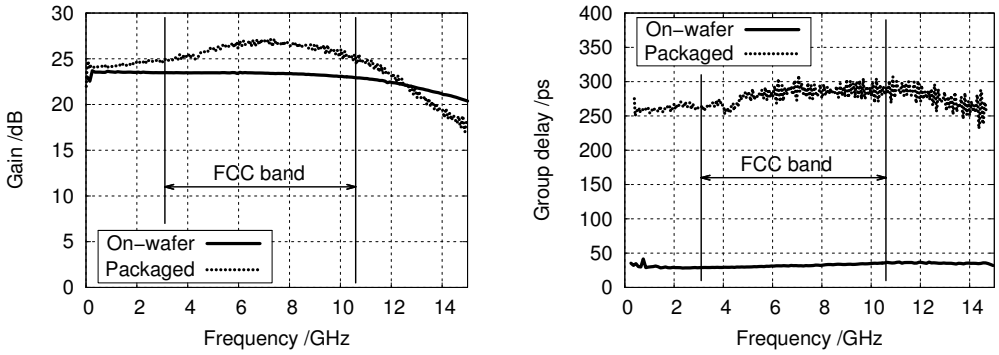

(a) (b)

Figure 4.6: Measured comparison of (a) gain and (b) group delay between the on-wafer and the packaged LNA.

the complete FCC-allocated UWB band. The noise figure increase compared to the on-wafer measurement is 0.8 dB.

To characterize the LNA's linearity a gain compression measurement is performed. Therefore, a single-tone excitation is applied to the input of the circuit with increasing power while the output power at the tone frequency is measured. The compression point is taken, where the ratio between input and output power deviates by 1 dB from its linear association [74]. For amplifiers in the receiver branch, the compression is referred to the input power. Fig. 4.7 (b) presents the 50 Ohm input-referred

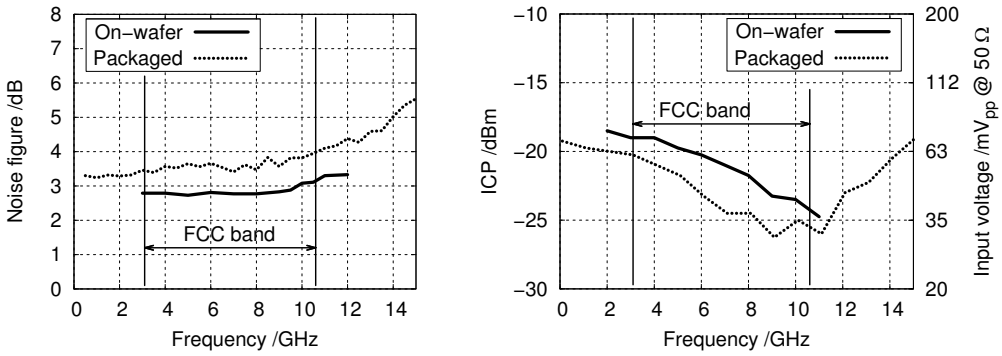

(a) (b)

Figure 4.7: Measured comparison of (a) noise figure and (b) input-referred 1 dB compression point (ICP) between the on-wafer and the packaged LNA.

1 dB compression point (ICP) of the on-wafer and the packaged LNA versus frequency. It can be concluded that the packaged LNA has an ICP larger than -26 dBm in the FCC UWB frequency band. The ICP of the packaged LNA is 3 dB worse compared to the on-wafer measured. Even though displaying the ICP in dBm is common practice, it does not constitute a practical measure in UWB system design when dealing with short time-domain impulse signals. Due to the spectral spreading of the impulse, the measured distributed spectral power appears to be low, but in time domain the spectral components all add up coherently, which results in a relatively large voltage amplitude. Therefore, the time-domain peak-to-peak voltage amplitude is a better representation of compression. Accordingly, another y-scale is displayed in Fig. 4.7 (b), which shows the peak-to-peak input voltage corresponding to the power of the sinusoidal input signal measured at 50 Ohm. Thus it can be seen that the compression of the packaged LNA starts to take place at an input voltage of 35 mV_{pp}. Based on the presented measurements, it can be concluded that the packaged LNA is suitable for the FM IR-UWB communications system.

4.2.2 Schottky Diode Rectifier

A rectifier is necessary in the FM IR-UWB receiver for converting the RF domain impulse to an impulse with spectral components extending down to DC. As rectifier components, two Schottky diodes are investigated, the commercial Schottky diode HSCH-5330 from Avago Technologies [77] and the integrated Schottky diode of the

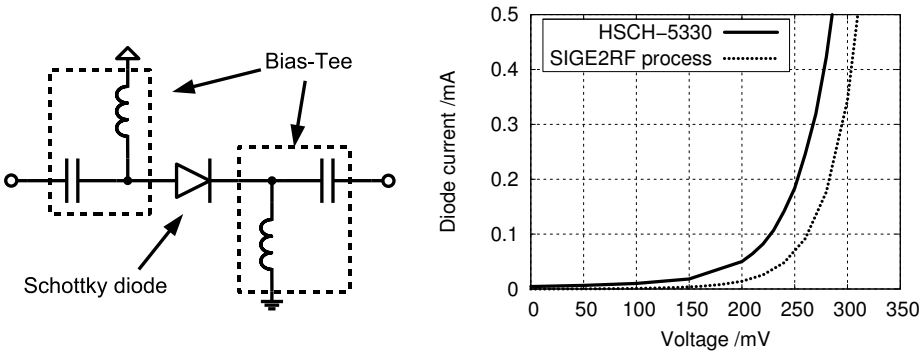

(a) (b)

Figure 4.8: (a) Simplified circuit schematic of the half-wave rectifier diode with bias-tees. (b) IV-plot of the Schottky diodes.

SiGe HBT semiconductor technology SIGE2RF from Telefunken Semiconductors [49]. Each diode is arranged in a half-wave rectifier arrangement using bias-tees, which allows an external variable bias to the diode. A simplified schematic can be seen in Fig. 4.8 (a), measured IV-plots of the diodes are shown in Fig. 4.8 (b). The diodes are slightly forward biased, which maximizes the spectral output power at the fundamental frequency. The ideal biasing current is investigated in a measurement connecting an impulse generator with a repetition rate of 100 MHz via an attenuator to the rectifier arrangement. The diode bias is varied and the power at the output bias-tee is monitored at the 100 MHz component, as presented in Fig. 4.9 (a). It shows a maximized output power at a diode biasing of 0.15 mA for the HSCH-5330 and of 0.25 mA for the SIGE2RF Schottky diode. These biasing currents are selected.

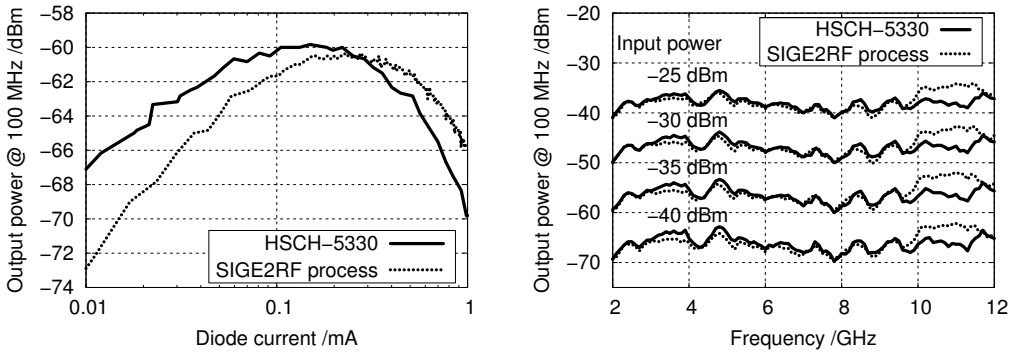

Figure 4.9: (a) Output power versus the diode biasing. (b) Measured output power of the biased diodes versus frequency of a two-tone measurement.

The relation between input and output power of the biased rectifiers for different frequencies is assessed in a two-tone measurement with a spacing of 100 MHz between the two tones. By this spacing, a signal component is down-converted to the desired 100 MHz at which its power is measured. Both tones are swept in frequency through the relevant FCC-allocated UWB band, measuring the rectification at different frequency locations. The measurement is repeated with different input power levels. Fig. 4.9 (b) gives the measured output power at 100 MHz with varying input power level versus frequency of this two-tone measurement for both Schottky diodes. It shows ripples in the output power, which are due to the unmatched operation of the diodes, but can be tolerated in the receiver because the impulse shape must not be preserved. A relation of 2 dB/dB between input and output power is

depicted in Fig. 4.9 (b) which is because of the quadratic relation of second-order intermodulation products.

The rectification operation of the biased HSCH-5330 Schottky diode can be investigated in Fig. 4.10 in time and spectral domain. The time-domain graph in Fig. 4.10 (a) shows a comparison of the impulse shape at the impulse generator output (top) and the bias-tee output (bottom). The rectification is clearly evident. The presence of negative voltages in the rectified impulse can be explained by the Schottky diode junction capacitance, which shunts some of the RF energy from the input to the output of the rectifier. The decrease in voltage amplitude by a factor of two is caused by losses in the diode and the insertion losses of both the bias-tee and the cables in the measurement setup. Fig. 4.10 (b) exhibits the spectral components at the bias-

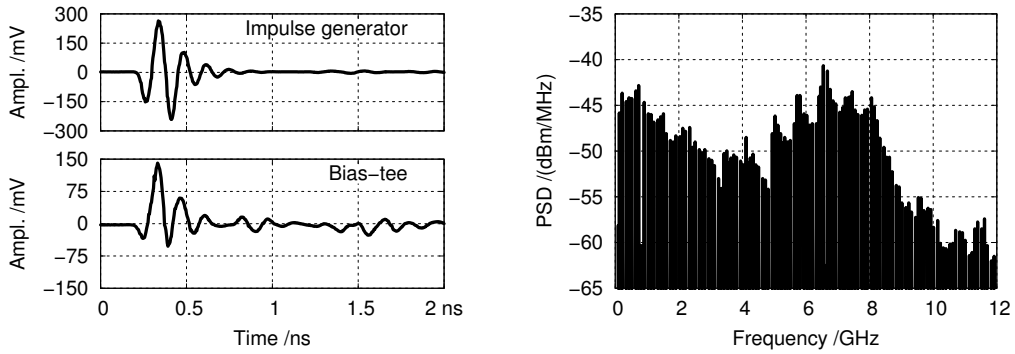

Figure 4.10: The HSCH-5330 Schottky diode in (a) time domain in a comparison between non-rectified (top) and rectified (bottom) impulse shape and (b) spectral domain of the rectified impulse.

tee output. It can be seen clearly that the spectral components are shifted to lower frequencies (the DC component is blocked by the bias circuit). The rise in spectral content at frequencies from 3–10 GHz is again due to the capacitive coupling across the rectifier diode. A detailed view of the spectrum from 0–1 GHz is presented in Sec. 4.3.1.

Because of the very similar behavior of the HSCH-5330 and the SIGE2RF Schottky diode, the further investigations are done with the biased HSCH-5330 Schottky diode rectifier only.

4.2.3 Low-Pass Filter

The required output band-pass filter is formed by the high-pass characteristics of the rectifier bias-tee and a subsequent low-pass (LP) filter of a 7th-order Chebyshev type. The LP filter is realized using SMD components on a printed circuit board.

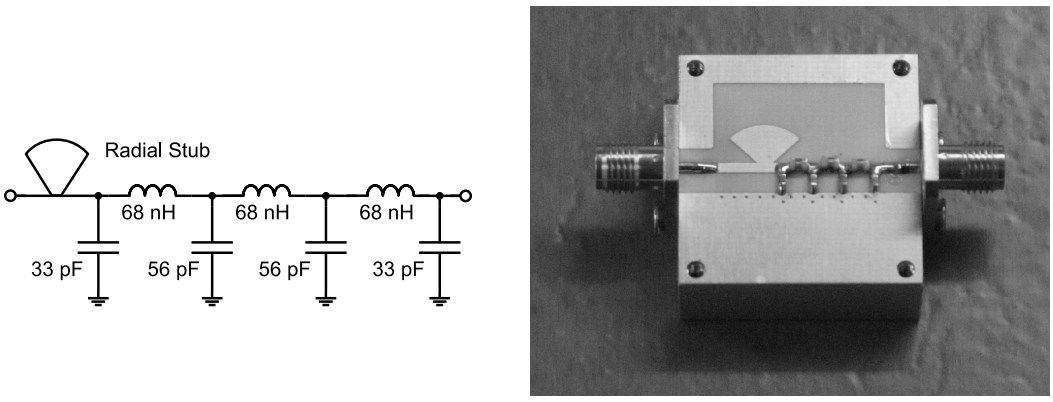

(a) (b)

Figure 4.11: Low-pass filter (a) schematic and (b) photograph.

In addition to the SMD filter core, a stub band-stop filter is included to the SMD filter to improve the filter function of the signal coupled across the rectifier diode (cf.

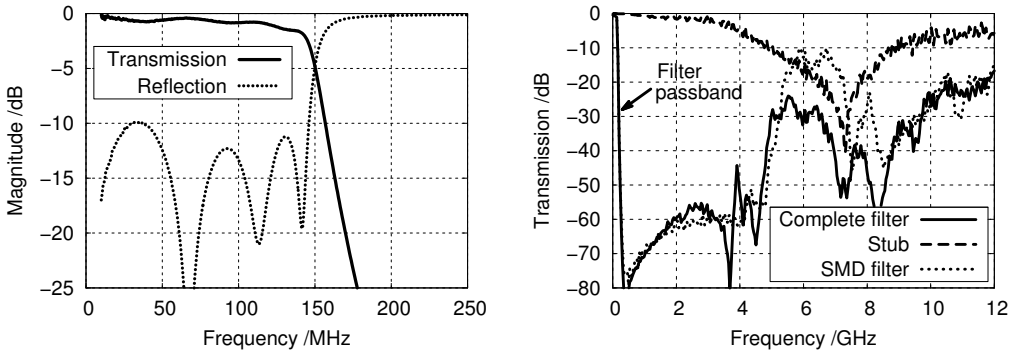

(a) (b)

Figure 4.12: Measurements of the LP filter (a) in the desired frequency range and (b) in the FCC UWB signal range up to 12 GHz, showing the suppression improvement with the radial stub at the location of the emission maximum around 7 GHz.

the spectral harmonics in the range of 3–10 GHz in Fig. 4.10 (b)). The filter section using SMD components is designed in a π-structure with a capacitance as a first component. This capacitance presents an RF short circuit to the output of the diode instead of a floating node. This maximizes the 100 MHz output signal. A schematic and a photograph of the filter can be seen in Fig. 4.11. Fig. 4.12 (a) shows the filter transmission and reflection performance in the desired down-converted frequency band. The filter has a 3 dB corner frequency of 140 MHz. Fig. 4.12 (b) presents a comparison of the transmission characteristics of the separately measured SMD low-pass filter, the separately measured stub-bandpass filter and the measurement of the combined filter structure in the frequency band up to 12 GHz. It illustrates the transfer rejection of the filter structure in the unwanted frequency band. A measurement of the time-domain output signal of the completed receiver is shown in the transceiver validation in Sec. 4.3.1.

4.2.4 UWB Omnidirectional Monopole Antennas

As mentioned before, the directive Vivaldi antennas of Sec. 3.2.3 are used in the test system. Furthermore, antennas with an omnidirectional radiation pattern are used, which are suited for transmissions in which transmit and receive antenna do not have to be aligned. For this project, the compact monopole antenna of [78, 79] is rebuilt. This antenna has a nearly omnidirectional radiation pattern in the H-plane, a maximum antenna gain of 2.4 dBi and shows a good impedance match in the FCC

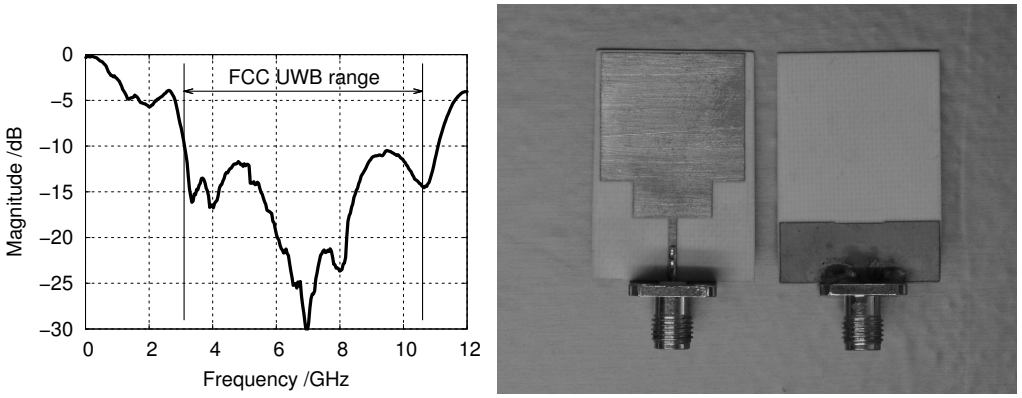

Figure 4.13: The monopole antenna; (a) measured matching characteristics and (b) photograph of the antenna's front and backside.

UWB frequency band, as shown in Fig. 4.13 (a). A picture of front and backside of the antenna is presented in Fig. 4.13 (b).

4.2.5 FM Modulator and Demodulator

For the detailed characterization of the demonstrator system, an Agilent E4438C signal generator with FM option is applied as the FM modulator and a Rohde & Schwarz ESVN 20 test receiver is used as the FM demodulator, both with manifold adjustment and measurement options. For applications as a stand-alone system, the commercially available FM test transmitter from [80] as modulator and the commercial FM radio from [81] as demodulator are evaluated as well. Both devices work in the classical FM radio broadcasting range of 87.5–108 MHz. The information signal transfer characteristic in the audio range of 20 Hz–20 kHz of the FM transmitter for different FM carrier frequencies is shown in Fig. 4.14 (a). Fig. 4.14 (b) depicts the transfer characteristic of the FM radio for different FM carrier frequencies.

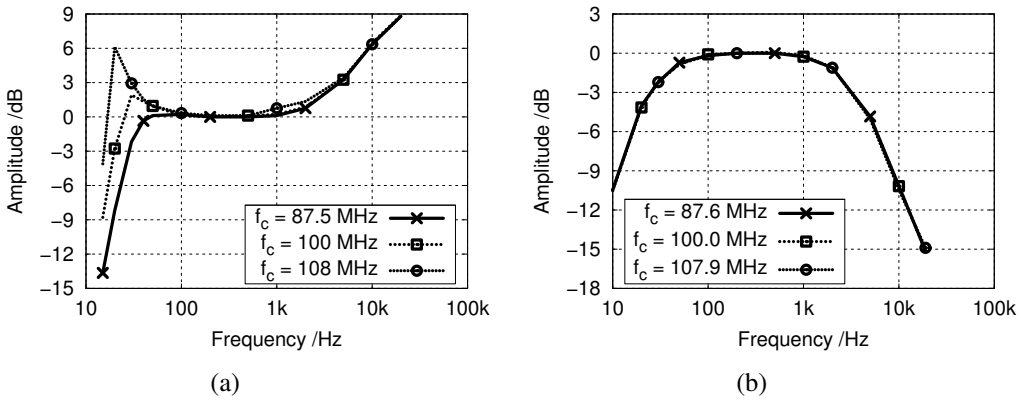

Figure 4.14: Transfer characteristic using information signals in the audio range of (a) FM modulator and (b) FM demodulator.

As the rising and falling curves at frequencies above 1 kHz in Fig. 4.14 illustrate, transmitter and receiver apply the typical FM pre-emphasis and de-emphasis concept for a better signal-to-noise ratio of the higher information signal content [72]. In both devices the 3 dB corner frequency for the low-frequency information signal is around 20 Hz. The reason for the rise of the low-frequency amplitude in the commercially available modulator is unknown, but it had no negative influence on the operation. The commercial modulator and demodulator provide the possibility of a

stereo transmission, which could be used to transmit two independent sensor signals by using the same transmitter hardware, if necessary. However, the characterization of the demonstrator was done using mono transmission only.

4.3 Measurements on the Demonstrator

In this section the FM IR-UWB system according to the block diagram in Fig. 4.1 is assembled and measurements are shown to prove the operation. If not specified otherwise, the modulated transmission is done using the FM parameters of a classical FM radio transmission, which are an FM center frequency $f_c = 100\,\text{MHz}$ and an FM deviation $\Delta f_c = 60\,\text{kHz}$. The FM rate is set to $f_{s,max} = 2\,\text{kHz}$. In the FM demodulator an appropriate filter bandwidth of the intermediate bandpass filter of $f_{IF} = 120\,\text{kHz}$ is used, fitting twice the FM deviation. Other FM parameters, which could satisfy the needs for a better transmission quality or a lower impulse repetition, are applicable as well, but with the parameters of classical FM radio, cheap commercial components can be used.

4.3.1 FM IR-UWB Transmitter and Receiver Evaluation

As discussed in Sec. 4.1, the modulated carrier signal is used as a trigger signal to the input of the impulse generator, generating a position or frequency-modulated impulse train. In the spectral domain, each spectral line is broadened by the frequency modulation according to the modified Carson bandwidth (4.2). Fig. 4.15 shows a detailed view of the measured impulse generator output spectrum around 6.6 GHz. There the comparison between an unmodulated and a modulated spectral signal clearly indicates the spectral broadening and confirms the modulation. For a determination of the signals in the receiver branch, the impulse generator was connected directly to the input of the rectifier bias-tee. The antennas and the LNA were not used for this measurement. Fig. 4.16 (a) presents the measured spectrum at the bias-tee output up to 1 GHz. It shows the rectified harmonic components with a frequency spacing of 100 MHz. Furthermore, the transmission characteristic of the low-pass filter is shown, which is used to filter the 100 MHz harmonic component. Fig. 4.16 (b) shows the time-domain signal of the recovered 100 MHz at the output of the LP filter. In center frequency and modulation content, this signal is equivalent to the output signal of the modulator used to trigger the impulse generator. Only a low-amplitude higher harmonic content of the rectified impulse can be seen in the

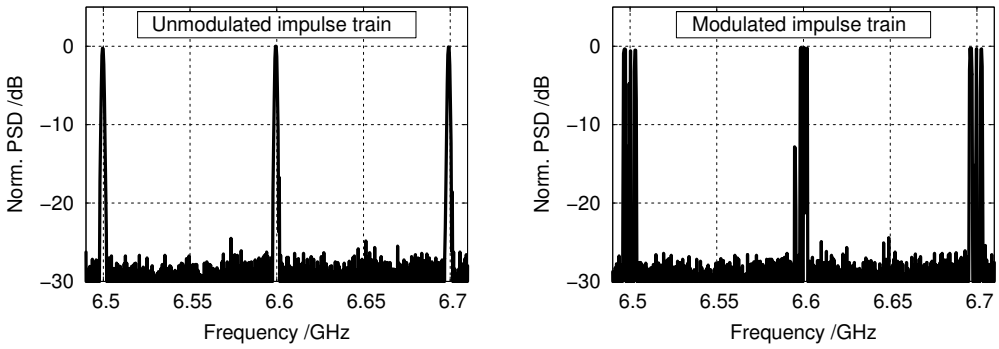

Figure 4.15: Detailed view of the spectral signal at the output of the impulse generator (a) without modulation and (b) with modulation.

negative part of the sinusoidal slope of the 100 MHz signal, which shows the good suppression of the filter. From the filtered FM signal in Fig. 4.16 (b), the information signal is successfully demodulated.

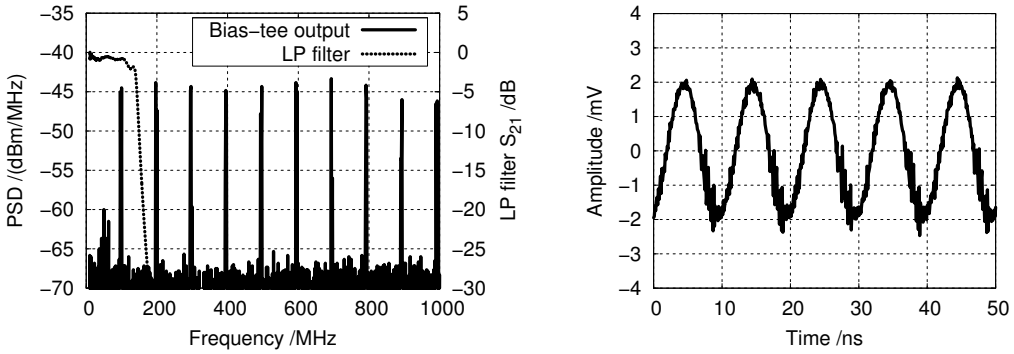

Figure 4.16: (a) Spectral components of the impulse train at the rectifier output, together with the transmission characteristic of the LP filter. (b) Recovered 100 MHz time-domain signal at the output of the LP filter.

4.3.2 Wireless Transmission

For a wireless transmission, the antennas and the LNA are used in the transceiver system. An interesting figure of merit is the maximum transmission distance, which can be spanned with the simple demonstrator system. Because the quality of the information signal constantly decreases with increasing antenna distance, a suitable criterion for the determination of this decrease must be defined first. In FM demodulators an important connection exists between the carrier-to-noise ratio (CNR) at the input of the demodulator and the signal-to-noise ratio (SNR) of the information signal at the output of the demodulator. This connection follows a linear 1 dB/dB relation for large CNR values. When the CNR gets smaller, the relation deviates from its linear behavior. The point where the curve deviates by 1 dB is called the FM threshold. For the present FM IR-UWB system, the FM threshold is specified first. This shall serve as the comparison measure for decreasing input signals at an increasing distance.

In the current setup, the FM threshold is determined by a measurement using a cable-connected step attenuator between the impulse-generator output in the transmitter and the LNA input in the receiver. The ESVN 20 test receiver is used for demodulation of the information signal, and also monitors the carrier level. For determining the FM threshold, the carrier-to-noise ratio would be necessary, but the carrier level is sufficient for this investigation because it can be assumed that the noise content in the closed demonstrator system remains constant. This means that an attenuation of 1 dB of the carrier level worsens the CNR by 1 dB as well. The demodulated information signal is brought to an 8-bit digitizing oscilloscope with a Fourier transform option. There the spectral level of the information signal is related to its noise level and the demodulated SNR value is noted.

Fig. 4.17 (a) gives a plot of the carrier level versus the demodulated SNR; the linear relation is indicated by the dotted line. The figure shows that the FM threshold deviation takes place at an SNR of 26 dB and a carrier level of 2.5 dBµV. The deviation from the linear curve at SNR values larger than 45 dB is explained by an underestimation of the noise content in the SNR, due to the limited resolution of the 8-bit oscilloscope.

To verify the wireless transmission, the antennas are then connected to the system. The maximum transmittable distance of the simple demonstrator is determined by increasing the distance r between the antennas while monitoring the carrier level at the input of the demodulator, as shown in Fig. 4.17 (b). The results closely correspond to the $1/r^2$ dependency expected for free-space propagation. The $1/r^2$ rela-

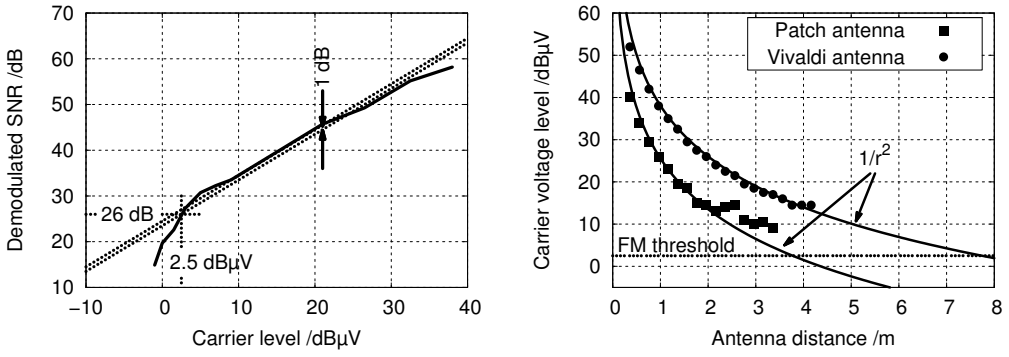

(a) (b)

Figure 4.17: (a)Demodulated SNR versus carrier level for a determination of the FM threshold. (b) Measured carrier level of a transmission with increasing distance.

tionship is used to determine the maximum communication distance before reaching the FM threshold. For the chosen system settings, the maximum distance in this demonstrator is 3.8 m using the omnidirectional patch antennas and 7.8 m using the directive Vivaldi antennas. The measured maximum distance is specific to the simple demonstrator hardware and the settings presented, proving the concept of operation. The maximum obtainable transmission distance fulfilling the spectral UWB masks can be increased, for example, by an enlarged impulse amplitude together with a lower impulse repetition rate or by using a different rectifier concept.

4.4 Measurements on Interference Robustness

In a real-world setting, many disturbances can affect the proper functionality of a transmission system. In this section, the FM IR-UWB demonstrator is investigated in its performance in a multipath environment, its robustness to narrowband interferers, and its behavior in a FM IR-UWB multi-user environment.

It is complicated to assess these scenarios by simulations because the large frequency difference between the radiated UWB impulses in the GHz-range and the modulation signal in the range of some Hz to kHz would mean extremely long simulation times. Therefore, the disturbance effects are addressed by measurements. In order to determine the linear influence of the occurring interferences only, great care is taken not to drive the active components into saturation. For these measurements,

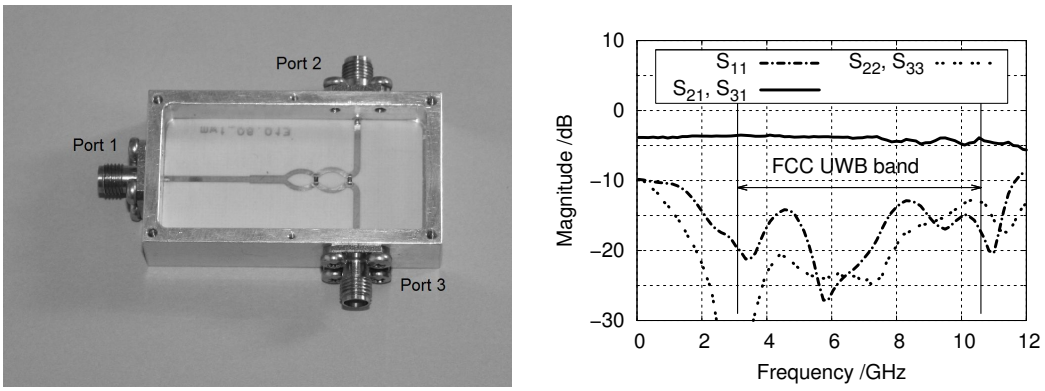

(a) (b)

Figure 4.18: Used UWB power divider/combiner; (a) picture of the opened housing and (b) measured S-parameter performance.

a UWB power divider/combiner is necessary, which is supplied through a project collaboration with the Institute of Microwave Techniques at Ulm University. The power divider/combiner consists of a multi-section Wilkinson divider similar to the one published in [82]. A picture of the opened housing is shown in Fig. 4.18 (a); the S-parameter characterization can be seen in Fig. 4.18 (b). The circuit has an insertion loss of 1.5 dB and a flat transmission characteristic.

4.4.1 Multipath Propagation

In addition to receiving a signal by a direct line-of-sight transmission, a signal can reach a receiver by further transmission paths resulting from reflections of the signal. In free-space transmission, reflections of a transmitted signal can occur at objects in the surroundings of transmitter and receiver. In case of the system presented, which typically would transmit in an indoor environment, reflections can occur at the walls, the floor or the ceiling of a room or at objects placed inside the room, compare with the considerations on reflections affecting the impulse shape in Sec. 2.2.4. Compared to the impulse of the line-of-sight connection, the reflected impulse that reaches the receiver is attenuated and arrives with a time delay. Additionally, the impulses are traveling from air, with a relative dielectric constant $\epsilon_{r,Air} = 1$, into a medium with a higher dielectric constant. Using the calculations (3.1) and (3.2) from the previous section, this always results in a negative reflection coefficient

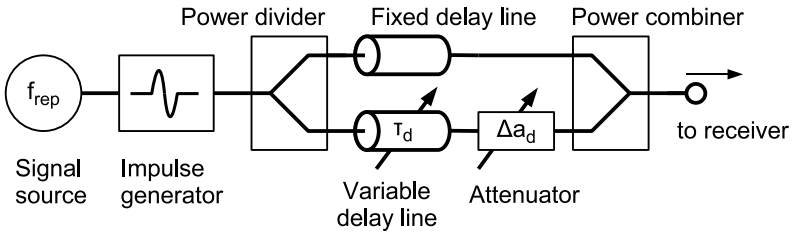

Figure 4.19: Block diagram of the FM IR-UWB transmitter with splitting section for multipath channel measurements.

Γ, which indicates a shape inversion of the reflected impulses. In case of multiple reflections, both impulse orientations can occur.

To assess the effect of the multipath propagation by measurements, the closed system demonstrator is extended. As the block diagram of Fig. 4.19 presents, the output of the impulse generator is divided by the UWB power divider. The split signals are fed through a transmission line with a fixed line length, imitating the line-of-sight connection, and a transmission line with an adjustable line length in the other branch, representing the delayed reflection. Additionally, the second branch can be attenuated to measure the influence of an attenuated reflection. At the output of the lines, the signals are combined by another power combiner, passed through a 40 dB attenuator to operate the receiver in the linear range and fed through cables to the LNA of the receiver. Modeling the reflected signal by a splitting arrangement lacks the inversion of the impulse shape as discussed above. However, the missing shape inversion only has an effect, when the delayed impulse overlaps with the non-delayed impulse which, due to the short impulse duration, rarely takes place. Far from overlapping, the missing shape inversion in the splitting arrangement has no negative influence on the evaluation of the multipath effect, because in the rectifier, the impulse orientation is lost regardless.

In the demodulator, the carrier level is noted as the measure of input signal power. The measurements are done with three different relative attenuations Δa_d of 0, 3 and 10 dB between the branches and a time delay between the impulses τ_d between -0.3 and 10.2 ns, which is more than one complete impulse repetition cycle $1/f_{rep} = 10$ ns. The measurement results are depicted in Fig. 4.20 (a) for the complete delay and all three attenuations. The measurement results illustrate two specific effects. The first effect occurs for small delays (i.e. delays around ± 0.4 ns), causing the direct and the delayed impulse to overlap each other. This region is shown in an enlarged plot in Fig. 4.20 (b). As discussed before, this is not correctly

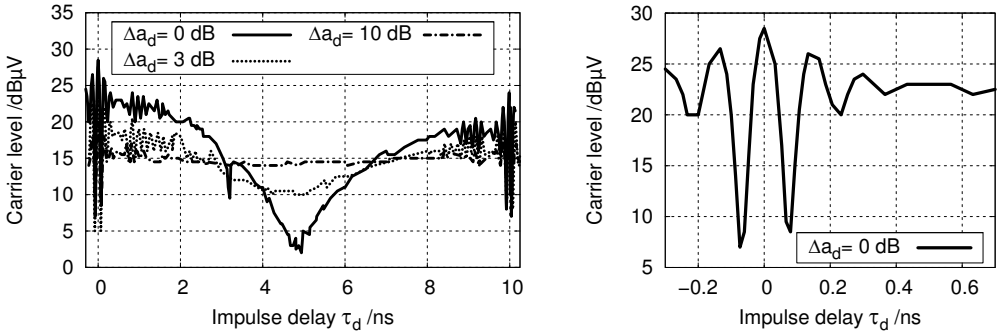

(a) (b)

Figure 4.20: Measured carrier level versus time delay between the impulses (a) for a complete impulse repetition and the different attenuations between the two branches and (b) at the special case position where the impulses overlap.

modeled in the applied delay-line measurement setup, because in a real-world setting a shape inversion of the reflected signal takes place. But, keeping this in mind, the interpretation of the non-inverting measurement allows transferring the results to the other case. In the overlap region small impulse delays can cause high fluctuations of the carrier level, which are due to both constructive and destructive interferences with the impulse cycles. For no delay (τ_d =0 ns) between the impulses, an approximately 6 dB higher carrier level can be observed in the measurement compared to the delay $\tau_d = 0.5$ ns, where the impulses do not overlap any more. This is because of doubling the amplitude and the quadratic slope of the rectifier. In case of bringing now a shape-inverted impulse with no delay and no attenuation together with a normal impulse, the amplitudes would cancel each other. The effect of overlapping impulse summation occurs only in a very narrow delay region but can occur on multiply reflected impulses as well. This can be seen in the ripples in the curves of Fig. 4.20 (a) at around $\tau_d = 1$ ns. These ripples are caused by impulse summations too; in this case because of reflections occurring in the splitter/ combiner arrangement.

The second effect visible in Fig. 4.20 (a), which occurs at delays $\tau_d > 0.4$ ns, is similar to a flat fading of narrowband systems. Here the harmonics of the first and the second impulse are interfering with each other, which results in a decreasing (and later increasing) carrier level. To show the origin of the effect, Fig. 4.21 presents two measurement examples of the fading behavior of two impulses with different

time delays in the spectral domain. Fig. 4.21 (a) illustrates the spectrum with a delay $\tau_d = 0.7$ ns between the impulses. This represents a fading behavior with a spectral repetition of $\Delta f_d = 1/\tau_d = 1.42$ GHz. The suppression of the spectral components can be seen clearly at around 6.4 GHz. Fig. 4.21 (b) presents the spectrum when the second impulse is delayed by $\tau_d = 5$ ns, which is half of the repetition interval. Here the fading occurs at $\Delta f_d = 200$ MHz. As Fig. 4.21 (b) illustrates, in this special case every second harmonic is missing which is equivalent to a transmission with a doubled repetition rate of 200 MHz. As a result, the 100 MHz signal component at the output of the rectifier is strongly suppressed, and the carrier level at the demodulator input decreases strongest for the delay of $\tau_d = 5$ ns. Observing Fig. 4.20 (a), it can be concluded that an increasing time delay between the impulses continuously decreases the spectral content in the rectified 100 MHz signal component. The fading effect becomes strongest when the delay between the impulses $\tau_d = T_{rep}/2$. Additionally it can be investigated in Fig. 4.20 (a) that for an attenuation of the reflection branch of $\Delta a_d = 0$ dB the fading effect is strongest, while the fading influence nearly disappears at an attenuation $\Delta a_d = 10$ dB.

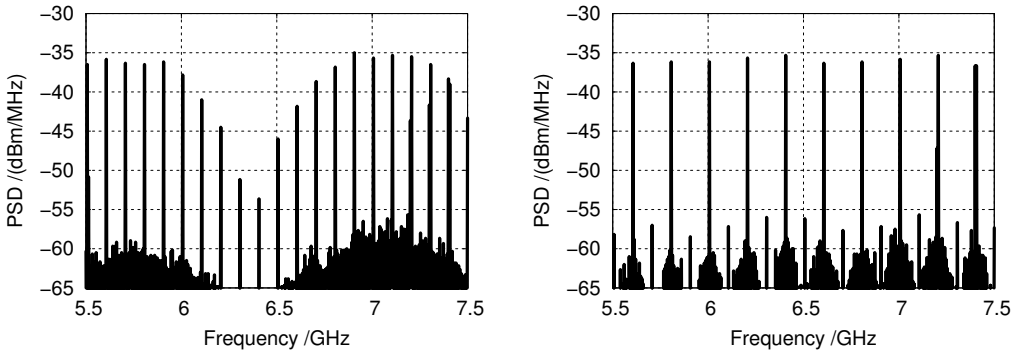

Figure 4.21: Fading effect of two impulses with a time difference (a) $\tau_d = 0.7$ ns and (b) $\tau_d = 5$ ns.

As shown, the simple FM IR-UWB transmission system is affected by multipath effects in a way very similar to narrowband transmission systems. By improving the receiver structure, a receiver according to Fig. 4.22 could be built that is robust to multipath propagation. It uses a two-branch structure which, after the rectifier, incorporates a filter bank with two bandpass filters. One bandpass filter selects the first harmonic at 100 MHz directly. The second incorporates the 200 MHz harmonic and uses a frequency divider to bring the 200 MHz harmonic to 100 MHz. Both are

combined and passed to the demodulator. Thus, harmonic signal power for demodulation of either the 100 MHz or the 200 MHz harmonic is present at all times.

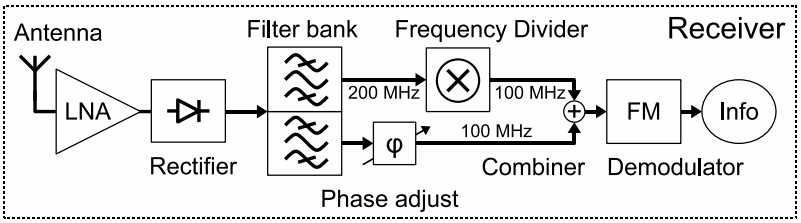

Figure 4.22: Proposed FM IR-UWB receiver structure robust in a multipath environment.

4.4.2 Multi-User Environment

The proposed FM IR-UWB method is investigated for its multi-user capability, which allows a simultaneous operation of several FM IR-UWB transceivers in close vicinity, without disturbing each other. For an FM IR-UWB system, the idea is to separate channels by using different impulse repetition rates f_c. This is similar to tuning to different FM center frequencies in conventional FM radio. With this the spectral space between the impulse harmonics emitted by one user can be used by other users. However, for an investigation of the minimal necessary frequency spacing the situation is more complex. According to the modified Carson bandwidth (4.2), the spectral broadening of the impulse emission at higher harmonics is much larger. Therefore, the entanglement of the impulse spectra of the two users has to be taken into account. The minimally necessary spacing is investigated by measurements using two transmitters, which are connected by a power combiner whose

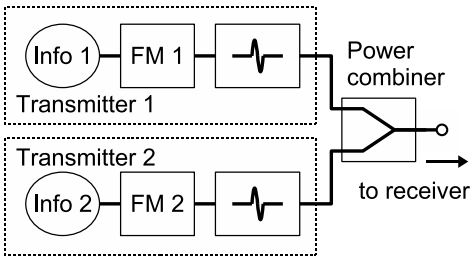

Figure 4.23: Block diagram of the setup for measurement with two users in an ideal transmission channel.

output is connected to the input of the receiver. A block diagram of this setting is given in Fig. 4.23. With this setup, the parameters for two users can be defined individually and the occurring effects characterized in an ideal transmission channel.

Fig. 4.24 (a) exhibits a spectral-domain measurement at the output of the power combiner. The first transmitter uses an impulse repetition rate $f_c = 100\,\text{MHz}$, seen in the spectral signals at 6.4, 6.5 and 6.6 GHz, and the second transmitter a repetition rate $f_c = 99.5\,\text{MHz}$, seen in the spectral signals at around 6.37, 6.47 and 6.57 GHz accordingly. Fig. 4.24 (b) plots a spectral domain measurement at the out-

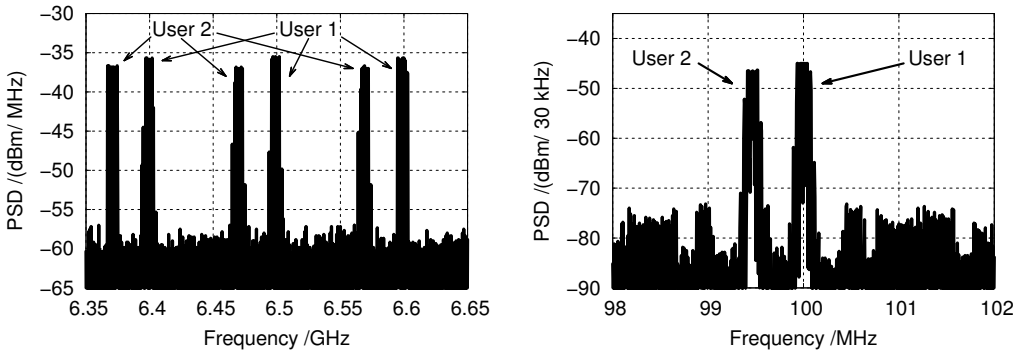

Figure 4.24: Spectral domain of two FM IR-UWB transmissions; (a) at the output of the combiner and (b) at the output of the rectifier's bandpass filter.

put of the low-pass filter. Here the recoverable repetition rates of the first and second transmitter at 100 MHz and 99.5 MHz, respectively, are displayed. By choosing the corresponding center frequency in the demodulator, either the first or the second transmitted information signal can be demodulated. The spurs in the vicinity of the main spectral signals in Fig. 4.24 (b) are mixing products due to the rectification. To determine the minimal necessary channel spacing of two closely spaced transmitting systems, the first transmitter is kept at the fixed repetition rate $f_c = 100\,\text{MHz}$, while the one of the second transmitter is varied. In the first transmitter, FM rates $f_{s,max} = 2\,\text{kHz}$ and 20 kHz are applied, while in the second transmitter FM rates $f_{s,max} = 1.95\,\text{kHz}$ and 19.95 kHz are used. The small FM rate differences are used to avoid interferences in demodulation. In the receiver, the demodulated information signal of the first transmitter is monitored in spectrum, which for the single-user case is a pure sinusoidal at either 2 kHz or 20 kHz. When the repetition rates f_c of the two transmitters are approaching each other, the pure sinusoidal is distorted,

which can be seen in spurs in the demodulated spectrum. A measure for these distortions is the spurious-free dynamic range (SFDR), defined as the power ratio of the wanted signal to the next strongest spurious signal [65]. A comparison of the measurements of the SFDR versus the repetition-rate difference Δf_{rep} of the two transmitters is shown in Fig. 4.25.

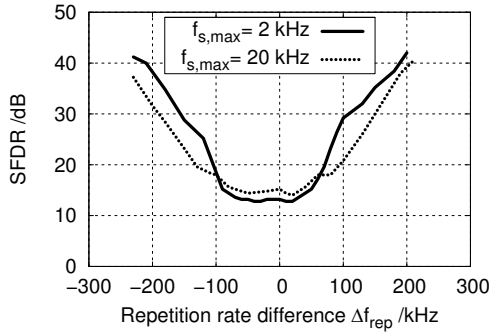

Figure 4.25: Spurious-free dynamic range (SFDR) of the information signal versus the repetition-rate difference of two users for FM rates $f_{s,max} = 2$ kHz and 20 kHz.

It is evident that the closer the repetition rate of the second transmitter gets to the repetition rate of the first transmitter, the worse the SFDR becomes. To achieve e.g. an information signal SFDR of 30 dB, it is necessary to choose a repetition-rate separation of more than 150 kHz for an FM rate of 2 kHz and a separation of more than 200 kHz for an FM rate of 20 kHz. Keeping in mind that the Carson bandwidth of a conventional FM radio system is 124 kHz for an FM rate of 2 kHz and 160 kHz for 20 kHz, the influence resulting from the spectral broadening can be neglected and users can be separated as in conventional FM radio.

4.4.3 Narrowband Interference

Another perturbation effect which has to be validated on an FM IR-UWB transmission is the robustness to narrowband interferers. This is of special concern, since UWB systems share their band with other wireless services, as mentioned in Sec. 2.1. In this section the influence on the FM IR-UWB system behavior is evaluated for narrowband interferers which are located within the FCC UWB band from 3.1–10.6 GHz and cannot be blocked by an appropriate bandpass filtering. The investigations concentrate on the influence on the modulation, not on linearity

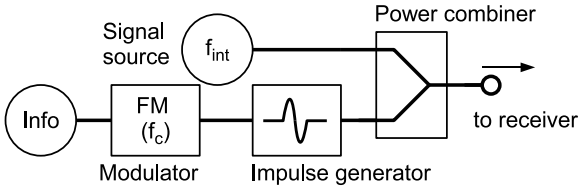

Figure 4.26: Block diagram of the setup for narrowband interference evaluation.

constraints of the receiver. First some general considerations: A sinusoidal signal brought to the input of the FM IR-UWB receiver without a present impulse train will be rectified by the diode to DC and twice its signal frequency and will be suppressed by the subsequent bandpass filter. Therefore, an interferer in absence of an UWB impulse train cannot bring a disturbing signal to the input of the demodulator. Having a narrowband interferer together with an UWB impulse train, a mixing of the narrowband signal with the spectral lines of the modulated UWB transmission will occur and these mixing products can fall into the receiver bandwidth of the FM IR-UWB system. The influence of these distortions is investigated by measurements in this chapter. In Fig. 4.26 a block diagram of the measurement setup is presented. The signals from an impulse generator and a signal source are combined by a power combiner, which is connected to the receiver by a 30 dB attenuator in order not to overdrive the receiver's LNA.

As discussed in [83], there are two main approaches of applying a narrowband interference. The first approximates the interference using a sinusoidal tone as interfering signal, and the other applies a noise signal with, for example, constant power spectral density across the interfering band. Here, a single tone sinusoidal signal varied in center frequency f_{int} and amplitude is chosen as interferer. Fig. 4.27 (a) presents a spectral-domain plot, measured at the output of the power combiner for a modulated 100 MHz UWB impulse train and a narrowband interferer with $f_{int} = 7.605$ GHz. The narrowband interferer has a relative emission level of 30 dB above the highest UWB spectral component. At the output of the rectifier, mixing products of the narrowband with the UWB signal appear. Fig. 4.27 (b) shows the rectified signal around 100 MHz of a modulated UWB transmission with $f_c =$ 100 MHz and an unmodulated narrowband interferer with $f_{int} = 7.605$ GHz. The mixing products fall into the input bandwidth of the demodulator when the interferer frequency f_{int} is close to a harmonic of the impulse signal. The influence of the interference can be assessed best on the demodulated information signal with the spurious-free dynamic range (SFDR) again being taken as a measure for infor-

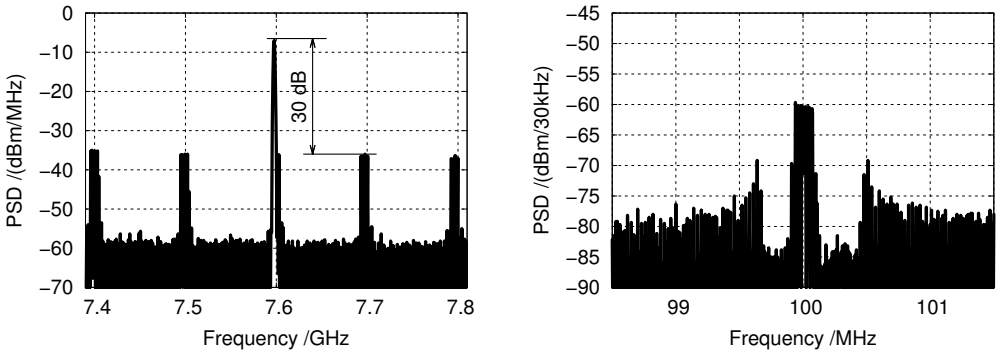

Figure 4.27: Spectral plots of a modulated FM IR-UWB emission with $f_{rep} = 100\,\text{MHz}$ and a sinusoidal interferer at $f_{int} = 7.605\,\text{GHz}$ at the output of the (a) combiner and (b) rectifier.

mation signal purity. Fig. 4.28 (a) depicts a plot of the SFDR versus the offset frequency Δf_{int} for interferer frequencies f_{int} around 4.5 and 7.6 GHz. In both cases the same relative spectral emission level of 30 dB is applied.

As shown in Fig. 4.28 (a), the sinusoidal interferer around 7.6 GHz shows a stronger influence on SFDR than the interference around 4.5 GHz. This is because the spectral harmonic of the transmitted UWB impulse has a larger spectral amplitude at 7.6 GHz than the UWB harmonic at 4.5 GHz. Furthermore, the interference around 7.6 GHz influences a wider frequency band than the interference around 4.5 GHz. This can be explained by the broadening of the UWB harmonics according to the modified Carson bandwidth (4.2). When dividing the measured peak broadenings in Fig. 4.28 (a) by the corresponding harmonic number, the peak broadening of the original modulated carrier signal can be calculated and the measurements can be compared. For the 7.6 GHz harmonic, $\Delta f = 8.8\,\text{MHz}/76 = 115.7\,\text{kHz}$ is obtained and for the 4.5 GHz harmonic $\Delta f = 5.2\,\text{MHz}/45 = 115.5\,\text{kHz}$ is received; these results are in very good agreement to each other. The general shape of the curves in Fig. 4.28 (a) can be explained by the spectral distribution of a frequency-modulated carrier signal. The spectral amplitude distribution of any frequency-modulated carrier signal follows the Bessel functions, which depend on the FM deviation and the FM rate. With the applied FM rate and FM deviation, the maximum amplitudes in the two-sided spectrum have a frequency distance of around 114 kHz between each other, which is very close to the measured and computed values of the peak broadening. A closer investigation into the spectral distribution of frequency modulation

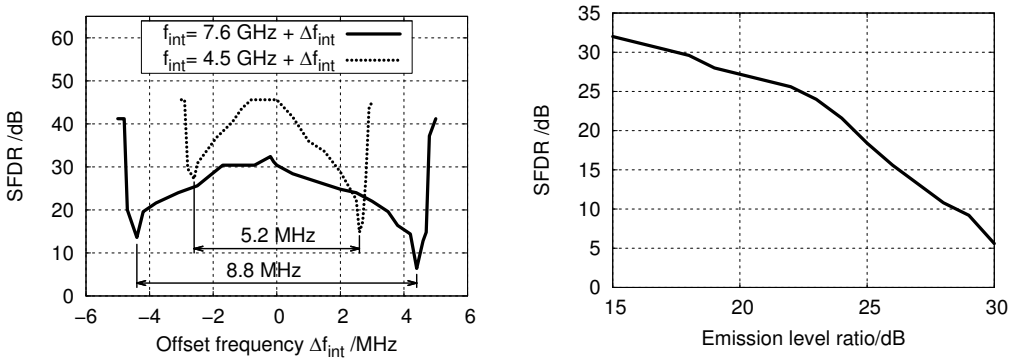

(a) (b)

Figure 4.28: (a) SFDR versus offset frequency for a 100 MHz UWB transmission interfered by a sinusoidal signal with f_{int} around 4.5 and 7.6 GHz. (b) SFDR versus the relative spectral emission power difference at the frequency of the strongest interference $f_{int} = 7.6044$ GHz.

can be found in [72]. As presented, narrowband interferences can have an influence on the FM IR-UWB transmission when directly hitting a UWB spectral component.

In another measurement, the influence of a varying interferer amplitude is investigated. As an example, the interferer frequency $f_{int} = 7.6044$ GHz, as the frequency of the strongest interference, is taken and varied in relative emission level. While varying the relative emission level, the influence on the SFDR is measured, which is plotted in Fig. 4.28 (b). Obviously, decreasing the relative emission level improves the SFDR and thereby decreases the influence of the interferer.

Based on the presented evaluations, it can be concluded that narrowband interferers influence the operation of an FM IR-UWB system only in the close vicinity of the harmonics of the UWB transmission, which drastically reduces the probability of a conflict. Even in case of an interference hitting a spectral line, the extent of the influence depends on the power level of the interferer. However, a jamming of the transmission is easily possible when two interferers are spaced with a difference of the UWB impulse repetition rate. Then, by the rectification, mixing signal components directly interfere with the signal for demodulation. But in all narrowband interference cases, a simple change of the repetition rate will resolve the FM IR-UWB transmission. Thus, the FM IR-UWB system can be considered to be robust to narrowband interferers.

5 Advanced Concepts

In this chapter concepts are described which can advance the UWB radar sensor and the FM IR-UWB communications system. First a UWB antenna array is shown which can confine the radiated impulse more narrowly into a specific direction and also allows to control the radiated beam electronically. Then an impulse generator targeting the European UWB mask is presented which can adopt the presented concepts to a different spectral mask. Last a biphase modulator is described which can be used for a user discrimination of radar sensors by applying a pulse amplitude modulation with a biphase spreading sequence.

5.1 Electronically Beam-Steerable UWB Antenna Array

Antenna arrays are generally used to increase the directivity of a single antenna element, thus concentrating the transmitted energy in a smaller main beam or reducing signal perturbations in the receiver by suppressing interferences from undesired observation angles. An additional advantage of an array is that the direction of the antenna's maximum radiation can be controlled by modifying the signal delay for the individual antennas. If this is done electronically, the antenna beam can be shifted without mechanical rotation of the antenna. In the framework of this project, an antenna array can be used in both the radar sensor and the analog communication system. In the FM IR-UWB communication system, the directive beam can focus the radiation to the base station node, thus increasing the transmission distance. In the radar sensor, the beam-steerable antenna array can be used to focus the radiation beam to the object under scrutiny and can therefore be used to increase the reflected and received impulse energy and decrease the influence of unwanted reflections from objects in close vicinity of the covered area. In case the object is not located directly in front of the radar sensor, beam steering can be used to direct the beam to the region where the largest determinable deviation occurs. This, however, requires appropriate algorithms, which are out of scope of this study.

In the literature, promising UWB antennas (e.g. [62, 84–86]) and antenna arrays (e.g. [87, 88]) for the FCC-allocated UWB frequency range have been documented

that fulfill the requirements of the UWB frequency band. The characterization of the antenna arrays is mainly done using fullband frequency-domain characterization. Mostly missing is a characterization using the targeted time-domain impulse shape, which gives an illustrative insight into the use of antenna arrays for impulse-radio purposes. While the advantages of beam steering have been frequently described, only few actual concepts applicable to UWB technology have been published so far. This is mainly due to the difficulty of generating a tunable ultra-wideband true-time-delay element in the RF domain. One interesting beam-steering concept is shown in [89]. In this concept broadband power dividers split the input signal to four microstrip lines which are feeding the antenna array. A triangular perturber is placed above these feeding lines. Bringing the perturber closer to the transmission lines, the phase velocity on the four feeding lines is altered which results in a delay of the containing signals. This concept works for all UWB signals, e.g. spread-spectrum UWB as well as impulse-radio UWB, but requires mechanical parts and a large control voltage for the piezoelectric perturber actuation. In the following section an innovative concept is presented, which avoids the use of the mechanical parts and applies a purely electronical beam steering.

5.1.1 Introduction to the Principle

The basic principle of an antenna array is to place individual antenna elements at a certain spacing d side by side to each other, forming a one- or two-dimensional arrangement. Doing so, the radiated impulses of each element will influence the radiation behavior of the antenna arrangement compared to a single antenna element. In this study the properties of a one-dimensional antenna array with four individual antenna elements is investigated, but the principle can be transferred to a different number of antenna elements or two-dimensional arrays.

A typical antenna array setting can be seen in Fig. 5.1. Impulses which are emitted simultaneously by each of the four transmit antennas form an impulse front in the direction 0°. The angle 0° is the angle of the constructive summation of the impulses in the far field of the antennas resulting in a maximized merged radiation. When a receiver is placed at an angle Θ, there is a small time delay τ between the individual impulses arriving in the receiver. The summation of the impulses with this delay results in a changed impulse shape with decreased amplitude summation. The summation behavior versus investigation angle Θ of the receiver depends on the radiated impulse shape applied. For the investigations in this section, each individual antenna element radiates a fifth Gaussian derivative impulse with a $\sigma = 51$ ps;

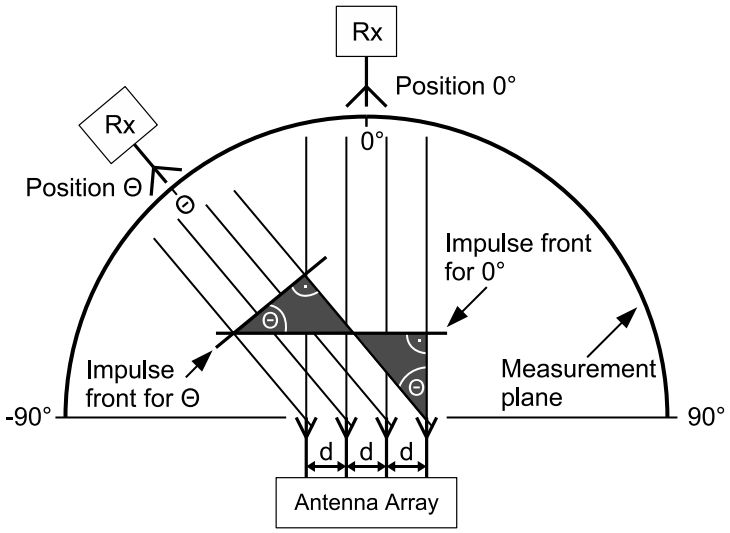

Figure 5.1: Illustration of an antenna array with two different receiver locations.

other impulse shapes can be investigated similarly. In order to set up a formula of a general N-element array, the gated sinusoidal impulse representation (2.5) of the fifth Gaussian derivative is used. With this the array formula can be expressed by

$$f_N(t,\tau) = \sum_{n=0}^{N-1} \left[\frac{1.11}{N} \cdot \exp\left(\frac{-(t+n\cdot\tau)^2}{2\sigma^2} \right) \cdot \sin(\omega(t+n\cdot\tau)) \right], \qquad (5.1)$$

where τ is the time difference of arrival of impulses emitted by neighboring antenna elements, $\sigma = 76.5$ ps is the standard deviation[1] and $\omega = 2\pi \cdot \mathrm{f} = 2\pi \cdot 7$ GHz is the impulse center frequency of the impulse fitting the FCC indoor mask. N is the number of antenna elements and $1.11/N$ is a normalizing factor to obtain a unity amplitude, where the 1.11 is a calculated value of the factor $A/(\sqrt{2\pi}\cdot\sigma)$ from (2.5). Using trigonometry and free-space propagation with c_0 as the speed of light, the time difference τ between neighboring impulses with respect to the angle of investigation Θ and the distance between the neighboring antenna elements d can be calculated as

$$\tau = d/c_0 \cdot \sin(\Theta)\ . \qquad (5.2)$$

The angular behavior is investigated in a time-domain ray simulation using (5.1), (5.2) and $N = 4$ omnidirectional antennas at an initial antenna spacing $d = 10$ cm.

[1] As discussed in Sec. 2.2, the value of the standard deviation σ is different in the representation of the impulse as a derivative of the Gaussian bell shape or a Gaussian-gated sinusoidal.

Fig. 5.2 (a) presents a three dimensional graph of the time-domain amplitudes of an array with antenna spacing $d = 10\,\text{cm}$ versus receiver rotation angle Θ and time in isometric view. Fig. 5.2 (b) shows the same plot but in top view with a gray-shading of the amplitude in z-axis. It can be observed that a focusing of the radiated amplitude takes place at the angle of 0°, while the shape broadens in time for different angles.

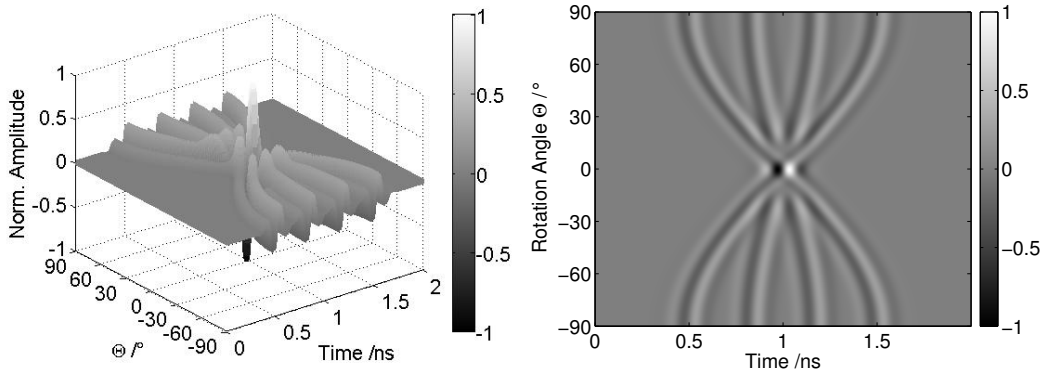

(a) (b)

Figure 5.2: Simulation of the antenna array with four omnidirectional antenna elements at a spacing of $d = 10\,\text{cm}$ versus time and rotation angle Θ in (a) isometric view and (b) top view.

For a better understanding, the impulses radiated by the individual antenna elements and the merged impulse shape are shown in Fig. 5.3 for receive antenna angles $\Theta = 0°$, 11°, 23° and 90°. While all individual impulses overlap constructively at 0°, at 11° the impulses diminish each other substantially. At an angle $\Theta = 23°$ a partially increased amplitude summation of the impulses takes place, and at the outermost angle $\Theta = 90°$ the four individual impulses are clearly separated again.

The amplitude distribution versus rotation angle Θ is best assessed in a plot of the maximum merged impulse amplitude, which can be seen in Fig. 5.4. The angular location of the maxima and minima together with their corresponding amplitude values can be investigated. This graphical representation can be used to compare several antenna arrays. However, the merged impulse is processed differently in an energy-detection receiver or a correlation-detection receiver because the shape of the merged impulse plays an important role, too. As discussed in Sec. 2.3.2, an impulse approaching an energy-detection receiver is squared and integrated, while in a correlation receiver it is multiplied with a template impulse at an ideal time instance

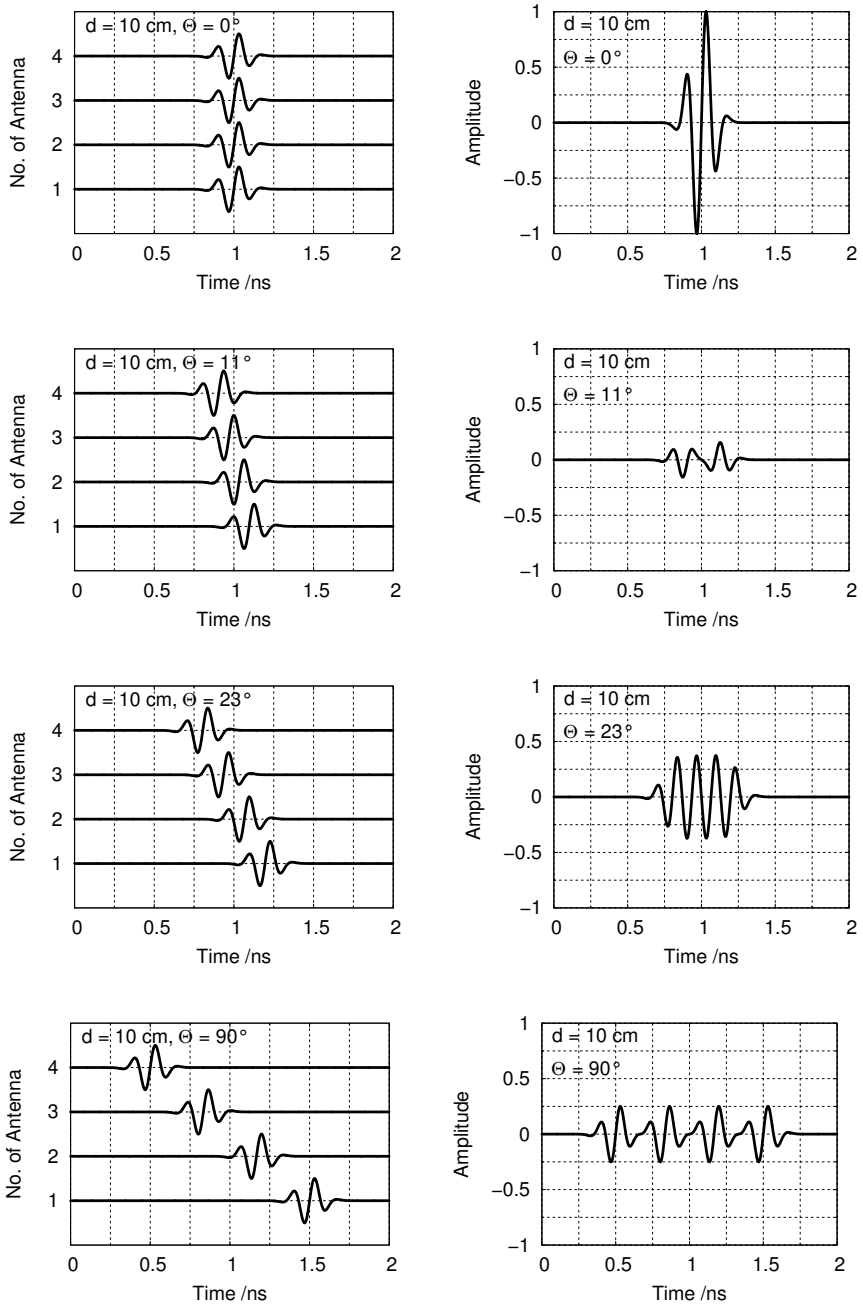

(a) (b)

Figure 5.3: Examples of impulses at selected angles Θ of (a) the individual antenna elements in the transmitter and (b) the merged impulse arriving at the receiver.

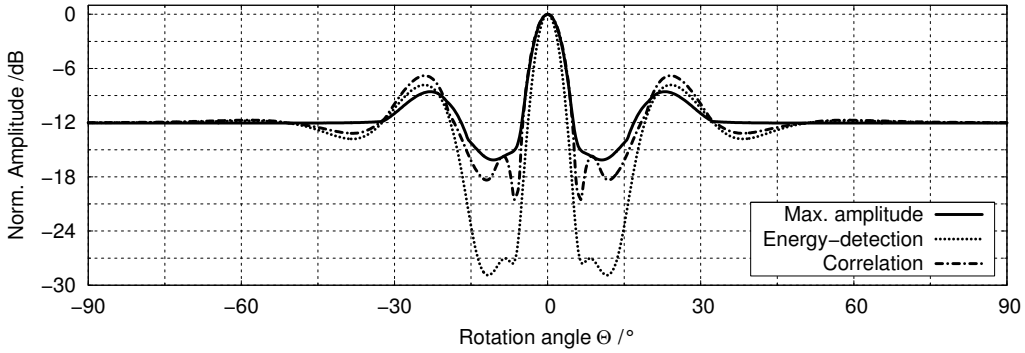

Figure 5.4: Comparison of signal amplitude versus rotation angle Θ using the maximum amplitude of the merged impulse, the signal at the output of an energy-detection receiver and the signal at the output of a correlation-detection receiver.

and integrated. Fig. 5.4 compares the calculated behavior of the output signal of the two receiver types with the curve of the maximum amplitude versus rotation angle Θ, as similarly described in [90]. All curves show a maximum at 0° and intermediate maxima and minima, which are similar to side lobes of a narrowband antenna array. The side lobes appear approximately at the same angle instances for all three curves. The main beam of the energy-detection receiver signal is slightly smaller compared to the other curves, which is due to the squaring of the impulse in contrast to a multiplication with a constant template signal amplitude in the correlation receiver. At the angles of $\pm$90°, the curves reach a plateau of -12 dB, which gathers the energy of a single individual impulse only. Because the general angular behavior of all three curves is very similar, in the following only the plot of the amplitude distribution is shown.

By varying the distance d between the antenna elements, the width of the radiated beam and the angular location of the side-lobe maxima and minima can be altered, as shown in Fig. 5.5. The corresponding angular 3 dB width of the beam can be calculated using (5.1) with $N = 4$ antenna elements. Here, $f_4(t, \tau) = 1/\sqrt{2}$ must be solved for τ, for which no closed-form solution exists. By iteration $\tau = 15.16$ ps is found for an array with four elements. This, together with (5.2), leads to the 3 dB beamwidth

$$\Theta_{3dB,4} = 2 \cdot \arcsin\left(\frac{c_0}{d} \cdot 15.16\,ps\right) , \tag{5.3}$$

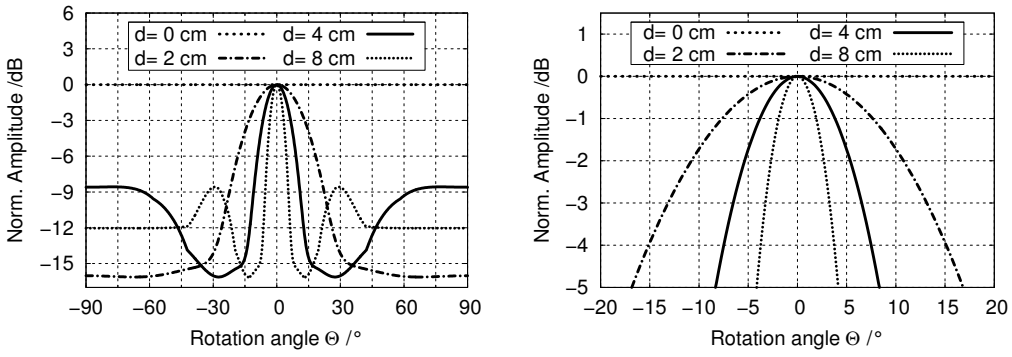

Figure 5.5: Comparison of the amplitude maximum for different antenna distances d in (a) complete and (b) partial view of the main beam.

where d is the distance between the antenna elements, c_0 is the speed of light and the factor 2 is the extension to both sides. The angular position of the side lobe minimum and maximum can be estimated in analogy to narrowband systems, using the sinusoidal part of the Gaussian-gated sinusoidal representation (2.5) only. The minimum appears approximately where the sinusoidals overlap at a phase difference of 180°; the maximum again at 360°, which is independent of the number of antenna elements N. The formation of the minimum and maximum for the array with $d = 10\,\text{cm}$ can again be investigated in the time-domain plots in Fig. 5.3. Using the phase difference, the center frequency f and (5.2) the approximate angle of the angular minimum Θ_{min} and maximum Θ_{max} can be calculated to

$$\Theta_{min} \approx \arcsin\left(\frac{c_0}{2 \cdot d \cdot f}\right) \quad ; \quad \Theta_{max} \approx \arcsin\left(\frac{c_0}{d \cdot f}\right) , \tag{5.4}$$

where c_0 is the speed of light, d is again the spatial difference between the antenna elements and f is the sinusoidal center frequency of (5.2) (here: $f = 7\,\text{GHz}$). Despite a good agreement, these formulas are estimations only, because precisely due to the gating with the impulse envelope, the sine wave minima and maxima are slightly shifted towards the envelope maximum. This results in a small overestimation of the delay-time difference in (5.4), but this small error shall be neglected here.

For an electronic beam steering of the antenna beam, the impulse front introduced in Fig. 5.1 must be changed in order to be perpendicular to the angle of the wanted direction. This means that the impulses of the antenna elements must be delayed

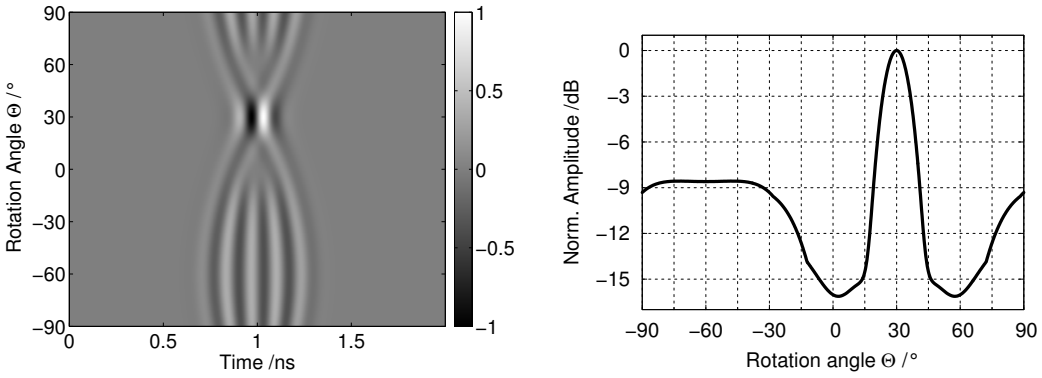

(a) (b)

Figure 5.6: Beam steering applied for an array with $d = 4$ cm in (a) 3D top view and (b) amplitude maximum versus rotation angle.

with respect to each other accordingly. This delay between the elements can again be calculated by (5.2). A simulation example with an antenna spacing $d = 4$ cm and pointing at $\Theta = 30°$ is plotted in Fig. 5.6 (a) in a 3D top view and in Fig. 5.6 (b) in the amplitude distribution versus rotation angle. The angular shift of the main beam is clearly evident, while the 3 dB beamwidth and the side lobe distribution with respect to the main radiation angle remain unchanged in comparison to the corresponding plot in Fig. 5.5. In the next section measurements are presented and compared to the obtained simulations.

5.1.2 Measurements on a 4x1 Antenna Array

In order to measure and verify the time-domain performance of a four-antenna transmit array, an arrangement is built using four Vivaldi antennas with mounted impulse generator from Sec. 3.2.3. The four Vivaldi antennas are placed in a collinear arrangement in the H-plane, as can be seen in Fig. 5.7. In contrast to the beam-steering concept using a broadband true time-delay in the RF domain, e.g. implemented in [89], this study proposes an easier concept of beam steering for IR-UWB systems, which uses four individually controllable signal sources for the triggering of the applied impulse generators. The four signal sources are synchronized via the built-in 10 MHz synchronization reference. The idea is to phase-shift the trigger control signal in the low-frequency domain, which is much easier than providing a broadband true-time delay in the RF domain. By changing the phase φ_N of the triggering signal for each source N, the individual time delay of each impulse can be

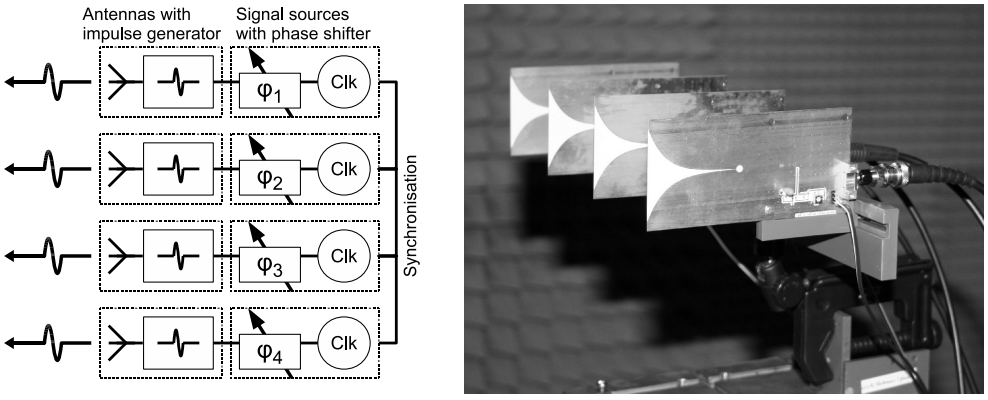

(a) (b)

Figure 5.7: UWB transmit antenna array. (a) Block diagram and (b) photograph.

controlled and thus different steering angles Θ can be chosen. To adjust the steering angle, the phase of the triggering signal must be set according to

$$\varphi_N = \frac{f_c \cdot d}{c_0} \cdot \frac{360^\circ}{N-1} \cdot \sin(\Theta) \ , \tag{5.5}$$

where f_c is the impulse repetition rate, d is the lateral distance between the antennas and c_0 is the speed of light.

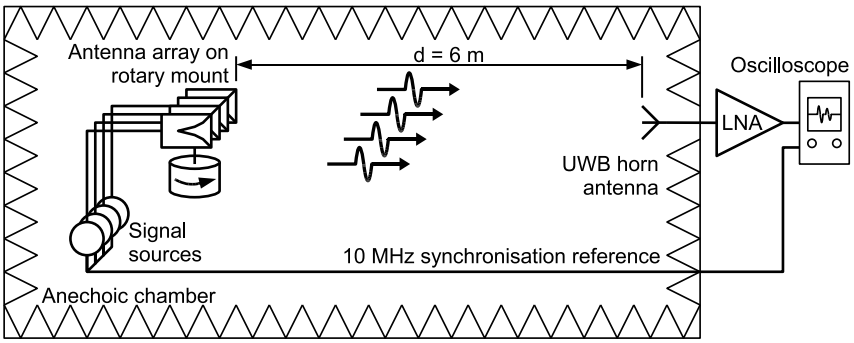

Figure 5.8: Sketch of the antenna array measurement setup.

The current measurements are conducted in an anechoic chamber at a distance of 6 m between transmitter and receiver. A sketch of the arrangement can be seen in Fig. 5.8. At the receiving side, a UWB low-dispersive ridged-waveguide horn antenna is connected to the UWB low-noise amplifier and a real-time oscilloscope.

The 10 MHz synchronization reference is used for synchronization between the signal sources and to trigger the oscilloscope. The array is rotated from -90° to +90° in steps of 1°, and the received time-domain impulse signal is stored for each phase step.

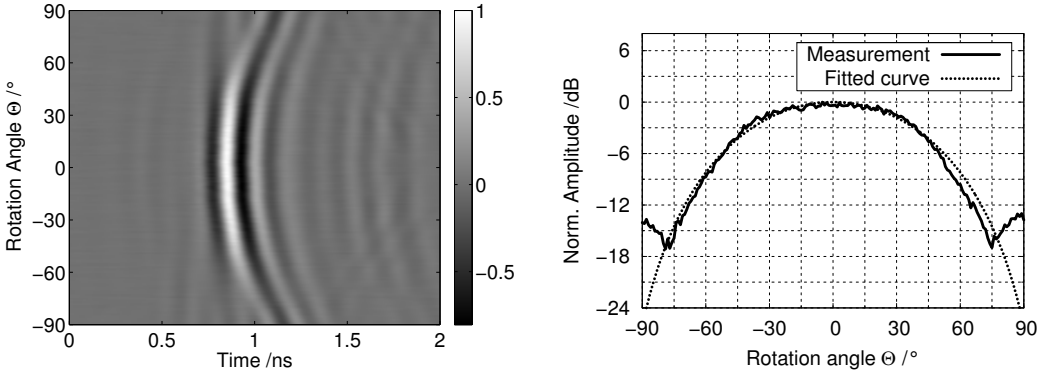

(a) (b)

Figure 5.9: Single antenna element. (a) Measured transient amplitude and (b) amplitude distribution compared to the fitting function.

First a single antenna element is measured versus rotation angle Θ. The plots of the transient measurement in the H-plane are given in Fig. 5.9. The curvature around the time axis in Fig. 5.9 (a) is caused by a small mounting deviation from the center axis on the rotation rack, but has no influence on the results. The angular behavior of the single antenna element can be seen from the extracted amplitude in Fig. 5.9 (b). The antenna is directive and has a beam width of 80°. To include the influence of the directive antenna, the simulation model of the previous section is extended by a fitting of the antenna directivity. A fitting of the directional amplitude shape versus rotation angle Θ is done using

$$A(\Theta) = 0.5 \cdot (1 + \cos(1.714 \cdot \Theta)) \ . \tag{5.6}$$

The fitted directive amplitude distribution is compared to the measured curve in Fig. 5.9 (b). In the following graphs, the measurement using the antenna array is compared to the omnidirectional simulation and the directive simulation using the fitted amplitude distribution.

Two measurements of the antenna array in the H-plane with an element spacing $d = 8$ cm can be seen in Fig. 5.10. In the top row, no beam steering is applied, whereas the bottom row illustrates a beam steered to -20°. To achieve this, the re-

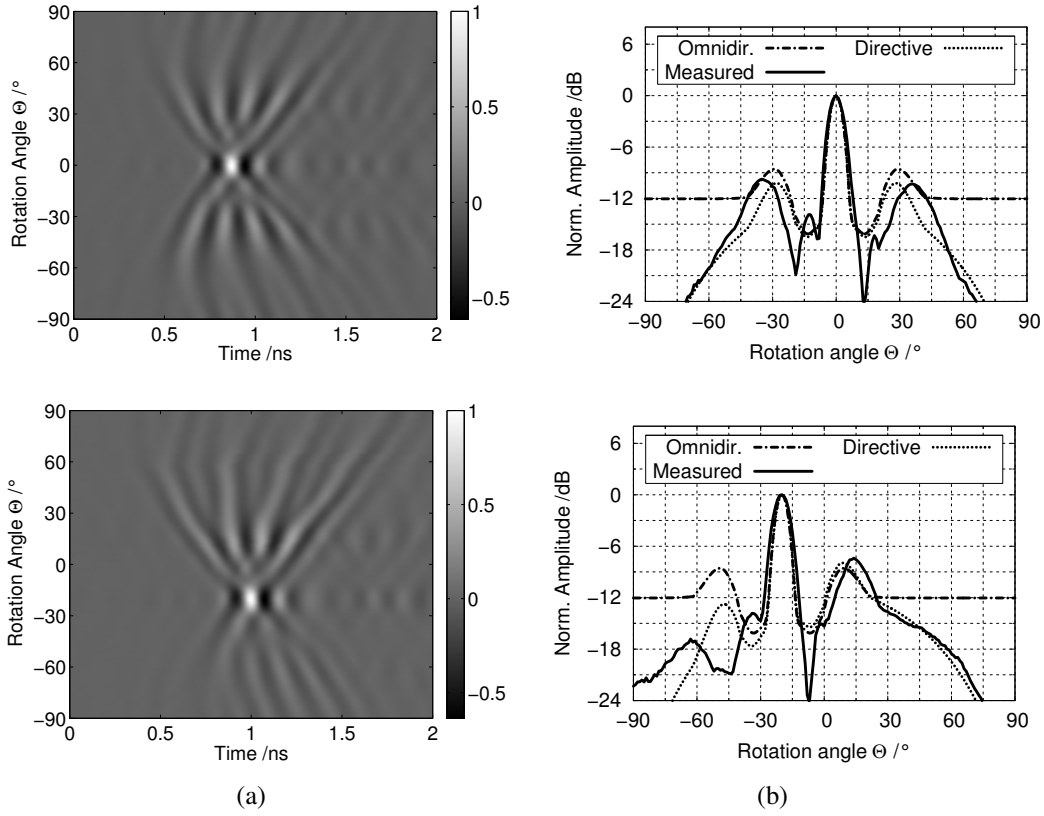

Figure 5.10: Array with $d = 8$ cm and no beam steering (top row) and beam steering to -20° (bottom row) in (a) measured 3D view and (b) comparison of amplitude distribution between measurement, omnidirectional model and directive model.

spective phase shifts are set for each trigger signal according to (5.5). The extracted maximum amplitude distributions are shown in Figs. 5.10 (b) and are compared to the amplitude distribution model of the omnidirectional and the directive single antenna element. The fitting to the directive model is good; the antenna array measurements with a spacing $d = 8$ cm show a focusing of the 3 dB beam width within 8°. The differences between measurement and model are due to slight misalignments in spacing between the antenna elements, slight misalignments in parallel mounting the antenna elements, slightly different lengths of the trigger-signal feeding cables and a broadening of the impulse shapes resulting from the bandwidth limitation of the antennas.

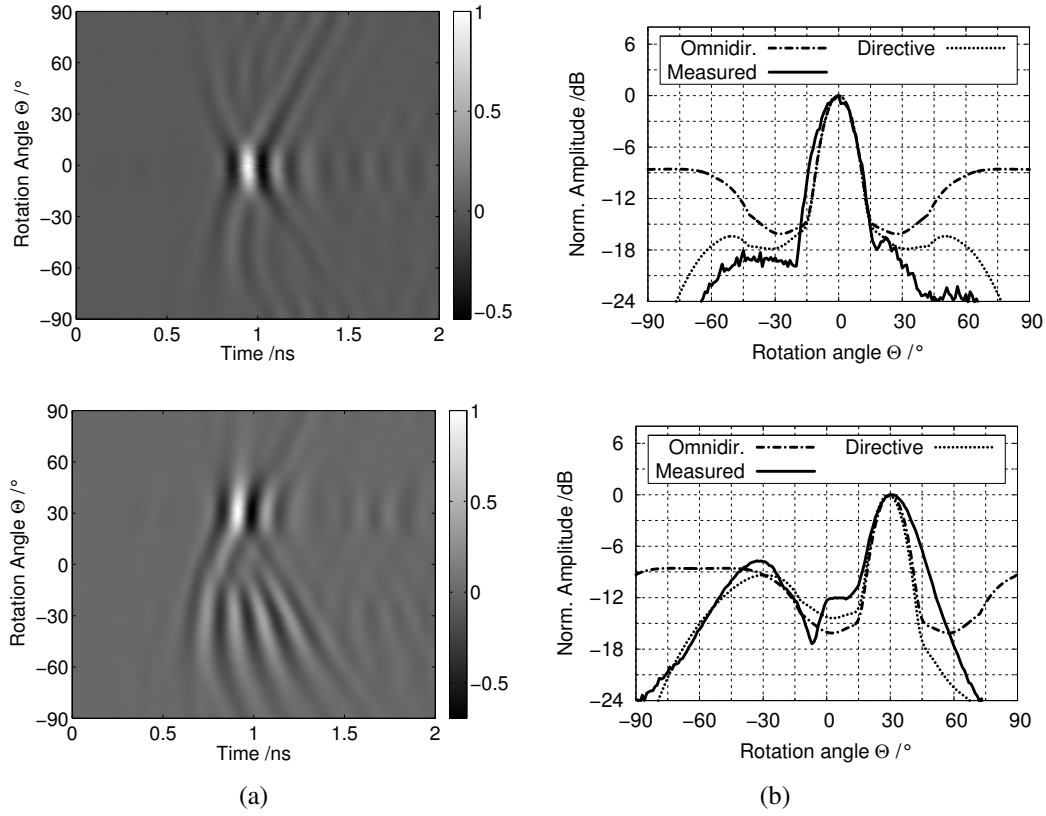

Figure 5.11: Array with $d = 4$ cm and no beam steering (top row) and beam steering to 30° (bottom row) in (a) measured 3D view and (b) comparison of amplitude distribution between measurement, omnidirectional model and directive model.

For further measurements the antenna spacing is reduced to $d = 4$ cm. The top row of Fig. 5.11 gives the measured results of no beam steering applied and in the bottom row with a beam steering to 30°. The array with a spacing of $d = 4$ cm shows a focusing of the 3 dB beam width to 16°. A shift of the main lobe to 30° is clearly visible in the bottom figures. The differences between the measurements and the simulations are attributed to the above-mentioned reasons. The Vivaldi antenna array with a distance of $d = 4$ cm and no applied beam steering constitutes an advantageous trade-off by exploiting the small radiation beam width and the good suppression of the side lobes. However, the side lobes reappear in case of an applied beam steering. A decreased spacing of the antenna elements would suppress the side lobes more strongly, but with the disadvantage of a wider antenna beam.

This section shows that an antenna array can be applied to increase the directivity of a single antenna element for radiated UWB impulses. Simple ray modeling with the presented equations is validated by measurements and is shown to predict experimental results well. The concept is here shown only for a transmit antenna array, but it can be adopted to a receiving antenna array in case a correlation receiver is used. As shown, the antenna array can be implemented in both the UWB radar sensor for breath-rate monitoring and in the FM IR-UWB transmission system.

5.2 Impulse Generator Targeting the ECC Mask

In order to make use of the spectral UWB mask allocated in Europe as introduced in Sec. 2.1 and [12], a UWB impulse generator with a changed impulse shape is necessary. The first-ever implementation of an impulse generator IC is shown which targets this allocation. The IC is designed and fabricated in the 0.8 µm SiGe HBT semiconductor technology of Telefunken Semiconductors having transistors with $f_T/f_{max} = 80/90$ GHz [48, 49].

5.2.1 Circuit Concept and Simulations

The circuit idea is similar to the concept of the FCC-compliant impulse generator introduced in Sec. 3.2.1, but the LC-resonance circuit used for pulse shaping is replaced by a multi-stage structure, due to the higher quality factor required for the European UWB band. The circuit can be divided into four main function blocks, as the simplified circuit schematic of Fig. 5.12 shows. The first two function blocks contain two limiting amplifier stages and a spike-shaping circuit, similar to the FCC-compliant impulse generator.

From the spike-shaping circuit, Gaussian-shaped spikes are fed into the function block for impulse generation, in which a relaxation oscillation is induced in a triple-circuit capacitively coupled bandpass filter. Three LC-resonator stages were found to be necessary to reach the narrow ECC mask. The bandpass filter is designed to have a center frequency in the middle of the ECC mask and a bandwidth to ensure compliance with the mask. The resonating frequency needs to be the same in each LC-resonator stage. Otherwise, a beat frequency between the resonators distorts the time-domain output waveform and leads to ringing, which would enlarge the impulse width. The individual inductance and capacitance values are adjusted, taking

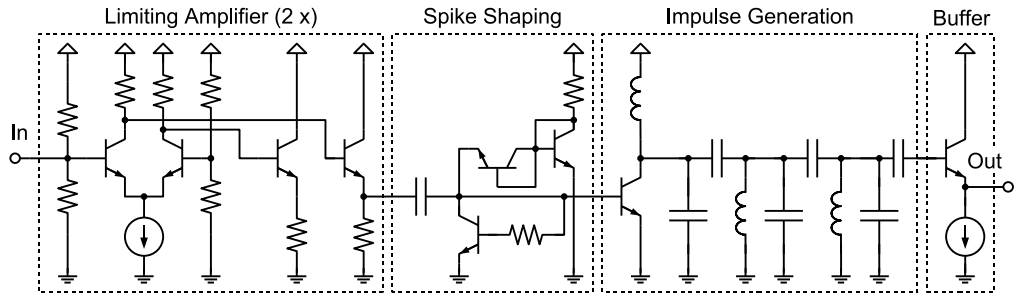

Figure 5.12: Simplified circuit schematic of the impulse generator targeting the ECC mask.

the reactances of source and load impedance into account. The last function block consists of a buffer stage which is used to drive a 50 Ohm load.

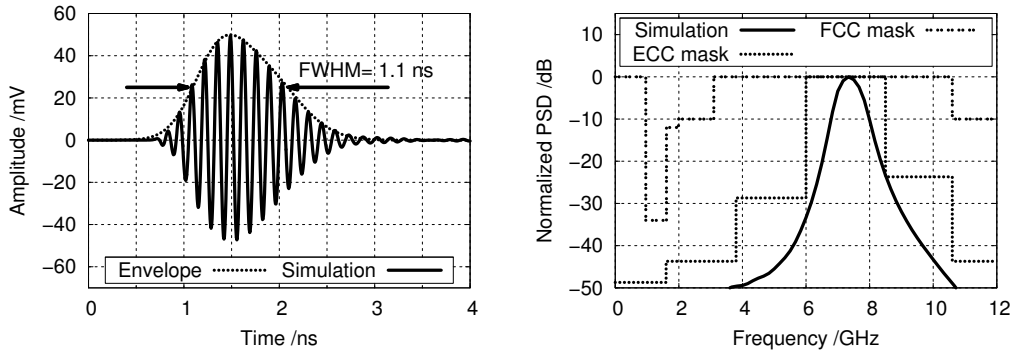

(a) (b)

Figure 5.13: Simulation results of the ECC impulse generator in (a) time and (b) spectral domain.

Fig. 5.13 shows the simulation results for the ECC impulse generator in time and frequency domain. The time extension is 1.1 ns (FWHM) and thus larger than the 0.8 ns predicted in the description of a theoretical impulse shape fitting the ECC mask in Sec. 2.2.2. This enlargement is necessary due to the unsymmetrical rise and fall time of the impulse. The simulated impulse emission fits into the ECC-allocated UWB mask.

5.2.2 Measurement Results

The fabricated circuit is characterized by on-wafer measurements using a signal source with a 200 MHz sinusoidal signal at the input of the IC to generate an unmodulated impulse train with a 200 MHz repetition rate. Fig. 5.14 (a) gives the recorded output waveform of a single impulse. The generated impulse has a peak to peak amplitude of 32 mV and a time-domain extension of 0.83 ns (FWHM).

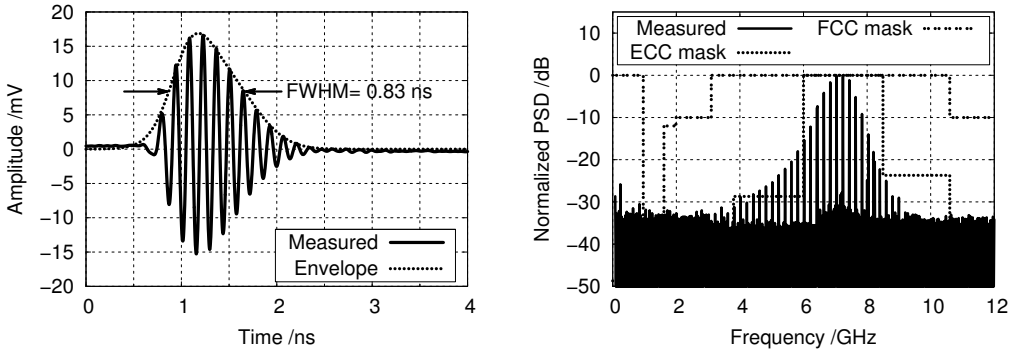

(a) (b)

Figure 5.14: Measurement results of the ECC impulse generator in (a) time and (b) spectral domain.

In order to assess the frequency-domain behavior, a spectrum analyzer is connected to the impulse generator output. Fig. 5.14 (b) shows the measured normalized power spectral density (PSD) of the unmodulated 200 MHz impulse train in a 1 MHz resolution bandwidth. The maximum measured PSD is -44.2 dBm/MHz. The normalized impulse is compared with the normalized European and FCC indoor masks. This graph shows that the upper part of the impulse fits into the European mask very well, while the lower part violates the mask at approximately -15 dB from the maximum value.

This deviation from the simulation is most probably due to the coupling capacitances between the LC-resonant stages. With a value of 55 fF, the capacitances are close to the minimal-producible capacitance value of the semiconductor technology. For these small values the simulation models can deviate significantly. In a transmission system, this violation of the mask could be adjusted by a bandpass filtering, which may be part of the transmit antenna. Compared to an impulse completely filling the ECC mask, the presented impulse shows an implementation loss

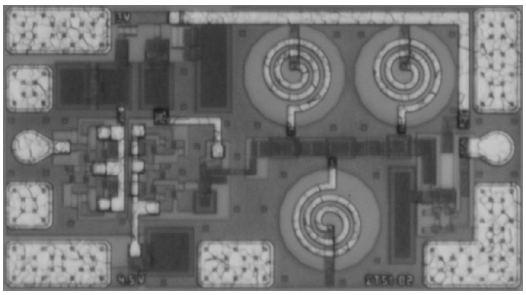

Figure 5.15: Micrograph of the impulse generator integrated circuit.

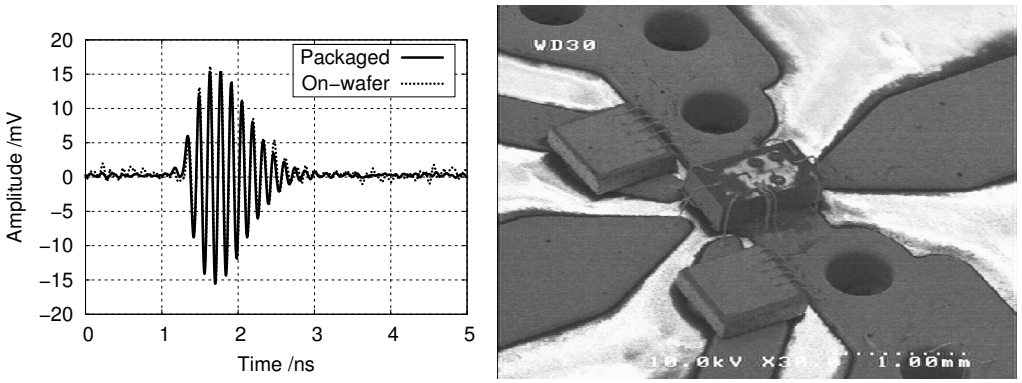

(a) (b)

Figure 5.16: (a) Comparison of on-chip and packaged time-domain impulse shape. (b) Picture of the mounted IC.

of 4.4 dB. The complete circuit has a power consumption of 58.6 mW and a chip size of 480 x 880 μm^2. A micrograph of the fabricated IC can be seen in Fig. 5.15. A package for the ECC impulse generator similar to the package of the FCC impulse generator is built with the IC glued chip-on-board onto the substrate and voltage regulators providing the DC supply. The performance comparison in Fig. 5.16 (a) shows no significant changes. A photograph of the package can be seen in Fig. 5.16 (b).

5.2.3 Modeling the Impulse Shape

For system simulations using the presented impulse shape, an equation-based modeling of the transient waveform is necessary. Similar to the discussion in Sec. 2.2.2, an envelope-gated sinusoidal modelling can be used. Here, an envelope consisting

of the summation of two Gaussian-shaped functions is suggested, which accounts for the unsymmetrical rise and fall time of the impulse. The function reads as

$$f(t) = \left(a_1 \cdot e^{-((t-b_1)/c_1)^2} + a_2 \cdot e^{-((t-b_2)/c_2)^2}\right) \cdot \sin(2\pi f \cdot (t + \tau/f)) \,, \qquad (5.7)$$

where the coefficients $a_{1/2}$, $b_{1/2}$ and $c_{1/2}$ are defining amplitude, position and width of each of the two Gaussian functions, f is the center frequency of the impulse and τ defines the phase alignment in the sinusoidal part. Tab. 5.1 provides the fitted coefficients for the normalized simulated and measured impulse. Fig. 5.17 (a) shows a comparison of the modeled with the measured curve, Fig. 5.17 (b) presents the modeled curve with the two Gaussian functions and the envelope function.

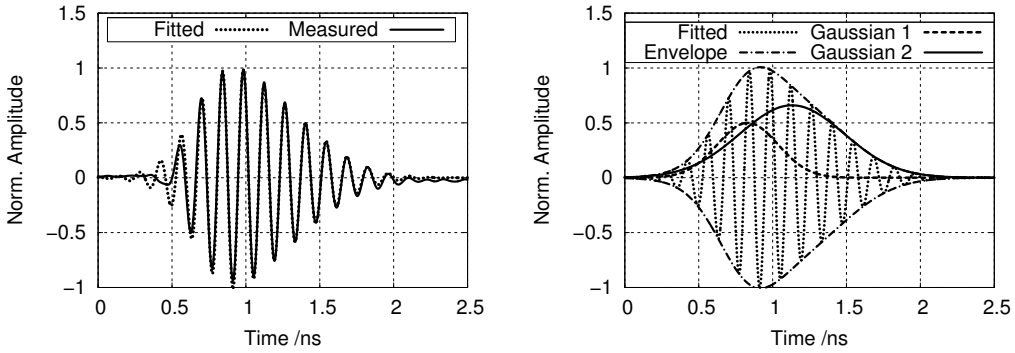

(a) (b)

Figure 5.17: (a) Comparison of normalized measured and fitted time-domain output waveform. (b) Fitted waveform together with the envelope functions and the two Gaussian functions used to build the envelope function.

Table 5.1: Fitted coefficients for the modeled functions

	a_1	b_1 /ns	c_1 /ns	a_2	b_2 /ns	c_2 /ns	f /GHz	τ
Simulation	0.57	0.85	0.37	0.66	1.28	0.55	7.35	1.86
Measurement	0.5	0.85	0.29	0.66	1.15	0.5	7.12	0.12

5.3 Biphase Impulse Modulator Circuit

In order to allow multiple UWB radar sensors to operate in the vicinity of each other, one possibility for a proper separation is to use different repetition frequencies f_c in the two sensors. Another possibility is to modulate the transmitted impulse train with a spreading sequence. For example, the impulses could be spread and despread by a biphase modulation scheme using the impulse itself on the one hand and its inverted replica on the other. A user separation between two sensors could be achieved by using two different spreading sequences, which must be orthogonal to each other for unique recovery [27]. By applying the correct spreading sequence, the signal can be recovered in the desired receiver, while the signal is canceled in the other receivers in which a different spreading sequence is applied. The use of such a scheme is, for example, proposed in [26] for a communication system, but the scheme would work for the UWB radar sensor in a similar way. Usually a biphase modulation feature is not implemented in current impulse generators. One of the few implementations can be seen in [91], where differential impulse generation and a cross-coupled switch matrix is used. In this study, a single-ended UWB biphase modulator in a separate circuit is developed, which is compatible with the FCC and ECC impulse generators presented before. The circuit is designed and fabricated in the 0.8 µm SiGe HBT semiconductor technology of Telefunken Semiconductors [48, 49].

5.3.1 Circuit Concept

The fundamental operation of the modulator circuit is similar to a multiplication of the high-frequency impulse with a positive or negative switching signal. A multiplication of the impulse with a positive switching signal results in a non-inverted output impulse, and the multiplication with a negative switching signal inverts the impulse. Fig. 5.18 shows a simplified circuit schematic of the biphase modulator providing this operation.

At its core, a four-quadrant multiplier based on a double-balanced Gilbert cell topology is chosen. The upper four transistors (transistor quad) of the Gilbert cell (T_1, T_2, T_3 and T_4) are optimized as signal switches. The switching signal activates either transistors T_1, T_4 or T_2, T_3. If in one switching state e.g. T_1 is off, the current flowing through R_1 passes through T_3. This ensures that the current flow is not interrupted and the voltage level does not rise up to the supply voltage level, distorting the correct operation. For this reason, a double-balanced topology is necessary and

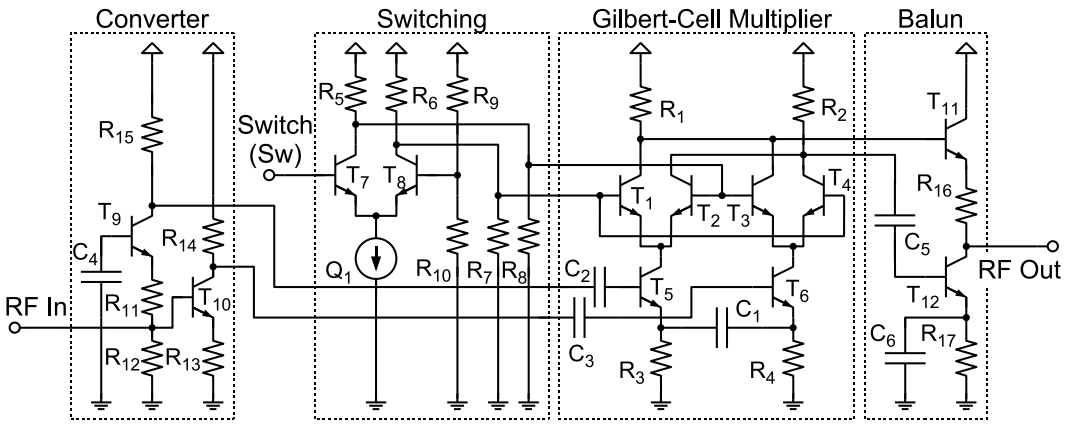

Figure 5.18: Simplified schematic of the UWB biphase modulator circuit.

cannot be reduced to only half of the circuit. When operated in one of the switching states, the Gilbert cell core circuit is regarded as a differential cascode stage. The lower two transistors (transistor pair) of the Gilbert cell (T_5 and T_6) are optimized for high linearity and wide bandwidth by applying feedback with the resistances R_3 and R_4 and the peaking capacitance C_1. A transfer gain of one between input and output is targeted. Since the Gilbert-cell is a fully differential circuit, all input signals need to be converted from single-ended to differential and the output signal needs to be converted back. The single-ended impulse signals at the RF input of the modulator circuit are converted to differential signals by an unbalanced-to-balanced converter. The converter topology applied in this circuit uses the non-inverting behavior of transistor T_9 in common-base configuration and the inverting behavior of T_{10} in common-emitter configuration. A big advantage of this topology is that the input matching can be easily adjusted by R_{11} and R_{12}. The differential output signal is converted to single-ended using a balanced-to-unbalanced converter (balun) with transistors T_{11} and T_{12} in a push-pull configuration. R_{17} and C_6 improve linearity and gain balance between the two inputs.

In order to also allow the switching operation with a single-ended input signal, a conversion from single-ended to differential is performed by a threshold-switch circuit. Changing the voltage level of the input voltage divider, which is formed by resistances R_5, R_8 and transistor T_7 on one side and R_6, R_7 and T_8 on the other side, forces a change of the current flow through the transistors and generates the differential switching voltage for the Gilbert cell. The input switching signal (Sw) is adjusted to be 0 V for the low and 2 V for the high switching state.

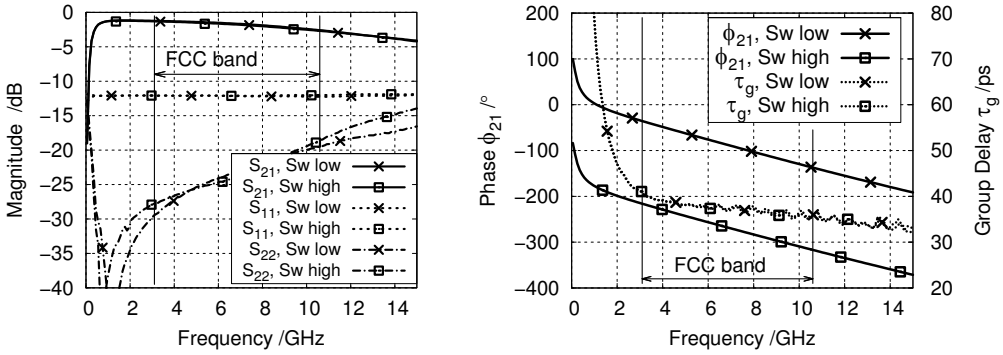

(a) (b)

Figure 5.19: Measured S-parameter performance of the biphase modulator in both switching states in (a) S-parameter magnitude and (b) phase and extracted group delay of the transmissions.

5.3.2 Measurement Results

The IC is characterized by several on-wafer measurements. The measured S-parameter performance is shown in Fig. 5.19 (a). The curves are very similar for low and high switching states. The measured gain (S_{21}) is around -2 dB within a variation of $\pm$1 dB. The measured input (S_{11}) and output (S_{22}) matching coefficients remain below -12 dB and -18 dB respectively within the complete FCC UWB frequency range. The measured reverse isolation (S_{12}) is below -40 dB between 3.1–10.6 GHz. Fig. 5.19 (b) shows the measured phase of the transmission coefficient (ϕ_{21}). The change in phase of 180° between the two switching states is maintained over the full UWB bandwidth. Fig. 5.19 (b) also gives the extracted group delay of the circuit. The small group delay variation of below 6 ps in the complete UWB frequency range, together with the small gain variation, promises only minor distortions to the incoming UWB impulse.

In order to prove this in time domain, a UWB impulse is applied to the input of the modulator and the output waveform is measured with an equivalent-time sampling oscilloscope. The impulse used is generated by the FCC-compliant impulse generator presented in Sec. 3.2.1. Fig. 5.20 (a) shows the time-domain output of the modulator in the two switching states, and by way of comparison, the impulse when connecting a through instead of the modulator is shown. This illustrates that the biphase switching clearly takes place and that both impulses are only a scaled version of the through-connected impulse, but that the impulse shapes remain un-

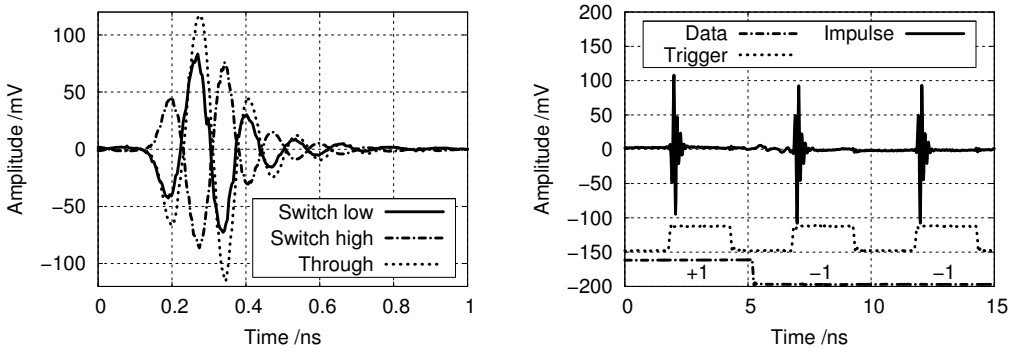

(a) (b)

Figure 5.20: Time-domain evaluation of the biphase modulator IC. (a) Comparison of impulse shapes between the input signal and the output signals in both switching states and (b) impulse train of an applied modulation.

changed. Fig. 5.20 (b) shows the measurement of a modulated impulse sequence at a repetition rate of 200 MHz, together with the return-to-zero coded trigger signal and the modulating data signal. The distortions due to switching remain below -25 dB and will decrease further when using a switching signal with a lower slew rate.

The linearity performance of the biphase modulator is determined by applying a sinusoidal stimulus to the circuit at different frequencies and varying input power. Losses of the cables and probes were carefully determined and are compensated

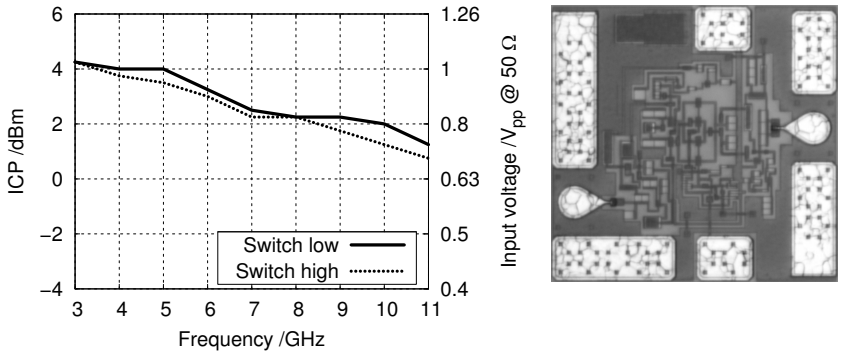

(a) (b)

Figure 5.21: (a) Linearity measurement of both switching states. (b) Micrograph of the fabricated IC.

during the measurement. Fig. 5.21 (a) plots the -1 dB input compression point versus frequency. The input compression point (ICP) stays above 1 dBm over the complete UWB frequency range and for both switching states. As done for the LNA in Sec. 4.2.1, Fig. 5.21 (a) presents the peak-to-peak input voltage amplitude corresponding to the sinusoidal input signal at 50 Ohm on the right ordinate. The circuit can handle input voltages larger than 650 mV_{pp}.

The circuit has a DC consumption of 31.4 mA at a 3.2 V bias in both switching states. The IC has an overall size of 510 x 490 μm^2. A micrograph of the circuit can be seen in Fig. 5.21 (b). As this performance shows, the circuit is very well suited to be used for a spreading and despreading operation in the UWB radar system.

6 Conclusion

In this thesis, the potential of an impulse-radio ultra-wideband radar sensor, realized with a chipset in a low-cost SiGe HBT semiconductor production technology together with commercial circuitry, has been demonstrated. With the hardware demonstrator presented, three different movement determination methods, i.e. undersampling reception, correlation-slope detection and sweeping-impulse correlation, have been compared and their advantages and disadvantages presented. By way of measurements, a movement determination in the millimeter down to the submillimeter range has been proven, and examples of breathing patterns of male adults and a seven-week-old infant have been shown successfully.

For a distribution of analog signals, i.e. speech, music or medical sensor information (such as body temperature or blood oxygen saturation), an innovative analog transmission scheme using UWB impulses has been presented. The transmission of analog information can be achieved by a continuous frequency modulation of the impulse train. Detailed measurements on a simple FM IR-UWB demonstrator have been shown, proving the modulation concept and showing the robustness of the modulation scheme to inband interferers, multi-user disturbance and multipath effects. The simple system concept is able to make use of commercially available and therefore cheap circuit components and requires only a small number of special UWB circuits. Accordingly, the system presented offers the opportunity for a fast commercial occupation of the UWB frequency band that is so far nearly unused.

Advancements to both concepts presented have been shown in three examples. First, the use of a UWB antenna array has been presented which applies a novel concept for a purely electronical beam steering. In order to make use of the spectral UWB masks in Europe, an impulse generator has been proposed which targets the ECC UWB regulation. For the IR-UWB radar sensor, a biphase modulator circuit has been presented which could be used for a multi-user separation by applying a biphase spreading sequence to the transmitted impulse train and a corresponding despreading in the receiver. The circuits have been qualified for UWB operation by detailed characterizations.

Further improvements can be envisioned in all building blocks of the presented system. For example, impulse generators producing an increased impulse amplitude could allow to span a larger distance for both the IR-UWB radar sensor and the FM IR-UWB communication system. The mask-conformity could be maintained for the increased impulse amplitude by a lower impulse repetition rate. For battery-supplied devices, the power-saving potential of the IR-UWB system principle could be exploited, bringing the circuits to idle-state when no impulse signal is present. For the IR-UWB radar, refined object determination methods could be developed, which could increase the object recognition in a strong multipath environment or with a small radar cross-section of the object, or could perform a multi-object discrimination. With a second receive antenna, a two-dimensional tracking could become possible. A very obvious bottleneck of the simple FM IR-UWB demonstrator presented is the rectifying Schottky diode, where a significant amount of the signal is not rectified and therefore lost to the system. A refined architecture could improve this system. The stereo and radio data system (RDS) capabilities of the classical FM radio could be used directly with the FM IR-UWB architecture, allowing to transmit a digital and two analog information signals with the same hardware arrangement.

All in all IR-UWB technology remains a very interesting candidate for new transmission and sensing architectures. It is to be hoped that in the future IR-UWB will attract the interest it deserves and take its due place in the medley of modern radio systems.

A UWB Spectral Allocations

A.1 United States FCC Regulation

Table A.1: Average EIRP emission limits of the U.S. FCC UWB masks [6, 10]

Frequency range (GHz)	Indoor applications (dBm/MHz)	Outdoor applications (dBm/MHz)
< 0.96	-41.3	-41.3
0.96 – 1.61	-75.3	-75.3
1.61 – 1.99	-53.3	-63.3
1.99 – 3.10	-51.3	-61.3
3.10 – 10.6	-41.3	-41.3
> 10.6	-51.3	-61.3

Maximum allowed peak emissions level is 0 dBm EIRP, contained in a 50 MHz bandwidth and centered on the frequency at which the highest radiated emission occurs.

A.2 European ECC Regulation

Table A.2: Maximum allowed EIRP densities of the European ECC UWB mask [12, 14]

Frequency range (GHz)	Maximum mean EIRP density (dBm/MHz)	Maximum peak EIRP density (dBm/50 MHz)
< 1.6	-90	-50
1.6 – 3.8	-85	-45
3.8 – 4.2	-75	-30
4.2 – 4.8	-70 (-41.3) ‡	-30 (0) ‡
4.8 – 6.0	-70	-30
6.0 – 8.5	-41.3	0
8.5 – 10.6	-65	-25
> 10.6	-85	-45

(‡ Allowed in case mitigation techniques are applied)

B Abbreviations and Symbols

Abbreviations

ADC	Analog-to-Digital Converter
AWGN	Additive White Gaussian Noise
BPSK	Binary Phase Shift Keying
Cascode	Cascaded Anodes
CEPT	European Conference of Postal and Telecommunications Administrations
CNR	Carrier-to-Noise Ratio
CW	Continuous Wave
DARPA	U.S. Defense Advanced Research Projects Agency
DDS	Direct Digital Synthesizer
DFG	German Research Foundation (Deutsche Forschungsgemeinschaft)
ECC	Electronic Communication Commission
EIRP	Effective Isotropic Radiated Power
ETSI	European Telecommunications Standards Institute
FCC	Federal Communications Commission
FM	Frequency Modulation
FWHM	Full-Width at Half-Maximum
GPIB	General Purpose Interface Bus
GPS	Global Positioning System
GSM	Global System for Mobile Communications
HBT	Heterojunction Bipolar Transistor
IC	Integrated Circuit
ICP	Input-referred 1 dB Compression Point
IR	Impulse-Radio
IR-UWB	Impulse-Radio Ultra-Wideband
LNA	Low-Noise Amplifier
LP	Low-Pass
MMIC	Microwave Monolithic Integrated Circuit
OFDM	Orthogonal Frequency Division Multiplex

OOK	On-Off-Keying (Modulation)
OSD	Office of the Secretary of Defense
PAM	Pulse-Amplitude Modulation
PPM	Pulse-Position Modulation
PSD	Power Spectral Density
RADAR	Radio Detection and Ranging
RDS	Radio Data System
RF	Radio Frequency
RMS	Root-Mean-Square
SFDR	Spurious-Free Dynamic Range
SiGe	Silicon Germanium (Semiconductor material)
SMD	Surface-Mount Device
SNR	Signal-to-Noise Ratio
UKoLoS	Ultrabreitband-Funktechniken für Kommunikation, Lokalisierung und Sensorik
UMTS	Universal Mobile Telecommunications System
UWB	Ultra-Wideband

Symbols

ACF_s	Autocorrelation function of function s
$B_{FM,N}$	Modified Carson bandwidth
B_{tot}	Total bandwidth of a UWB signal (= $(f_H - f_L)$)
B_f	Fractional bandwidth of a UWB signal
$CCF_{s,g}$	Cross-correlation function of functions s and g
c_0	Speed of light ($\approx 3 \cdot 10^8$ m/s)
Δf	Difference frequency of repetition rate signals
Δf_c	FM deviation
$\Delta \tau_g$	Group delay variation
d_{max}	Maximum distance of sensing
$d_{min,pp}$	Point-to-point spatial resolution
$\epsilon_{r,eff}$	Effective relative dielectric constant
ϵ_0	Dielectric constant (= $8.854 \cdot 10^{-12}$ F/m)
f	Frequency
f_{max}	Highest observation frequency
$f_{s,max}$	FM rate (highest appearing FM information frequency)

f_s	FM information signal
f_c	Repetition rate of an UWB impulse signal/ FM carrier signal
f_H	Upper -10 dB corner frequency of a UWB signal
f_L	Lower -10 dB corner frequency of a UWB signal
Γ	Reflection coefficient
μ_0	Vacuum permeability (= $4\pi \cdot 10^{-7}$ H/m)
σ	Standard deviation of a Gaussian bell shape
τ	Time shift
T_{rep}	Repetition interval of an impulse train
T_s	Sampling time
Θ	Antenna observation angle
Z_x	Characteristic impedance of material x

C Publications

- S. Chartier, **B. Schleicher**, T. Feger, T. Purtova, and H. Schumacher, "79 GHz Fully Integrated Fully Differential Si/SiGe HBT Amplifier for Automotive Radar Applications," in *13th IEEE International Conference on Electronics, Circuits and Systems (ICECS)*, Nice, France, December 2006, pp. 1011–1014.
- J. Dederer, **B. Schleicher**, F. de Andrade Tabarani Santos, A. Trasser, and H. Schumacher, "FCC compliant 3.1-10.6 GHz UWB Pulse Radar System using Correlation Detection," in *IEEE MTT-S International Microwave Symposium (IMS)*, Honolulu, HI, June 2007.
- S. Chartier, **B. Schleicher**, F. Korndörfer, S. Glisic, G. Fischer, and H. Schumacher, "A Fully Integrated Fully Differential Low-Noise Amplifier for Short Range Automotive Radar Using a SiGe:C BiCMOS Technology," in *Proceedings of the 2nd European Microwave Integrated Circuits Conference*, Munich, Germany, October 2007, pp. 407–410.
- S. Chartier, E. Sönmez, J. Dederer, **B. Schleicher**, and H. Schumacher, "Millimeter-Wave Si/SiGe HBT Frequency Divider Using Dynamic and Static Division Stages," in *Asia-Pacific Microwave Conference (APMC)*, Bangkok, Thailand, December 2007.
- H. Schumacher, J. Dederer, **B. Schleicher**, and A. Trasser, "Si/SiGe Integrated Circuits for Impulse-Radio UWB Sensing and Communications (Invited Paper)," in *Asia-Pacific Microwave Conference (APMC)*, Bangkok, Thailand, December 2007.
- **B. Schleicher**, S. Chartier, G. Fischer, F. Korndörfer, J. Borngräber, T. Feger, and H. Schumacher, "A Compact Low-Power SiGe:C BiCMOS Amplifier for 77-81 GHz Automotive Radar," in *IEEE Topical Meeting on Silicon Monolithic Integrated Circuits in RF Systems (SiRF)*, Orlando, FL, USA, January 2008, pp. 195–198.
- S. Chartier, **B. Schleicher**, T. Feger, T. Purtova, G. Fischer, and H. Schumacher, "79 GHz fully integrated fully differential Si/SiGe HBT amplifier for

automotive radar applications," *Analog Integrated Circuits and Signal Processing*, vol. 55, no. 1, pp. 77–83, Februar 2008.

- **B. Schleicher**, J. Dederer, M. Leib, I. Nasr, A. Trasser, W. Menzel, and H. Schumacher, "Highly Compact Impulse UWB Transmitter for High-Resolution Movement Detection," in *IEEE International Conference on Ultra-Wideband (ICUWB)*, vol. 1, Hannover, Germany, September 2008, pp. 89–92.

- J. Dederer, **B. Schleicher**, A. Trasser, T. Feger, and H. Schumacher, "A Fully Monolithic 3.1-10.6 GHz UWB Si/SiGe HBT Impulse-UWB Correlation Receiver," in *IEEE International Conference on Ultra-Wideband (ICUWB)*, vol. 1, Hannover, Germany, September 2008, pp. 33–36.

- M. Leib, E. Schmitt, A. Gronau, J. Dederer, **B. Schleicher**, H. Schumacher, and W. Menzel, "A Compact Ultra-wideband Radar for Medical Applications," *FREQUENZ*, vol. 1–2, no. 63, pp. 2–8, January/ February 2009.

- **B. Schleicher**, J. Dederer, and H. Schumacher, "Si/SiGe HBT UWB Impulse Generators with Sleep-Mode Targeting the FCC Masks," in *IEEE International Conference on Ultra-Wideband (ICUWB)*, Vancouver, Canada, September 2009, pp. 674–678.

- **B. Schleicher**, H. Ghaleb, A. Trasser, and H. Schumacher, "FM over Impulse Radio UWB," in *IEEE International Conference on Ultra-Wideband (ICUWB)*, Vancouver, Canada, September 2009, pp. 200–204.

- T. Thiasiriphet, M. Leib, D. Lin, **B. Schleicher**, J. Lindner, W. Menzel, and H. Schumacher, "Investigations on a Comb Filter Approach for IR-UWB Systems," *FREQUENZ*, vol. 63, no. 9-10, pp. 179–182, September/ October 2009.

- H. Schumacher, **B. Schleicher**, D. Lin, M. Leib, and W. Menzel, "Compact I-UWB Frontends for Medical Sensing and Imaging," in *European Microwave Conference (EuMC), Workshop on 'Advances in UWB Localization and Sensing'*, Rome, Italy, October 2009.

- G. Liu, **B. Schleicher**, T. Purtova, and H. Schumacher, "Fully Integrated Millimeter-Wave VCO Using Slow-Wave Thin-Film Microstrip Line for Chip Size Reduction," in *Proceedings of the 4th European Microwave Integrated Circuits Conference (EuMIC)*, Rome, Italy, October 2009, pp. 116–119.

- **B. Schleicher** and H. Schumacher, "Impulse Generator Targeting the European UWB Mask," in *10th Topical Meeting on Silicon Monolithic Integrated Circuits in RF Systems*, New Orleans, LA, January 2010, pp. 21–24.
- **B. Schleicher**, C. A. Ulusoy, and H. Schumacher, "A Biphase Modulator Circuit for Impulse Radio-UWB Applications," *IEEE Microwave and Wireless Components Letters*, vol. 20, no. 2, pp. 115–117, February 2010.
- M. Leib, T. Mach, **B. Schleicher**, C. A. Ulusoy, W. Menzel, and H. Schumacher, "Demonstration of UWB Communication for Implants Using an Energy Detector," in *German Microwave Conference (GeMIC)*, Berlin, Germany, March 2010.
- M. Leib, W. Menzel, **B. Schleicher**, and H. Schumacher, "Vital Signs Monitoring with a UWB Radar Based on a Correlation Receiver," in *European Conference on Antennas and Propagation*, Barcelona, Spain, April 2010.
- **B. Schleicher** and H. Schumacher, "Sendevorrichtung zur Erzeugung eines analog modulierten Impulszuges und zur Aussendung desselben sowie Empfangsvorrichtung zum Empfang eines entsprechendes Signals/ Transmission device for creating an analog modulated pulse train and for transmitting the same and reception device for receiving a corresponding signal," European Patent Application 2 175 569, April 14, 2010.
- T. Thiasiriphet, J. Lindner, **B. Schleicher**, H. Schumacher, M. Leib, and W. Menzel, "Device and method for impulse transmission and reception coping with multipath propagation, different types of interference and low SNR," European Patent Application 2 178 220, April 21, 2010.
- **B. Schleicher**, A. Trasser, M. Leib, W. Menzel, and H. Schumacher, "IR-UWB Radar Sensor for Ultra-Fine Movement Detection and Vital Sign Monitoring," in *IEEE International Conference on Wireless Information Technology and Systems (ICWITS), Workshop on 'Innovative Circuits, Systems and Applications for Local Position Estimation'*, Honolulu, HI, August 2010.
- **B. Schleicher**, S. Ahmed, A. Trasser, and H. Schumacher, "Multi-User Capability of an FM IR-UWB System," in *IEEE International Conference on Wireless Information Technology and Systems (ICWITS)*, Honolulu, HI, August 2010.
- **B. Schleicher**, M. Leib, W. Menzel, and H. Schumacher, "Beam steerable IR-UWB antenna array with FCC-compliant impulse generators," *Electronic Letters*, vol. 46, no. 18, pp. 1245–1246, September 2010.

- D. Lin, **B. Schleicher**, A. Trasser, and H. Schumacher, "A Highly Compact SiGe HBT Differential LNA for 3.1-10.6 GHz Ultra-Wideband Applications," in *IEEE International Conference on Ultra-Wideband (ICUWB)*, Nanjing, China, September 2010.
- D. Lin, **B. Schleicher**, A. Trasser, and H. Schumacher, "A SiGe HBT Low-Power Pulse Generator for Impulse Radio Ultra-wide Band Applications," in *IEEE International Conference on Ultra-Wideband (ICUWB)*, Nanjing, China, September 2010.
- D. Lin, **B. Schleicher**, A. Trasser, and H. Schumacher, "Si/SiGe HBT UWB Impulse Generator Tunable to FCC, ECC and Japanese Spectral Masks," in *IEEE Radio and Wireless Symposium (RWS)*, Phoenix, AZ, January 2011, pp. 66–69.
- C. A. Ulusoy, **B. Schleicher**, and H. Schumacher, "A Tunable Differential All-Pass Filter for UWB True Time Delay and Phase Shift Applications," *IEEE Microwave and Wireless Components Letters*, vol. 21, no. 9, pp. 462–464, September 2011.

Bibliography

[1] J. Dederer, *Si/SiGe HBT ICs for Impulse Ultra-Wideband (I-UWB) Communications and Sensing*. Cuvillier Verlag Göttingen, Jan. 2009.

[2] C. Fowler, J. Entzminger, and J. Corum, "Assessment of Ultra-Wideband (UWB) Technology," *IEEE Aerospace and Electronics Systems Magazine*, vol. 5, no. 11, pp. 45–49, Nov. 1990.

[3] C. McLaren, J. Null, and J. Quinn, "Heat Stress From Enclosed Vehicles: Moderate Ambient Temperatures Cause Significant Temperature Rise in Enclosed Vehicles," *Pediatrics*, vol. 116, no. 1, pp. e109–e112, Jul. 2005, http://www.pediatrics.org/cgi/content/full/116/1/e109 or cf. http://ggweather.com/heat/index.htm.

[4] Aerospace Medical Association, Medical Guidelines Task Force, "Medical Guidelines for Airline Travel, 2nd edition," *Aviation, Space, and Environmental Medicine*, vol. 74, no. 5, Section II, pp. A1–A19, May 2003.

[5] WHO, *International Travel And Health*. World Health Organization, Mar. 2005, http://www.who.int/ith/chapters/en/index.html.

[6] Federal Communications Commission, "Revision of Part 15 of the Commission's Rules Regarding Ultra-Wideband Transmission Systems," FCC, Washington, D.C., USA, First report and order 02-48, Apr. 2002.

[7] M. Z. Win, D. Dardari, A. F. Molisch, W. Wiesbeck, and J. Zhang, "History and Applications of UWB," *Proceedings of the IEEE*, vol. 97, no. 2, pp. 198–204, Feb. 2009.

[8] T. W. Barrett, "History of Ultra Wideband Communications and Radar: Part I, UWB Communications," *Microwave Journal*, vol. 44, no. 1, pp. 22–54, Jan. 2001.

[9] T. W. Barrett, "History of Ultra Wideband Communications and Radar: Part II, UWB Radars and Sensors," *Microwave Journal*, vol. 44, no. 2, pp. 22–46, Feb. 2001.

[10] United States of America, "Code of Federal Regulations, Title 47 Telecommunication, Volume 1, Chapter 1, Part 15 Radio Frequency Devices," Rev. Oct. 2009, http://www.gpoaccess.gov/cfr/.

[11] I. Oppermann, M. Hämäläinen, and J. Iinatti, Eds., *UWB Theory and Applications*. John Wiley & Sons, Ltd, 2004.

[12] Electronic Communications Committee (ECC) within the European Conference of Postal and Telecommunications Administrations (CEPT), "Commission decision of 21 February 2007 on allowing the use of the radio spectrum for equipment using ultra-wideband technology in a harmonised manner in the Community," Official Journal of the European Union, document number C(2007) 522, Feb. 2007.

[13] H. Luediger and R. Kallenbronn, "Generic UWB Regulation in Europe," *FREQUENZ*, vol. 63, no. 9-10, pp. 172–174, Sep. / Oct. 2009.

[14] European Telecommunications Standards Institute, "Electromagnetic compatibility and Radio spectrum Matters (ERM); Short Range Devices (SRD) using Ultra Wide Band technology (UWB) for communications purposes; Harmonized EN covering the essential requirements of article 3.2 of the R&TTE Directive (Final Draft)," ETSI, Final draft ETSI EN 302 065 V1.2.1, Jul. 2010.

[15] W. T. Ang, J. Chen, and T. Lv, "High-Order Monocycle Design and Its Waveform-Generating Circuit for UWB Communications," *IEEE Transactions on Circuits and Systems—Part I: Fundamental Theory and Applications*, vol. 54, no. 8, pp. 1657–1665, Aug. 2007.

[16] G. T. F. de Abreu, C. J. Mitchell, and R. Kohno, "Jitter-Robust Orthogonal Hermite Pulses for Ultra-Wideband Impulse Radio Communications," *EURASIP Journal on Applied Signal Processing - Special Issue on Ultra-Wideband State of the Art*, vol. 3, pp. 369–381, Mar. 2005.

[17] H. W. Pflug, "UWB Pulse Shaping for IEEE 802.15.4a," in *Proceedings of the 38th European Microwave Conference*, Amsterdam, NL, Oct. 2008, pp. 713–716.

[18] Y. Zhu, J. D. Zuegel, J. R. Marciante, and H. Wu, "Distributed Waveform Generator: A New Circuit Technique for Ultra-Wideband Pulse Generation, Shaping and Modulation," *IEEE Journal of Solid-State Circuits*, vol. 44, no. 3, pp. 808–823, Mar. 2009.

[19] M. Kraemer, A. Lecointre, D. Dragomirescu, and R. Plana, "Architecture considerations for 60 GHz Pulse Transceiver Front-Ends," in *International Semiconductor Conference (CAS)*, vol. 2, Sinaia, Romania, Oct. 2007, pp. 425–428.

[20] H. Sheng, P. Orlik, A. M. Haimovich, L. J. Cimini, and J. Zhang, "On the Spectral and Power Requirements for Ultra-Wideband Transmission," in *IEEE International Conference on Communications (ICC)*, vol. 1, Anchorage, AK, May 2003, pp. 738–742.

[21] J. H. Reed, Ed., *An Introduction to Ultra Wideband Communication Systems*. Prentice Hall International, 2005.

[22] S. Sczyslo and T. Kaiser, "Evaluation of Localization Measurements in LoS and NLoS Scenarios Using Antenna Arrays," in *European Microwave Conference (EuMC), Workshop on 'Advances in UWB Localization and Sensing'*, Rome, Italy, Oct. 2009.

[23] F. Nekoogar, *Ultra-Wideband Communications: Fundamentals and Applications*. Prentice Hall, Aug. 2005.

[24] M. L. Welborn, "System Considerations for Ultra-Wideband Wireless Networks," in *IEEE Radio and Wireless Conference (RAWCON)*, Waltham, MA, USA, Aug. 2001, pp. 5–8.

[25] M. Wolf, N. Song, and M. Haardt, "Non-Coherent UWB Communications," *FREQUENZ*, vol. 63, no. 9-10, pp. 187–191, Oct. 2009.

[26] T. Thiasiriphet and J. Lindner, "A novel comb filter based receiver with energy detection for UWB wireless body area networks," in *IEEE International Symposium on Wireless Communication Systems (ISWCS)*, Reykjavik, Iceland, Oct. 2008, pp. 498–502.

[27] J. Lindner, *Informationsübertragung: Grundlagen der Kommunikationstechnik*. Springer, 2005.

[28] I. Güvenç and H. Arslan, "On the modulation options for UWB systems," in *IEEE Military Communications Conference (MILCOM)*, vol. 2, Oct. 2003, pp. 892–897.

[29] T. E. McEwan, "Body monitoring and imaging apparatus and method," Nov. 12, 1996, U.S. Patent 5,573,012.

[30] T. E. McEwan, "Body monitoring and imaging apparatus and method," Jun. 16, 1998, U.S. Patent 5,766,208.

[31] S. Azevedo and T. E. McEwan, "Micropower Impulse Radar," *Science and Technology Review*, pp. 16–29, Jan. / Feb. 1996.

[32] S. Azevedo and T. E. McEwan, "Micropower Impulse Radar," *IEEE Potentials*, vol. 16, no. 2, pp. 15–20, Apr. / May 1997.

[33] E. M. Staderini, "UWB Radars in Medicine," *IEEE Aerospace and Electronics Systems Magazine*, vol. 17, no. 1, pp. 13–18, Jan. 2002.

[34] E. M. Staderini and G. Varotto, "Optimization criteria in the design of medical UWB radars in compliance with the regulatory masks," in *IEEE Biomedical Circuits and Systems Conference (BIOCAS)*, Montreal, Quebec, Nov. 2007, pp. 53–58.

[35] F. Michahelles, R. Wicki, and B. Schiele, "Less Contact: Heart-rate detection without even touching the user," in *International Symposium on Wearable Computers (ISWC)*, Arlington, VA, Oct. 2004, pp. 4–7.

[36] G. Ossberger, T. Buchegger, E. Schirmbäck, A. Stelzer, and R. Weigel, "Non-invasive respiratory movement detection and monitoring of hidden humans using ultra wideband pulse radar," in *International Workshop on Ultra Wideband Systems. Joint with Conference on Ultrawideband Systems and Technologies*, Kyoto, Japan, May 2004, pp. 395–399.

[37] I. Y. Immoreev, S. Samkov, and T.-H. Tao, "Short-Distance Ultrawideband Radars," *IEEE Aerospace and Electronics Systems Magazine*, vol. 20, no. 6, pp. 9–14, Jun. 2005.

[38] I. Y. Immoreev and S. Ivashov, "Remote Monitoring of Human Cardiorespiratory System Parameters by Radar and its Applications," in *International Conference on Ultrawideband and Ultrashort Impulse Signals (UWBUSIS)*, Sevastopol, Crimea, Ukraine, Sep. 2008, pp. 34–38.

[39] J. Sachs, P. Peyerl, and M. Roßberg, "A new UWB-principle for sensor-array application," in *IEEE Instrumentation and Measurement Technology Conference (IMTC)*, vol. 3, Venice, Italy, May 1999, pp. 1390–1395.

[40] J. Sachs, P. Peyerl, R. Zetik, and S. Crabbe, "M-Sequence Ultra-Wideband-Radar: State of Development ," in *Proceedings of the International Radar Conference*, Adelaide, Australia, Sep. 2003, pp. 224–229.

[41] E. Zaikov, J. Sachs, M. Aftanas, and J. Rovnakova, "Detection of trapped people by UWB radar," in *German Microwave Conference (GeMIC)*, Hamburg, Germany, Mar. 2008, pp. 240–243.

[42] F. Thiel, M. Hein, J. Sachs, U. Schwarz, and F. Seifert, "Physiological signatures monitored by ultra-wideband-radar validated by magnetic resonance imaging," in *IEEE International Conference on Ultra-Wideband (ICUWB)*, vol. 1, Hannover, Germany, Sep. 2008, pp. 105–108.

[43] A. Nezirovic, S. Tesfay, S. E. Valavan, and A. Yarovoy, "Experimental Study on Human Breathing Cross Section using UWB Impulse Radar," in *Proceedings of the 5th European Radar Conference (EuRad)*, Amsterdam, The Netherlands, Oct. 2008, pp. 1–4.

[44] A. Nezirovic, A. G. Yarovoy, and L. P. Ligthart, "Experimental study on human being detection using UWB radar," in *International Radar Symposium (IRS)*, Krakow, Poland, May 2006, pp. 1–4.

[45] M. Y. W. Chia, S. Leong, C. Sim, and K. Chan, "Through-wall UWB radar operating within FCC's mask for sensing heart beat and breathing rate," in *35th European Microwave Conference*, vol. 3, Paris, France, Oct. 2005.

[46] M. H. W. Hoffmann, *Hochfrequenztechnik: Ein Systemtheoretischer Zugang*. Springer, 1997.

[47] S. Gabriel, R. W. Lau, and C. Gabriel, "The dielectric properties of biological tissues: III. Parametric models for the dielectric spectrum of tissues," *Physics in Medicine and Biology*, vol. 41, pp. 2271–2293, 1996.

[48] A. Schüppen, J. Berntgen, P. Maier, M. Tortschanoff, W. Kraus, and M. Averweg, "An 80 GHz SiGe production technology," *III-Vs Review*, vol. 14, no. 6, pp. 42–46, Aug. 2001.

[49] Telefunken Semiconductors, *SIGE2RF Design Manual*, 2010.

[50] J. Dederer, A. Trasser, and H. Schumacher, "SiGe impulse generator for single-band ultra-wideband applications," in *International SiGe Technology and Device Meeting (ISTDM)*, Princeton, NJ, USA, May 2006, pp. 274–275.

[51] J. Dederer, B. Schleicher, F. de Andrade Tabarani Santos, A. Trasser, and H. Schumacher, "FCC compliant 3.1-10.6 GHz UWB Pulse Radar System using Correlation Detection," in *IEEE MTT-S International Microwave Symposium (IMS)*, Honolulu, HI, Jun. 2007, pp. 1471–1474.

[52] N. Deparis, A. Boé, C. Loyez, N. Rolland, and P.-A. Rolland, "60 GHz UWB-IR Transceiver With Pulsed-Injected Locked Oscillator," in *Proceedings of the 37th European Microwave Conference (EuMW)*, Munich, Germany, Oct. 2007, pp. 1038–1041.

[53] N. Deparis, A. Siligarisy, P. Vincenty, and N. Rolland, "A 2 pJ/bit pulsed ILO UWB transmitter at 60 GHz in 65-nm CMOS-SOI," in *IEEE International Conference on Ultra-Wideband (ICUWB)*, Vancouver, Canada, Sep. 2009, pp. 113–117.

[54] V. F. Kroupa, "Noise Properties of PLL Systems," *IEEE Transactions on Communications*, vol. 30, no. 10, pp. 2244–2252, Oct. 1982.

[55] Hewlett Packard, "RF & Microwave Phase Noise Measurement Seminar," Jun. 1985, http://www.hparchive.com/.

[56] C. Rauscher, *Grundlagen der Spektrumanalyse*. Rohde & Schwarz GmbH & Co, KG, 2000.

[57] Agilent Technologies, *"8560 EC Series Spectrum Analyzers (Data Sheet)"*, Feb. 2008.

[58] Agilent Technologies, *Agilent Technologies 85671A Phase Noise Utility (User's Guide)*, Nov. 2000.

[59] J. Dederer, B. Schleicher, A. Trasser, T. Feger, and H. Schumacher, "A Fully Monolithic 3.1-10.6 GHz UWB Si/SiGe HBT Impulse-UWB Correlation Receiver," in *IEEE International Conference on Ultra-Wideband (ICUWB)*, vol. 1, Hannover, Germany, Sep. 2008, pp. 33–36.

[60] U. Tietze and C. Schenk, *Electronic Circuits – Handbook for Design and Applications*, 2nd ed. Springer, 2008.

[61] P. J. Gibson, "The Vivaldi aerial," in *9th European Microwave Conference*, Brighton, UK, Sep. 1979, pp. 101–105.

[62] W. Sörgel, C. Waldschmidt, and W. Wiesbeck, "Transient responses of a Vivaldi antenna and a logarithmic periodic dipole array for ultra wideband communication," in *IEEE Antennas and Propagation Society International Symposium (APS)*, vol. 3, Jun. 2003, pp. 592–595.

[63] Analog Devices Inc., *AD9959 – 4-Channel 500 MSPS DDS with 10-Bit DACs (Datasheet)*, Jul. 2005, rev. 0.

[64] Analog Devices Inc., *AD9959/PCB – Evaluation Board for 4-Channel 500 MSPS DDS with 10-Bit DACs (Datasheet)*, Oct. 2005, rev. 0.

[65] J. Garcia, S. G. LaJeunesse, and D. Bartow, *Measuring Spurious Free Dynamic Range in a D/A Converter*, Intersil Corporation Technical Brief 326, Jan. 1995, http://www.intersil.com/data/tb/tb326.pdf.

[66] W. W. Macalpine and R. O. Schildknecht, "Coaxial Resonators with Helical Inner Conductor," *Proceedings of the IRE*, vol. 47, no. 12, pp. 2099–2105, Dec. 1959.

[67] H. Koch, *Transistorsender: Entwurf, Berechnung und Bau von Sendern mit Transistoren*, 5th ed. Franzis, 1984.

[68] Meilhaus Electronic GmbH, *MEphisto Scope 1: Command-Interpreter*, Jan. 2010, Firmware-Version 3.10.

[69] National Instruments Corporation, *LabWindows/CVI 8*, 2005, Version 8.0.0.

[70] P. Devine, *Füllstandmessung mit Radar – Leitfaden für die Prozessindustrie*. VEGA Grieshaber KG, Baur Offset, 1990.

[71] J. Huettner, R. Gierlich, A. Ziroff, and R. Weigel, "A low cost Ultra-Wide-Band Pulse Radar in a guided wave gauging application," in *Proceedings of the 6th European Radar Conference (EuRAD)*, Rome, Italy, Sep. 2009, pp. 101–104.

[72] R. Mäusl, *Analoge Modulationsverfahren*, 2nd ed. Heidelberg: Hüthig Verlag, 1992.

[73] J. Dederer, A. Trasser, and H. Schumacher, "Compact SiGe HBT Low Noise Amplifiers for 3.1-10.6 GHz Ultra-Wideband Applications," in *Topical Meeting on Silicon Monolithic Integrated Circuits in RF Systems (SiRF)*, San Diego, CA, USA, Jan. 2006, pp. 391–394.

[74] S. Prasad, H. Schumacher, and A. Gopinath, *High-Speed Electronics and Optoelectronics*. Cambridge University Press, 2009.

[75] G. Gonzales, *Microwave Transistor Amplifiers: Analysis and Design*, 2nd ed. Prentice-Hall, 1996.

[76] H. Schumacher, *Lecture Notes on Monolithic Microwave Integrated Circuits (MMIC)* . Ulm University, 2005/ 2006.

[77] Avago Technologies, *HSCH-53xx Series: Beam Lead Schottky Diodes for Mixers and Detectors (1-26 GHz) (Datasheet)*, Sep. 2006.

[78] J. Jung, W. Choi, and J. Choi, "A Small Wideband Microstrip-Fed Monopole Antenna," *IEEE Microwave and Wireless Components Letters*, vol. 15, no. 10, pp. 703–705, Oct. 2005.

[79] J. Jung, K. Seol, W. Choi, and J. Choi, "Wideband Monopole Antenna for Various Mobile Communication Applications," *Electronics Letter*, vol. 41, no. 14, pp. 1313–1314, Nov. 2005.

[80] ELV Elektronik GmbH, *Mobiler Stereo-UKW-Prüfsender (Datasheet)*, 2009.

[81] ELV Elektronik GmbH, *Mini-Stereo-RDS-Radio-Modul (Datasheet)*, 2009.

[82] L. G. Maloratsky, "Setting Strategies for Planar Dividers/ Combiners," *Microwave Journal*, vol. 53, no. 3, pp. 62–84, Feb. 2010.

[83] M. Chiani and A. Giorgetti, "Coexistence between UWB and Narrowband Wireless Communication Systems," *Proceedings of the IEEE*, vol. 97, no. 2, pp. 231–254, Feb. 2009.

[84] M. Leib, M. Frei, and W. Menzel, "A Novel Ultra-Wideband Circular Slot Antenna Excited with a Dipole Element," in *IEEE International Conference on Ultra-Wideband (ICUWB)*, Vancouver, BC, Sep. 2009, pp. 386–390.

[85] W. Wiesbeck, G. Adamiuk, and C. Sturm, "Basic Properties and Design Principles of UWB Antennas," *Proceedings of the IEEE*, vol. 97, no. 2, pp. 372–385, Feb. 2009.

[86] U. Schwarz, M. Helbig, J. Sachs, F. Seifert, R. Stephan, F. Thiel, and M. A. Hein, "Physically small and adjustable double-ridged horn antenna for biomedical UWB radar applications," in *Proceeding of the 2008 IEEE International Conference on Ultra-Wideband (ICUWB2008)*, vol. 1, Hannover, Germany, Sep. 2008, pp. 5–8.

[87] S.-G. Kim and K. Chang, "A Low Cross-Polarized Antipodal Vivaldi Antenna Array for Wideband Operation," in *IEEE International Antennas and Propagation Symposium (APS)*, vol. 3, Monterey, CA, Jun. 2004, pp. 2269–2272.

[88] W. Sörgel, C. Sturm, and W. Wiesbeck, "Impulse Responses of Linear UWB Antenna Arrays and the Application to Beam Steering," in *IEEE International Conference on Ultra-Wideband (ICUWB)*, Zürich, Switzerland, Sep. 2005, pp. 275–280.

[89] C. T. Rodenbeck, S.-G. Kim, W.-H. Tu, M. R. Coutant, S. Hong, M. Li, and K. Chang, "Ultra-Wideband Low-Cost Phased-Array Radars," *IEEE Transactions on Microwave Theory and Techniques*, vol. 53, no. 12, pp. 3697–3703, Dec. 2005.

[90] X. H. Wu, A. A. Kishk, and Z. N. Chen, "A linear antenna array for UWB applications," in *IEEE Antennas and Propagation Society International Symposium*, vol. 1A, Washington, DC, Jul. 2005, pp. 594–597.

[91] T. Terada, S. Yoshizumi, Y. Sanada, and T. Kuroda, "Transceiver Circuits for Pulse-Based Ultra-Wideband," in *Proceedings of the 2004 International Symposium on Circuits and Systems (ISCAS)*, vol. 4, Vancouver, Canada, May 2004, pp. 349–352.

The resume is in the online version due to data privacy reasons not disclosed.